

Pore–Scale Reactive Transport Modeling of Subsurface Water–Rock Interactions

by
Jiahui You

A dissertation submitted to the Department of Petroleum Engineering,
Cullen College of Engineering
in partial fulfillment of the requirements for the degree of

DOCTOR OF PHILOSOPHY

in Petroleum Engineering

Chair of Committee: Dr. Kyung Jae Lee

Committee Member: Dr. Mohamed Soliman

Committee Member: Dr. Birol Dindoruk

Committee Member: Dr. Guan Qin

Committee Member: Dr. Ahmad Sakhaee-Pour

University of Houston
May 2022

Copyright 2022, Jiahui You

ACKNOWLEDGMENTS

I would like to thank my advisor Dr. Kyung Jae Lee, for all her patience, enthusiasm, motivation, encouragement, and support over the past four years. Dr. Lee's insight and knowledge steered me through this research. I need to thank all my committee members, Dr. Mohamed Soliman, Dr. Birol Dindoruk, Dr. Guan Qin, Dr. Ahmad Sakhaee-Pour, and Dr. S.M. Farouq-Ali, who provided significantly constructive comments and suggestions.

I would like to thank my colleagues, Lotanna Ohazuruike, Xuan Yi, and Xinwei Xiong, who helped me a lot with the experiment set-up. I also would like to thank my friends, who have supported me through this journey. And my biggest gratitude goes to my family for all the support, and to my husband Zhuoran. Thanks for all your support.

ABSTRACT

Understanding of reactive transport is of fundamental importance to various applications in subsurface systems of energy and resources. Such subsurface formations as natural shales have complex compositions with carbonate, clay, and sulfide. In such systems, mineral–fluid interactions have critical impact on the fluid transport, as subsequently resulting in the porosity–permeability alteration, pore geometry alteration, and flow pathways evolution. In this regard, the present dissertation establishes the pore–scale reactive transport models to investigate the impact of mineral–fluid interactions on fluid transport. The present dissertation mainly focuses on three mineral–fluid interactions: carbonate dissolution, clay swelling, and iron precipitation from sulfide (pyrite). Here, we take quartz as a non–reactive mineral, and did not consider the impact of organic matters. These mineral–fluid interactions are investigated through the following specific application problems: calcite dissolution by hydrochloric acid injection (to investigate the carbonate dissolution), CO₂–enriched brine injection (to investigate the carbonate dissolution and clay swelling), and hydraulic fracturing fluid injection into shale (to investigate the iron precipitation).

In the first application problem, the developed pore–scale reactive transport model is applied to the calcite dissolution by hydrochloride acid injection on the ideal grain models, digital rock images adapted from Niobrara formation, and the synthetic models having natural fracturs with surface roughness. The numerical result has been compared with the benchmark experiment for the validation of numerical method. The effects of Damköhler number (Da_{II}), Péclet number (Pe), the heterogeneity of the pore structure, and the mineralogy are investigated. The different dissolution and transport patterns are categorized with respect to the Da_{II} and the

Pe. By applying these results, we can choose the injection setting under chemical reaction–dominant range while avoiding diffusion to achieve efficient acidizing.

In the second application problem, the reactive transport model is coupled with the momentum conservation equation for plastic solid to describe the clay swelling during the injection of CO₂–enriched brine into the systems with mixed–minerals of calcite, clay, and quartz. The porosity–permeability relationships under mixed–mineral systems are investigated. In addition, the impact of fracture length, density, and connectivity on the fluid transport, porosity–permeability relationship, and evolution of pathways are studied. When the system contains clay, the permeability increase has been slowed by clay swelling, with respect to the porosity increase induced by calcite dissolution. In this regard, clay can be used to increase the sealing capacity for CO₂ storage.

In the third application problem of hydraulic fracturing fluid injection into shale, we first conduct the experiments with the pyrite samples to calibrate the reaction rate constants for the pyrite oxidation (at pyrite surface) and Fe²⁺ oxidation (in solution). The obtained reaction rate constants are utilized to establish the numerical method to track the pyrite surface oxidation and Fe²⁺ oxidation in solution. In the numerical simulation case 1, where the reactions of pyrite oxidation and Fe²⁺ oxidation occur, the transport patterns in the system are investigated based on the digital rock image model. For the numerical simulation case 2, the Level–set method is coupled with the reactive transport model to simulate the iron precipitation on the pyrite surface. The precipitation pattern on the digital rock image is investigated under different Damköhler numbers. Under the larger Da_{II} , the precipitation has longer dendritic shape, and the precipitation pattern is highly random.

The quantified pore-scale parameters obtained from this study are expected to improve current Darcy-scale models to accurately predict the long-term behavior of the subsurface water-rock interactions.

TABLE OF CONTENTS

ACKNOWLEDGMENTS	iii
ABSTRACT	iv
TABLE OF CONTENTS	vii
LIST OF TABLES	x
LIST OF FIGURES	xi
1 INTRODUCTION	1
1.1 Problem statement.....	1
1.2 Current state-of-the-art	3
1.2.1 Calcite dissolution by acidizing	3
1.2.2 CO ₂ -enriched brine injection into mixed-mineral systems	7
1.2.3 Iron precipitation by hydraulic fracturing fluid injection into shale	8
1.3 Applications of Darcy-Brinkman-Stokes method in fluid-rock interactions.....	10
1.4 Outline and the main objectives.....	12
1.5 Assumption and limitation.....	15
1.6 Main contributions.....	16
2 MATHEMATICAL MODEL	17
2.1 Introduction of the pore-scale model	17
2.2 The derivation of the volume-averaged momentum equation	19
2.3 Discretization of the DBS equation using Finite Volume Method.....	23
2.4 PISO algorithm	26
2.5 Derivation of mass balance equation.....	28
2.6 Summary of the governing equations and solution sequence.....	30
3 PORE-SCALE MODEL FOR ACID DISSOLUTION	33
3.1 Application of Darcy-Brinkman-Stokes equation in pore-scale model.....	33
3.2 Rate law and solid-liquid interface	35
3.3 Numerical method validation.....	36
3.4 Grid size sensitivity analysis	40
3.5 Stability analysis.....	42
4 INVESTIGATION OF ACID DISSOLUTION ON THE DIGITAL ROCK IMAGES	45

4.1	Introduction.....	45
4.2	Simulation of micro–grain porous media model	47
4.3	Simulation of digital rock under different dimensionless numbers	53
5	INVESTIGATION OF SURFACE ROUGHNESS ON THE ACID DISSOLUTION OF NATURAL FRACTURES.....	61
5.1	Introduction.....	61
5.2	Fracture roughness generation and volume–averaged parameters	62
5.3	Dissolution and transport in smoothed fracture	63
5.4	Dissolution and transport in fracture with rough surface	69
5.5	Dissolution in mineralogical composition fracture.....	83
6	INVESTIGATIONS OF MIXED–MINERALS SYSTEMS IN CO₂–ENRICHED BRINE INJECTION	88
6.1	Introduction.....	88
6.2	Mathematical model of injection of CO ₂ –acidified brine in mixed–mineral	89
6.3	Validation of the numerical method	90
6.4	CO ₂ –enriched brine in fracture system.....	94
6.4.1	Problem background.....	94
6.4.2	Effects of fracture density	97
6.4.3	Effects of fracture length.....	101
6.4.4	Effects of fracture connectivity	103
6.5	CO ₂ –enriched brine in mineralogical compositions of the fracture–matrix	107
7	INVESTIGATION OF IRON PRECIPITATION BY HYDRAULIC FRACTURING FLUID INJECTION INTO SHALE.....	112
7.1	Level–set method coupled with reactive transport model	112
7.2	Chemical reaction paths for the iron precipitation.....	114
7.3	Experiments for the validation of numerical modeling	115
7.4	Simulation cases using digital rock image models	120
7.4.1	Problem background.....	120
7.4.2	Simulation of the pyrite surface oxidation and Fe(II) oxidation in solution	122
7.4.3	Simulation of the iron precipitation.....	124
8	SUMMARY	128
8.1	Conclusions.....	128

8.2 Recommendations for future work	130
REFERENCES.....	132
APPENDIX.....	147
A1. Notation of the volume-averaged technique.....	147
A2. Averaged continuity equation	148
A3. Averaged momentum equation	150
A4. Closure problem	153
A5. Discretization theory	154
A6. Validation of the solid deformation	156

LIST OF TABLES

Table 2-1 The governing equations of pore–scale model to describe the dissolution	31
Table 3-1 Input parameters in the simulation case for the validation (Soulaine & Tchelepi, 2016).	38
Table 4-1 Typical sizes of previous pore–scale modeling.	46
Table 4-2 Input parameters in the simulation case for the validation (Soulaine et al., 2017).	48
Table 4-3 Size and initial porosity of ideal grain model.	49
Table 4-4 Parameters for the simulations of the cases for Niobrara formation digital image.	55
Table 5-1 Parameters for the smoothed surface fracture simulation.	64
Table 5-2 Geometric parameters of single sine wave profiles and the corresponding surface roughness pattern.	71
Table 5-3 Geometric parameter of multiple sine wave profiles and the corresponding surface roughness pattern.	72
Table 5-4 Parameters in the simulation.	72
Table 6-1 Concentration of aqueous species in the experiment (Agrawal et al., 2020).	91
Table 6-2 Boundary condition and parameters for the simulation (Molins et al., 2017).	96
Table 7-1 Input parameter for the pyrite oxidation simulation (Q. Li, Jew, Brown Jr, Bargar, & Maher, 2020).	122
Table 7-2 Input parameters for the different cases.	125

LIST OF FIGURES

Fig. 1-1 The schematic of subsurface water–rock interaction considered in this study.	1
Fig. 1-2 The schematic of the iron precipitation mechanisms adapted from (Jew et al., 2017). (a) the $\text{Fe}(\text{OH})_3$, Fe_3O_4 , Fe_2O_3 , precipitation under neutral environment; (b) the Ferrihydrite precipitation under acidic environment.	10
Fig. 2-1 Schematic concepts of Darcy–scale and pore–scale. In Darcy–scale, porosity (ϕ) is to describe porous media. In pore–scale modelling, each control volume has its own phase of solid or fluid.	18
Fig. 2-2 The schematic for multi–scale description of the porous media.	19
Fig. 2-3 The schematic of the averaging volume.	20
Fig. 2-4 The solution sequence for the numerical method.	32
Fig. 3-1 Schematic graph showing the different scale simulations. Darcy–scale model uses porosity (ϕ) to describe the porous media with the range from 0 to 1.	34
Fig. 3-2 The example of pore–scale model on the digital rock.	35
Fig. 3-3 Schematic geometry model and boundary condition of the validation case.	39
Fig. 3-4 (a) Changing of calcite during the acidizing; the first row was obtained from experimental results (Soulaire et al. 2017), and the second row was obtained from the presented work. (b) Changing normalized solid mass with time. (c) Changing normalized surface area with time.	39
Fig. 3-5 The discretization the computation domain with different grid size.	40
Fig. 3-6 The contours of the pore volume fraction in different grid sizes.	41
Fig. 3-7 The values of the simulation result (volume fraction of calcite) with different grid sizes.	42
Fig. 3-8 Residuals for the simulation under different input parameters.	44
Fig. 4-1 The discretization the computation domain and the large view of the geometric model.	48
Fig. 4-2 Acid concentration and corresponding contour at $t = 5$ s. (a) Cases A1, B1 and D1; (b) Cases DD1 and SD1; (c) Cases A2, A3 and A4. X axis corresponds to the vertical position along the outlet boundary.	50
Fig. 4-3 Normalized effective surface area with time and volume fraction of pore space for A2, A3 and DD1 at 320 s, 620 s and 600 s.	51

Fig. 4-4 Chemical reaction rate of different grain models with time.....	52
Fig. 4-5 (a) Digital rock of Niobrara formation, CO, USA (Prodanovic 2016); (b) The discretization of the computational domain.	54
Fig. 4-6 Acid concentration contours for different Damköhler numbers and Péclet numbers at $t_1 = 50$ s and $t_2 = 1,500$ s. (a), (b), (c), (d), (e), and (f) correspond to the case 1, 2, 3, 4, 5, and 6, respectively. ...	57
Fig. 4-7 Streamline and velocity vector of fluid flow at $t = 1,500$ s. Arrow denotes the direction of flow; size and color denote the magnitude of the velocity. (a), (b), (c), (d), (e), and (f) correspond to the case 1, 2, 3, 4, 5, and 6, respectively.	58
Fig. 4-8 (a) Volume fraction of pore with time. (b) Normalized effective surface area with time.	59
Fig. 4-9 Volume fractions of pore at $t_1=5,000$ s and $t_2=8,000$ s.....	60
Fig. 5-1 The discretization of the computational domain (above) and the expanded view (below).	64
Fig. 5-2 The different dissolution patterns under different dimensionless numbers, where the results of C3, C4 and C6 were observed at t $= 1,000$ s, C10 at $t = 100,000$ s, and the others at $t = 3,000$ s.	66
Fig. 5-3 The acid concentration distribution under different dimensionless numbers, where C3, C4 and C6 were observed at $t = 1,000$ s, C10 at $t = 100,000$ s, and the others at $t = 3,000$ s.	67
Fig. 5-4 Calcite dissolution patterns.	67
Fig. 5-5 (a) Volume fraction of pore space with time; (b) Effective surface area with time; (c) Dissolution rate with time.	69
Fig. 5-6 The discretization of the computational domain (above) and the expanded view (below).	70
Fig. 5-7 Acid concentration for different surface roughness in the fracture. (a), (b), (c), (d), (e), (f), (g), (h), and (i) correspond to the case P1, P2, P3, P4, P5, P6, P7, P8, and P9, respectively. The bottom figures are the partial enlarged details for the highlighted area. ...	73
Fig. 5-8 Velocity streamline and velocity vector under different surface geometric model. (a), (b), (c), (d), (e), (f), (g), (h) and (i) correspond to the case P1, P2, P3, P4, P5, P6, P7, P8, P9, respectively. The streamline was colored by the velocity magnitude.	74
Fig. 5-9 The volume fraction of pore at different time of the half upper side of the computational domain. Red color represents the pore, and blue color represents the solid rock. (a), (b), (c), (d), (e), (f),	

(g), (h), and (i) correspond to P1, P2, P3, P4, P5, P6, P7, P8, and P9, respectively.	75
Fig. 5-10 Acid dissolution rate of upper side of the fracture. (a), (b), (c), (d), (e), (f), (g), (h), and (i) corresponds to the case P1, P2, P3, P4, P5, P6, P7, P8, and P9, respectively.	76
Fig. 5-11 (a) Normalized permeability with normalized porosity for cases P1-P9; (b) Dissolution rate with time for cases P1-P9; (c) Effective surface area with time for cases P1-P9; (d) Normalized porosity with time for cases P1-P9.....	78
Fig. 5-12 (a) Normalized permeability with normalized porosity for cases SW1-SW10; (b) Effective surface area with time for cases SW1-SW10; (c) Dissolution rate with time for cases SW1-SW10.....	80
Fig. 5-13 (a) Normalized permeability with normalized porosity for cases M1-M10; (b) Effective surface area with time for cases M1-M10; (c) Dissolution rate with time for cases M1-M10.	81
Fig. 5-14 Evolution of fracture during acidizing of different fraction widths. The first row was at the initial time. The second row and the third row were at 13.9 h and 27.8 h, respectively.	82
Fig. 5-15 (a) Normalized permeability with normalized porosity under different widths; (b) Dissolution rate with time under different widths.	82
Fig. 5-16 The discretization of the computational domain (above) and the expanded view (bottom).....	84
Fig. 5-17 μ CT image of Indiana limestone sample containing different contents of quartz: (a) 0 vol%; (b) 4.5 vol%; (c) 5.6 vol%; (d) 9.2 vol%; (e) 12 vol%.	85
Fig. 5-18 Velocity streamline during the acidizing process with different mineralogical contents.	85
Fig. 5-19 (a) Changing volume fraction of pore space with time; (b) Changing effective surface area with time; (c) Changing dissolution rate with time; (d) The normalized porosity–permeability relationship.....	87
Fig. 6-1 (a) Images of the transmitted detector and the fluorescein detector of acid flow at 36,000s (Agrawal et al., 2020); (b) Numerical result of pH value distribution in the 3D; (c) Numerical pH value distribution of the cross-section; (d) pH value of the 2D case at 36,000 s.	93

Fig. 6-2 Comparison of measured pH value and Ca ion concentration from experiment (Agrawal et al., 2020) and numerical simulation under different flow rates.	93
Fig. 6-3 (a) 2D Micro-CT image of tight reservoir (1.5×1.35 cm) (Ning et al., 2019). (b) Geometric model for the simulation. The size is 1.5 cm in length and 0.5 cm in height. (c) Discretization of the computational domain with resolution of 300×100.	95
Fig. 6-4 (a) Typical mm-scale natural fracture model; (b) The relation of fracture size and the rock anisotropy (Concil, 2017).	96
Fig. 6-5 Changing pH in the fracture systems with different fracture density at $t = 27.8$ h (first row) and $t = 83.3$ h (second row).	98
Fig. 6-6 (a) Ca ion concentration and fracture evolution during the CO ₂ injection. The first row is at the beginning time of injection ($t = 1.38$ h). The second row and third row are at $t = 27.8$ h and $t = 83.3$ h, respectively; (b) Changing Ca ion concentration over time.	98
Fig. 6-7 Dissolution rate of different reaction paths under different fracture densities. (a) shows the dissolution rate contributed by the reaction of Eq. 5; (b) shows the dissolution rate contributed by the reaction of Eq. 6; (c) shows the total reaction rate for the calcite.	99
Fig. 6-8 (a) Normalized porosity and permeability relationship; (b) the velocity magnitude and streamlines. The black arrow denotes the main flow direction in D3. The red arrow denotes the additional pathway in D4, and white denotes the additional pathway in D5.	100
Fig. 6-9 Ca ion concentration and fracture evolution during the CO ₂ injection. The first row is at the beginning of the injection ($t = 1.38$ s). The second row and third row are at $t = 27.8$ h and $t = 83.3$ h, respectively.	101
Fig. 6-10 Changing pH in fracture systems with different branch lengths at $t = 27.8$ h (first row) and $t = 83.3$ h (second row).	102
Fig. 6-11 Dissolution rate of different reaction paths. (a) indicates the dissolution rates contributed by the reaction of Eq. 5; (b) indicates the dissolution rates contributed by the reaction of Eq. 6; (c) indicates the total reaction rate for the calcite.	102
Fig. 6-12 (a) Relationship between normalized porosity and normalized permeability; (b) changing Ca ion concentration in the system.	103
Fig. 6-13 Geometry schematics of fracture systems with different connections.	104

Fig. 6-14 Changing pH in fracture systems with different connectivity at $t = 15.3$ h (first row), 27.8 h (the second row) and 83.3 h (the third row).	105
Fig. 6-15 (a) Ca ion concentration and fracture evolution during the CO_2 injection. The first row is at the beginning time of injection ($t = 1.38$ h). The second row is at $t = 83.3$ h; (b) changing Ca ion concentration over time.....	105
Fig. 6-16 Dissolution rate of different reaction paths. (a) shows the dissolution rate contributed by the reaction of Eq. 5; (b) shows the dissolution rate contributed by the reaction of Eq. 6;(c) shows the total reaction rate for the calcite.	106
Fig. 6-17 (a) Normalized porosity and permeability relationship; (b) the velocity magnitude and streamlines.	107
Fig. 6-18 Schematic of fracture–matrix systems (black indicates calcite; yellow indicates quartz; blue indicates clay); (d) The discretization of the computational domain with resolution of 150×150	109
Fig. 6-19 Ca ion concentration of different mineralogical contents.	110
Fig. 6-20 Velocity distribution of different fracture–matrix systems.	110
Fig. 6-21 Normalized porosity and permeability curves.....	111
Fig. 7-1 The flow chart of the algorithm coupled Level–set method.....	114
Fig. 7-2 (a) The calibration of sulfate concentration in IC. (b) The standards solution of FeCl_2 and absorbance in UV–vis.	117
Fig. 7-3 (a) 3–D geometric model to mimic the experiment with Sample 1; (b) The cross section of the mesh; (c) The cross section of the initialization of the solid phase as a cube without surface roughness; (d) The cross section of the initialization of the solid phase with surface roughness.....	119
Fig. 7-4 The comparison between experimental results and numerical results of (a) Sulfate ion concentration; (b) Fe(II) concentration.	120
Fig. 7-5 (a) SEM image from Barnett shale (Vega et al., 2015); (b) EDS image of composite elemental map(Vega et al., 2015);(c) Geometric model of the numerical simulation. (d) The initialization of the pyrite in the computational domain with the mesh.	121
Fig. 7-6 The concentration of ions during the pyrite oxidation at $t = 1,000$ s; (a)Sulfate concentration; (b) Fe(II) concentration; (c) Fe(III) concentration; (d) Dissolved oxygen.	123
Fig. 7-7 The plot of ions concentration during the pyrite oxidation; (a) Sulfate concentration; (b) Fe(II) concentration; (c) Fe(III) concentration; (d) Dissolved oxygen.	124

Fig. 7-8 The volume fraction of pore during the iron precipitation. 126

Fig. 7-9 The concentration of Fe(III) during the iron precipitation. 127

Fig. A-1 (a) Schematic of the geometric model; (b) Clay porosity when fluid–
driven deformation reaches the steady state under different
dimensionless pressures with initial porosity of 0.5; (c) the
comparison of volume change between numerical results and
analytical results..... 158

1 INTRODUCTION

1.1 Problem statement

Understanding of reactive transport is of fundamental importance to various applications in subsurface systems of energy and resources, such as geologic sequestration of CO₂, reservoir stimulation through acidization, injection of hydraulic fracturing fluid in shale reservoirs, and subsequent alteration of geologic media as a result of water–rock interactions (Golfier et al., 2002; T. Huang, Hill, & Schechter, 1997; Hung, Hill, & Sepehrnoori, 1989; Michael & Khan, 2016; Schechter & Gidley, 1969; Tian, Xing, Tan, Gu, & Golding, 2016; T. Xu, Apps, & Pruess, 2003). The subsurface formations, taking the natural shales as the example, have complex compositions with carbonate, clay, sulfide, and quartz. The present dissertation focuses on three mineral–fluid interactions: carbonate dissolution, clay swelling, and iron precipitation from sulfide (pyrite), as shown in Fig. 1-1. Here, we take quartz as a non–reactive mineral and do not consider the impact of kerogen.

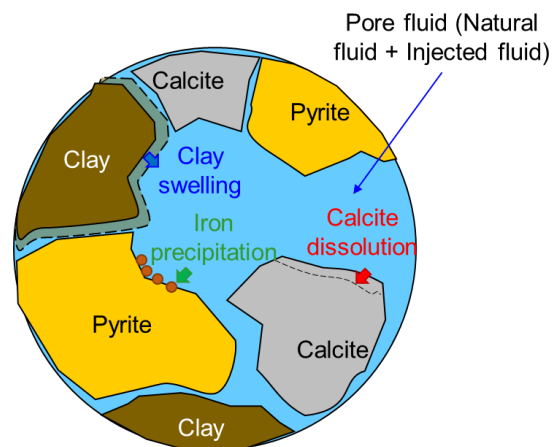


Fig. 1-1 The schematic of subsurface water–rock interaction considered in this study.

In the above-mentioned systems, we are exploring the three application problems to investigate the impact of those three mineral-fluid interactions on fluid transport by analyzing porosity-permeability evolution, pore geometry alteration, and flow pathways evolution: (1) Calcite dissolution by hydrochloric acid (to investigate the carbonate dissolution): Reactive transport caused by acid injection is a common process in petroleum reservoirs, while taking advantage of acid that can dissolve calcite and other substances, enlarge the radius of the flow channel, and profoundly enhance the hydrocarbon recovery; (2) CO₂-enriched brine injection (to investigate the carbonate dissolution and clay swelling): As well as calcite, non-reactive quartz and swelling clay can have significant impact on the reactants transport and subsequent reactions during the injection of CO₂-enriched brine. While injecting an enormous amount of CO₂ into carbonate-rich aquifers, CO₂ dissolves in the formation brine under the large pressure, and the subsequently formed CO₂-enriched brine reacts with the calcite. Reaction-induced changes in pore structure and fracture geometry alter the porosity and permeability, giving rise to the concerns of CO₂ storage capacity and environmental safety; (3) Hydraulic fracturing fluid injection into shale (to investigate the iron precipitation): In the applications of hydraulic fracturing in shale, fracturing fluid contains various organic additives. In such systems, ferrous iron is released from the pyrite in the shale reservoirs as interacting with hydraulic fracturing fluid. When the reservoir contains high content of calcite, the acid is neutralized, and ferrous iron is fast oxidized into ferric iron. Then, the iron is precipitated on the pyrite surface.

1.2 Current state-of-the-art

1.2.1 Calcite dissolution by acidizing

Reactive transport caused by acid injection is a common process in petroleum reservoirs, while taking advantage of acid that can dissolve calcite and other substances, enlarge the radius of the flow channel, and profoundly enhance the hydrocarbon recovery. To characterize the dynamic interplay between the evolution of solid–liquid interface and acid transport, we need a full–physics model describing calcite dissolution and acid transport from a pore–scale perspective. However, most of the presenting numerical models have not considered the stochastic nature of the initial structure of channels and the random reactive phenomena.

Since the 1980s, researchers have conducted acidizing experiments in various lithological cores. Lund first carried out the experiments of dolomite and calcite dissolution by hydrochloric acid, by employing a rotating disk system. The reaction rate was found to be proportional to the temperature–dependent fractional power of hydrochloric acid concentration (Lund, Fogler, & McCune, 1973). Then the variable density, viscosity, and fluid velocity were taken into account in the calcite dissolution (Lund, Fogler, McCune, & Ault, 1975). Later, Fogler conducted experiments in sandstone and developed a mathematical model to predict the acid transport and changing permeability as a function of acid concentration and flow rate (Fogler, Lund, & McCune, 1976). They categorized the dissolution patterns into the mass transfer–limited and reaction rate–limited groups. Later, the effects of various characteristics of solvents on the structure of porous media and the propagation rates of solvents were investigated (Hoefner & Fogler, 1988). The impact of different types of solvents (strong acids, weak acids, and chelating agents) and different acid formulations (straight acids, emulsions,

and gels) on the dissolution pattern and acid propagation rate were investigated in the subsequent core flooding experiments (Bazin, 2001; Fredd & Fogler, 1998). On the other hand, it was reported that the use of emulsion in acid caused relatively ineffective diffusion (Golfier et al., 2002). Modern imaging advancements have made it possible to detect the porous media structures from the nanometer to the micrometer scale and beyond (Molins et al., 2020). X-Rays are used to record and produce a three-dimensional description of the rock and fluids; Scanning Electron Microscopy (SEM) routinely produces two-dimensional images down to resolutions of 10 nm; FIB-SEM can produce 3-dimensional high-resolution images (Blunt et al., 2013). Dijk et al. used nuclear magnetic resonance imaging to measure aperture changes in fractured halite cores and demonstrated the impact of chemical reaction kinetics, transport processes, and initial fracture geometries on the dissolution phenomenon (Dijk, Berkowitz, & Yechieli, 2002). The textured glass with the smooth, transparent potassium-dihydrogen-phosphate (KDP) crystals was used to imitate surface roughness, and the high-resolution light-transmission techniques were employed to measure the evolving fracture aperture (Detwiler, Glass, & Bourcier, 2003).

Various pore-scale models were developed to investigate the calcite acidizing, applying Lattice Boltzmann Method (LBM), the Direct Numerical Simulation method (DNS), and Smoothed Particle Hydrodynamics (SPH) (Akanni, Nasr-El-Din, & Gusain, 2017; L. Chen et al., 2015; L. Chen, Kang, Viswanathan, & Tao, 2014; Deng, Molins, Trebotich, Steefel, & DePaolo, 2018; Kang, Zhang, & Chen, 2003; Kang, Zhang, Chen, & He, 2002; M. Liu & Mostaghimi, 2017a, 2017b; Molins, Trebotich, Steefel, & Shen, 2012; Pereira Nunes, Blunt, & Bijeljic, 2016; Soulaie, Roman, Kavscek, & Tchelepi, 2017, 2018; Soulaie & Tchelepi, 2016; Tartakovsky, Meakin, Scheibe, & West, 2007; Z. Xu, Meakin, & Tartakovsky, 2009). The last

decade has an explosion of LBM studies related to the calcite dissolution and fluid transport. LBM solves the governing equations on a lattice with streaming and collision, which can be directly simulated on pixels or voxels from 2-D or 3-D digital rock images. Kang et al. developed a pore-scale model to investigate the porosity-permeability relationship in calcite dissolution and precipitation affected by pore structure (Kang, Chen, Valocchi, & Viswanathan, 2014). They found that the dissolution pattern was influenced by not only the Damköhler number and Péclet number, but also the pore structure. Chen et al. studied the dissolution-induced changes in hydrologic properties of a fractured porous medium consisting of two minerals obtained with a quartet structure generation set (L. Chen et al., 2014). In their binary mineral medium, a multicomponent-multiphase flow was simulated, where the permeability increased slowly, in spite of the rapid increase of porosity. In the more recent LBM studies, the effects of coupled mechanisms like solvent transport, and chemical reaction induced precipitation and dissolution were investigated (L. Chen et al., 2015; L. Chen et al., 2014; Deng et al., 2018; Kang et al., 2003; Verhaeghe, Arnout, Blanpain, & Wollants, 2006). The LBM requires high computational resources for commercial-scale problems, because of the relatively large number of distribution variables corresponding to each node in the lattice. Besides, the LBM has restriction in simulating relatively high-Mach number incompressible flows and lacks consistent thermo-hydrodynamic schemes (Feng et al., 2010).

Besides the LBM, DNS models address the transport phenomena and fluid flow by solving the advection-diffusion equation and Navier-Stokes equation, respectively. The discretization methods for DNS models include Finite Volume Method (FVM), Finite Element Method (FEM), and Finite Difference Method (FDM). DNS models require an explicit approach to describe the solid-fluid interface. Several methods can be used to track the solid-

fluid interface: Arbitrary Lagrangian–Eulerian method tracks the zones by moving the mesh on the solid–liquid boundary along the reacting mineral; to employ the Embedded Boundary Method (EBM), the structured mesh is cut by the irregular shape of the solid–fluid boundary, and the cells over the irregular boundary are refined by the small grids; Level Set Method (LSM) defines the moving velocity to track the evolution of solid–fluid area; In the Immersed Boundary Condition (IBC) method, fluid zones are described by irregular configurations in the fixed Eulerian grids, while solid–fluid interface is represented by mobile Lagrangian grids (Mittal & Iaccarino, 2005). The small cut cells in EBM have significant impact on the robustness and stability, but the IBC method takes the advantages of the uniform, structured grids, which makes it possible to solve the Partial Difference Equations (PDE) in a robust and efficient way. Molins et al. incorporated EBM to capture the pore structure evolution during the acid dissolution and found the dissolution and transport characteristics in the model with spatially and mineralogically heterogeneous grains (Molins, Trebotich, Miller, & Steefel, 2017). Li integrated LSM with standard grid–based approach to simulate the acid dissolution and precipitation in complex geometries (X. Li, Huang, & Meakin, 2008). Soulaïne et al. proposed a micro–continuum model by incorporating the IBC method and compared that with the ALE method, finding that difference of solid mass obtaining from the two methods was less than 5%. The Arbitrary Lagrangian-Eulerian (ALE) is a finite element formulation, in which meshes are regenerated as a result of solid–liquid interface change in the problems such as calcite dissolution by acid. In the computational domain, the mesh can move arbitrarily to optimize the shapes of elements. The domain of interest can move along with materials to precisely track the boundaries and interfaces (Duarte, Gormaz, & Natesan, 2004). The IBC method has higher computation efficiency and numerical stability because the ALE method

solves a Laplace equation for the motion of all the points on the solid surface to have homogeneous mesh deformations.

1.2.2 CO₂-enriched brine injection into mixed-mineral systems

A number of studies investigated calcite dissolutions by CO₂-enriched brine, by applying direct visual observations of rocks through advanced imaging technics (Chaudhuri et al. 2008, Detwiler et al. 2003, Gouze and Luquot 2011, Hao et al. 2013, Menke et al. 2016). Smith conducted a core-flooding experiment on a sample from the evaporite formation, and the sample details were characterized using X-ray computed microtomography, before and after the exposure to the CO₂-enriched brine. The results showed that the CO₂-acidified brine preferentially consumed dolomite while anhydrite remained unreactive, where fracture orientation was the key factor to control CO₂ sequestration (Smith et al. 2013). Deng et al. found that the surface geometry of minerals exhibited complex evolutions: “comb-tooth” structures were generated from the preferential dissolution of calcite in transverse sedimentary bands; “degraded zones” structures were generated from homogeneously mixed calcite and dolomite or non-reactive minerals and quartz (Deng et al. 2013).

Many studies showed that initial pore structures were critical to the dynamic properties of rocks during the CO₂-enriched brine injection (Maheshwari et al. 2013, Al-Khulaifi et al. 2018, Menke et al. 2016). Thus, the investigation of pure carbonate rock is a systematic way to investigate the reactive transport phenomena between CO₂-acidified brine and minerals. In another study, to study the reaction kinetics of carbonate rock, the core-flooding experiment was conducted under reservoir condition (50 °C, 10 MPa) with the range of flow rates between 0.1 ml/min and 0.5 ml/min (Al-Khulaifi et al. 2018). The effective reaction rates were found 5–

38 times lower than the batch reaction rates under the same experimental condition, including partial pressure of CO₂ and reservoir temperature. Other investigation pointed out that the effective reaction rates were up to two orders of magnitude lower than those measured on a flat substrate without transport limitations (Menke et al. 2016).

A previous study conducted an experiment with a fractured limestone sample with clay coverage on the fracture surface (Noiriel et al. 2007). They found that as calcite reacted with CO₂-acidified brine, the clay coating was progressively developed, and the calcite dissolution rate and permeability decreased.

These studies proved that the heterogeneity of pores and mineral compositions had significant impact on the effective reaction rate, because the reaction was limited by the fast flow of fluid in channels. Given that the flow pathways evolution is critical in the injection of CO₂-acidified brine, we considered swelling and non-reactive quartz in this application, to investigate their effects on the mineral-fluid interaction, and subsequent evolutions of flow pathways and porosity-permeability relationship, by establishing the pore-scale modeling capability.

1.2.3 Iron precipitation by hydraulic fracturing fluid injection into shale

As reported by Energy Information Administration, about 60% of total U.S. oil production comes from shale reservoirs (Administration, 2021). Hydraulic fracturing fluid is widely used in shale reservoir productions to increase permeability. Hydraulic fracturing fluid contains diverse chemical additives, such as ethylene glycol, kerosene, guar gum, 2-ethyl hexanol, glycol ether, polyethylene glycol, and hydrochloric acid (Jew et al., 2017). When these

additives mix with reservoir water, chemical reactions occur, resulting in the dissolution or precipitation of minerals.

Previous experimental investigation indicated that the released Fe^{2+} oxidation and subsequent Fe^{3+} precipitation were the main paths to iron scale formation (Spencer, Garlapalli, & Trembly, 2020). Solution pH was the most important factor affecting the release of Fe into the solution. When the pH of the solution was 2.0 in the system, which happened in low carbonate shale formation and around the drill bores, the Fe^{2+} slowly oxidized into Fe^{3+} and ferrihydrite precipitated in the solution as the suspended precipitation, as shown in Fig. 1-2 (b). Under high carbonate contents, Fe^{2+} quickly oxidized into Fe^{3+} and iron precipitates on the pyrite surface (Fig. 1-2 (a)), where the environment around the shale formation far from the drill bores was neutral (Jew et al., 2017). The previous investigation found that during the injection of hydraulic fracturing fluid, the bitumen can be released from shales by interacting with it. The liberated bitumen formed a Fe^{3+} -bitumen complex and accelerated the iron oxidation and the precipitation for the both neutral and acidic condition (Q. Li, Jew, Cercone, et al., 2019). In the later study, Li et al. quantified the chemical reaction rate for the interaction between hydraulic fracturing fluid and shale matrices (Q. Li, Jew, Kohli, et al., 2019). They suggested that the chemical reaction of hydraulic fracturing fluid and shale had more impact on the greater depth zone than the observable reaction zone on the permeability. Thus, establishing the reactive transport model considering the stated phenomena relevant to iron would be effective in predicting the evolution of porosity and permeability in the deep area.

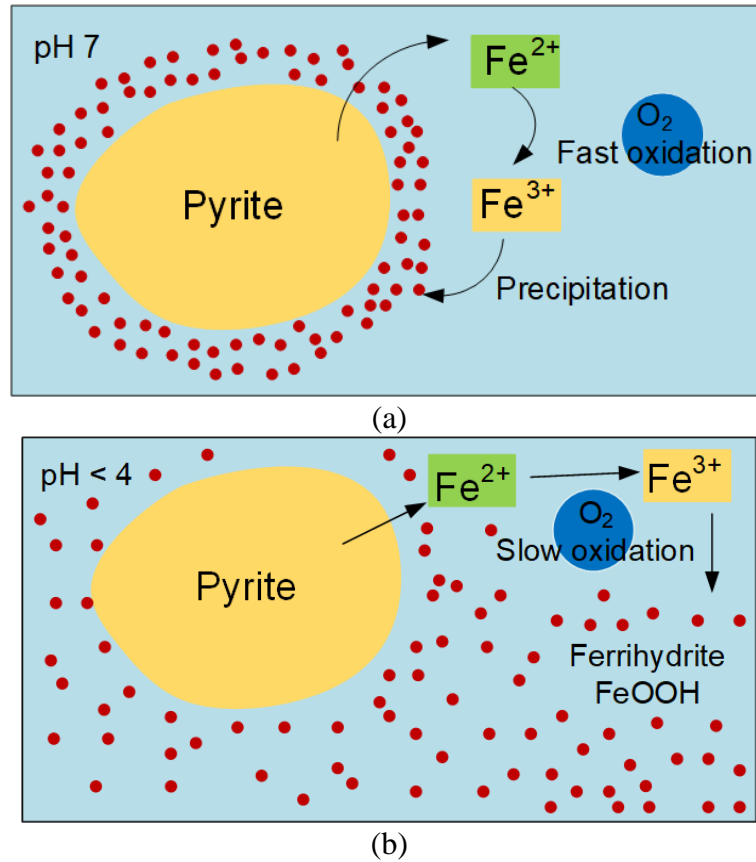


Fig. 1-2 The schematic of the iron precipitation mechanisms adapted from (Jew et al., 2017). (a) the $\text{Fe}(\text{OH})_3$, Fe_3O_4 , Fe_2O_3 , precipitation under neutral environment; (b) the Ferrihydrite precipitation under acidic environment.

1.3 Applications of Darcy–Brinkman–Stokes method in fluid–rock interactions

Darcy–Brinkman–Stokes method can use a single momentum equation to describe the fluid flow in both solid zone and fluid zone. We can take advantage of its numerical stability when applying into the dissolution and precipitation problem with dynamic changes of solid–fluid interface, so that we can avoid the regeneration of the grids and geometric structure during the simulation. We can also take advantage of its flexibility to implement to multi–mineral

systems. DBS method can describe the spatial distributions of different minerals, which can enable us to describe the different characteristics on each mineral. In this regard, we considered to use the DBS method in this dissertation research based on its advantages.

Brinkman firstly proposed the semi-empirical Stokes-Brinkman equation for an incompressible fluid flow in both porous media and the free zone (Brackbill, Kothe, & Zemach, 1992). The Stokes-Brinkman equation can be used to solve the fluid zone and porous media in a uniform equation and does not require the treatment on the interface. The permeability tensor is very large in the free zone, and the viscosity diffusion term dominates the flow. The Stokes-Brinkman equation changes into Stokes equations, which is the linearized format of the steady-state Navier-Stokes equations. In the porous media, Darcy's term dominates the flow and the Stokes-Brinkman equation can be simplified into the Darcy's Law.

Based on the volume averaging method, the macroscopic momentum transport equation in a non-homogeneous system was derived (Bousquet-Melou, Goyeau, Quintard, Fichot, & Gobin, 2002). The closed-form Navier-Stokes momentum equation contains the Forchheimer and Brinkman correction, and inertia terms. During the derivation, the porous media's evolution has been considered when analyzing and estimating all the terms raised from the volume averaging process by comparing with the characteristic's length associated with the structure. Later, the Darcy-Brinkman-Stokes (DBS) method was employed to give a microscopic view into complex phenomena with multiple functions and flexibility. DBS method uses a single momentum equation to describe fluid flow in both free zone and solid zone. Thereby, Darcy's Law and Navier-Stokes equation govern the fluid flow in the solid and free zones, respectively (Soulaire et al., 2017). DBS method can be implemented when both zones of pore (solid-free) and porous media (solid and pore) coexist in a region (Sadeghnejad, Enzmann, & Kersten,

2021). Soulaine extended the DBS method to describe the dissolution process over the whole control volume (Soulaine & Tchelepi, 2016). In the later work, Soulaine applied DBS method into calcite dissolution and upscaled the results obtained from pore-scale model to Darcy scale (Soulaine et al., 2017). DBS method can give the velocity distribution of the whole system, and the volumetric average fluid flow and pressure gradient can be obtained. In addition, the global permeability of the system can be calculated by Darcy's law. By capturing the moving solid-fluid interface of fracture, Molins studied the effects of the transport regime on the local reaction rates (Molins et al., 2017). Using structured and fixed Cartesian meshes to depict the fractured system with complex structure provided high efficiency and a stable way to simulate the changing interface processes. To the best of our knowledge, there are several pore-scale modeling studies taking distribution of micro-grains into account previously, but only few studies were specifically devoted to investigating the coupled calcite dissolution and transport mechanisms in pore-scale digital rock images.

1.4 Outline and the main objectives

Hypothesis of this dissertation research is that the mineral-fluid interactions will have significant impact on the reactive transport, through the alterations of pores and rock geometry. Pore structures in geologic systems are highly heterogeneous, and the heterogeneity significantly influences the mineral-fluid interactions, reactive transport pattern, flow pathways evolution, and porosity-permeability relationship. However, the previous studies have limited investigations on the impact of (1) various fractures and heterogeneous pore structures in the calcite dissolution by acid, (2) mixed-mineral systems with non-reactive quartz and swelling

clay (montmorillonite clay) in addition to calcite during the CO₂-enriched brine injection, and (3) iron precipitation by hydraulic fracturing fluid injection into shale, on the fluid transport.

In this work, we aim to develop pore-scale models to investigate the reactive transport and fluid flow of subsurface water-rock interactions to fill the above-mentioned gaps. The model based on the DBS method is built by revising the source codes and expanding the capability of OpenFOAM, an open-source platform for Computational Fluid Dynamics (CFD) (Weller et al. 1998). Based on OpenFOAM source codes, we (1) adapted the DBS momentum equation from the normal Navier-Stokes momentum equation; (2) adapted and coupled the multi-species advection-diffusion equations with DBS momentum equation of the surface reaction in the reactive transport model; (3) adapted and coupled the swelling pressure and reactive transport model with solid displacement solver to simulate the clay swelling during CO₂-enriched brine; (4) adapted the Level-Set method and coupled with reactive transport model of the iron precipitation. Here, the advection-diffusion equation is used to track the species concentration, and mass balance equation is used to describe the evolution of pore spaces due to mineral-fluid interaction. The established numerical simulator was employed in three applications to investigate the following characteristics:

First, we applied the HCl injection to investigate the carbonate dissolution. We choose the HCl as the only acid in the Chapters 4 and 5, because of the abundancy of relevant pore-scale studies regarding HCl-calcite reactions and its simplicity for the simulator validation and the interpretation of reactive transport phenomena obtained as a simulation result. Given that we developed our own in-house simulators of pore-scale reactive transport by revising and expanding the source codes of OpenFOAM, we needed previous studies with great amount of details for the validation of the developed simulator. As presented in Chapter 3, we could

validate our numerical method with the published workbench experiment of the surface reaction between calcite and HCl acid (Soulaire et al., 2017). In the first application:

(1) We elucidate the impact of highly heterogeneous pore structures and transport patterns on the calcite dissolution to improve our understanding of subsurface phenomena.

(2) We investigate the effects of surface heterogeneity, fracture morphology, and mineralogical composition of the rock matrix on fluid flow, reactive transport, and dynamic evolution of solid–fluid interface.

Second, we employed the CO₂–enriched brine injection to investigate the clay swelling and calcite dissolution. Specifically:

(1) We consider different natural fracture configurations and mineral components of clay, quartz, and calcite in fracture–matrix systems.

(2) The impact of fracture length, density, and connectivity on the fluid transport, porosity–permeability relationship, and evolution of pathways are studied.

Third, we considered the application problem of iron precipitation by hydraulic fracturing fluid injection into shale. Specifically:

(1) We first conduct experiment to provide the reaction rate constants of pyrite oxidation at surface and Fe²⁺ oxidation in solution.

(2) We combine Level–Set Method (LSM) with the pore–scale reactive transport model to address iron (Fe³⁺) precipitation in the neutral environment.

(3) We investigate the transport patterns for the numerical simulation case 1 by considering the pyrite oxidation and Fe²⁺ oxidation.

(4) The precipitation pattern on the conceptual model under neutral environment is investigated with the various Damköhler numbers in the numerical simulation case 2.

The structure of this dissertation is as follows: The introduction and background of the problem are described in Chapter 1. The mathematical method, including the derivation of the volume-averaged DBS momentum equation, discretization of the equation, and the scheme of the numerical method are presented in Chapter 2. We present the application problem of calcite dissolution by acid in Chapters 3-5. We take the dissolution problem as the example in Chapter 3 to further explain the DBS method, validation methods, discretization of the computational domain, and the effectiveness of DBS method coupled with the reactive transport model. Here, we investigate the hydrochloride acid to dissolve the calcite for the acidizing cases. Chapter 4 investigates the dissolution patterns on the digital rock models with respect to various dimensionless numbers. The acid dissolution patterns and porosity-permeability relationship in the natural fractures with various surface roughness and different contents of quartz are investigated in the Chapter 5. In Chapter 6, the effects of mixed-minerals of calcite, quartz, and clay are investigated in the injection of CO₂-enriched brine problem. We compare the natural fracture-matrix systems with different mineral components and investigate the various fracture density, length, and connectivity. The experimental characterization and numerical modeling of iron precipitation by hydraulic fracturing fluid injection into shale are presented in Chapter 7.

1.5 Assumption and limitation

(1) The fluid flow in this work is assumed to be continuum fluid.

(2) The numerical modeling in Chapter 3-5 considered the calcite dissolution only by hydrochloric acid.

(3) We considered the chemical reaction pathways approaching iron (Fe^{3+}) precipitation on the pyrite surface in the current numerical model.

1.6 Main contributions

(1) The dissertation provided the systematic and comprehensive approach to model the calcite dissolution patterns (by HCl) and quantified the pore structure evolution under various system conditions and model geometries.

(2) We established the pore-scale modeling approach in the mixed-mineral systems which contained the clay, calcite, and quartz during the process of CO_2 -enriched brine injection.

(3) The dissertation provided the reaction rate constants of pyrite oxidation and Fe^{2+} oxidation in the problem of hydraulic fracturing fluid injection into shale through experiments. By developing the pore-scale reactive transport model for this application problem, we provided the iron (Fe^{3+}) hydroxide precipitation patterns.

2 MATHEMATICAL MODEL

2.1 Introduction of the pore-scale model

The pore-scale model is defined as the scale at which each point of space is occupied by a specific phase, whether fluid or solid (Molins et al., 2020). The whole computational domain is discretized into structured grids on which the momentum, advection-diffusion, and mass balance equations are calculated. In this way, the spatial distribution of solid and fluid zones can be accurately distinguished; the evolution of solid-liquid interface is dynamically tracked as acid dissolves the rock, and the variation of acid distribution due to the chemical reaction and changing pore structures is described. As shown in Fig. 2-1, in Darcy-scale modelling, porosity (φ) is used to measure the void fraction of the entire domain, which is in the range from 0 to 1. In pore-scale modelling, local porosity (ε) represents the volume fraction of pore zone or solid zone within a control volume.

The volume-averaging technique defines the representative elementary volume has the average volume of V , and the volume of f -phase has V_f , and the volume of s -phase has V_s . The phase volume fraction has

$$\varepsilon_s = \frac{V_s}{V}, \varepsilon_f = \frac{V_f}{V}, \varepsilon_s + \varepsilon_f = 1. \quad (2-1)$$

In the fluid area, $\varepsilon_f = 1$, and $\varepsilon_s = 0$. For solid zone, $\varepsilon_f = 0$, and $\varepsilon_s = 1$. ε_f and ε_s have the relationship of $\varepsilon_s + \varepsilon_f = 1$. In the DBS method, Darcy's law describes the solid-liquid interface, where $0 < \varepsilon_f < 1$. Consider ψ as a continuous physical property in each phase of f - s system. The volume-averaging technique has

$$\psi = \begin{cases} \psi_f & \text{in } f \text{ - phase,} \\ \psi_s & \text{in } s \text{ - phase.} \end{cases} \quad (2-2)$$

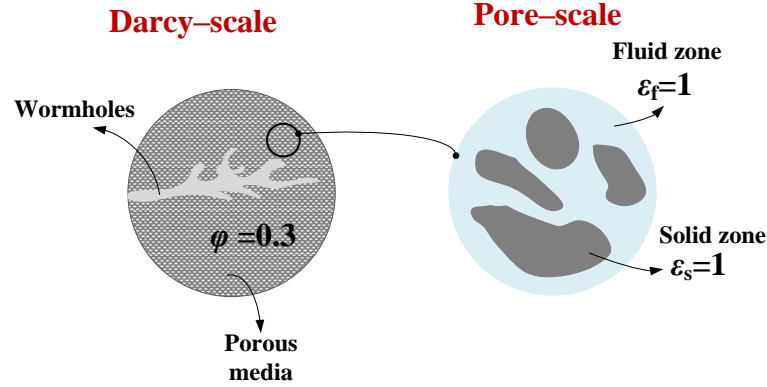


Fig. 2-1 Schematic concepts of Darcy-scale and pore-scale. In Darcy-scale, porosity (ϕ) is to describe porous media. In pore-scale modelling, each control volume has its own phase of solid or fluid.

We can define a superficial phase average of physical property ψ in the f -phase as

$$\langle \psi_f \rangle = \frac{1}{V} \int_{V_f + V_s} \psi_f dV. \quad (2-3)$$

$\langle \psi_f \rangle$ is the superficial averaged value and is not necessarily validated in the f -phase, because it took the integral by all the value including the s -phase and f -phase. Then, we need to take the phase average by integrating only over the f -phase and we have the intrinsic phase averaged value

$$\langle \psi_f \rangle^\alpha = \frac{1}{V_f} \int_{V_f} \psi_f dV. \quad (2-4)$$

The superficial averaged value and intrinsic phase averaged value have the relationship

$$\epsilon_f \langle \psi_f \rangle^f = \langle \psi_f \rangle. \quad (2-5)$$

Other denotations that are used in the volume-averaged technique can be found in the Appendix.

2.2 The derivation of the volume-averaged momentum equation

The volume-averaged DBS momentum equation was derived from the Navier-Stokes equation using the volume averaging technique. The volume-averaged technique was to rigorously derive the continuum equations for multi-phase system (Quintard & Whitaker, 1993). After applying the volume averaging technique, the equations that are only valid within a particular phase can be smoothly turned into the volume-averaged equation that are valid everywhere. For example, Navier-Stokes equation is only valid in the fluid zone, and after taking the volume averaging technique, the derived volume-averaged momentum equation is valid for the free zone and solid zone. Fig. 2-2 shows the multi-scale features of the typical porous media in pore-scale and large-scale. In the Darcy-scale, the characteristics length L can effectively represent the control volume. For the lower-scale, which is known as pore-scale, the fluid phase (denoted by the subscript of f) and solid phase (denoted by the subscript of s) are treated as the separated continua (Quintard & Whitaker, 1993). The characteristic length of fluid phase and solid phase are l_f and l_s , respectively. These characteristic lengths have the relationship of: $l_s, l_f \ll r_o \ll L$, where r_o is the radius of the averaging volume V . We also have the following relationships: $l_s, l_f \ll r_o \ll L_\epsilon$, L_ϵ is the characteristic length associated with the macroscopic variations of porosity.

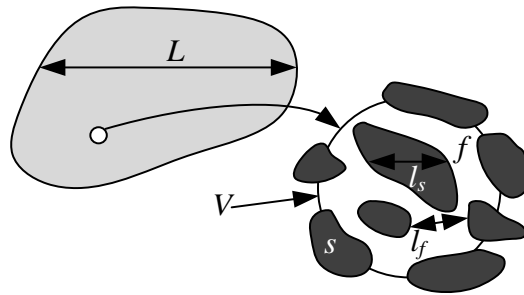


Fig. 2-2 The schematic for multi-scale description of the porous media.

The detail of the averaging volume is shown in Fig. 2-3. A_{fe} is the area of entrances and exits for the f -phase contained within the averaging volume; A_{fs} is the area of f - s interface; \mathbf{r} is the position vector of any location in t in the f -phase within the averaging volume. \mathbf{x} is the centroid of the averaging volume V , which can be in f -phase or s -phase (Bousquet-Melou et al., 2002). \mathbf{y} is the vector to locate points in f -phase relative to the centroid of V (Quintard & Whitaker, 1993).

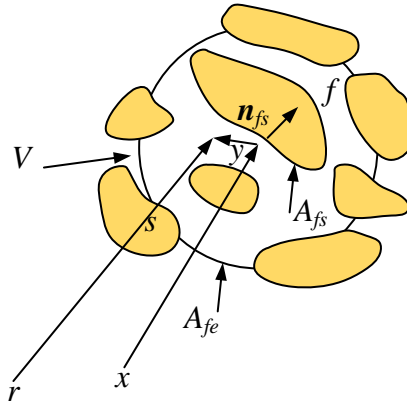


Fig. 2-3 The schematic of the averaging volume.

In this dissertation research, the DBS momentum equations are derived from the Navier–Stokes equations for using the volume averaging technique. We assume the fluid flow in porous media as incompressible flow and ignore the effects of gravity. In the present dissertation, we only considered single phase flow (water saturation is one). There is no interfacial transfer due to phase change, thus, there’s no momentum transfer in momentum equation. The Navier–Stokes momentum and mass conservation equations with the boundary conditions are shown as

$$\frac{\partial \rho_f}{\partial t} + \nabla \cdot (\rho_f \mathbf{v}_f) = 0, \quad (2-6)$$

$$\text{and } \frac{\partial}{\partial t} (\rho_f \mathbf{v}_f) + \nabla \cdot (\rho_f \mathbf{v}_f \mathbf{v}_f) = -\nabla P_f + \mu_f \nabla^2 \mathbf{v}_f. \quad (2-7)$$

In the f -phase, the boundary condition is

$$\rho_f \mathbf{n}_{fs} \cdot (\mathbf{v}_f - \mathbf{w}_{fs}) = \rho_s \mathbf{n}_{fs} \cdot (\mathbf{v}_s - \mathbf{w}_{fs}) \text{ at } A_{fs} \quad (2-8)$$

$$\text{and } v_f = f(\mathbf{r}, t) \text{ at } A_{fe}, \quad (2-9)$$

where, ρ_f is the density of fluid; v_f is the velocity in f -phase; v_s is the velocity in s -phase; P_f is the pressure in the f -phase; μ_f is the viscosity in the f -phase.

The volume-averaged technique has the following procedures (Bousquet-Melou et al., 2002; Quintard, 2015) :

a. Take the superficial average of the momentum equation using Eq. (2-3), and we get

$$\left\langle \frac{\partial}{\partial t} (\rho_f \mathbf{v}_f) \right\rangle + \langle \nabla \cdot (\rho_f \mathbf{v}_f \mathbf{v}_f) \rangle = -\langle \nabla P_f \rangle + \langle \mu_f \nabla^2 \mathbf{v}_f \rangle. \quad (2-10)$$

b. Use Gray decomposition ($\mathbf{v}_f = \langle \mathbf{v}_f \rangle^f + \tilde{\mathbf{v}}_f$) to define the velocity deviation.

Applying the Gray decomposition in the mass conservation equation of f -phase Eq. (2-6), we can obtain the equation

$$\frac{\partial \rho_f}{\partial t} + \nabla \cdot (\rho_f (\langle \mathbf{v}_f \rangle^f + \tilde{\mathbf{v}}_f)) = 0. \quad (2-11)$$

c. After arranging the equation and estimating the order of each term according to their characteristic length, we can obtain the following equation

$$\nabla \cdot \tilde{\mathbf{v}}_f = 0. \quad (2-12)$$

The detail of this procedure can be found in the appendix.

d. Take the surficial average of the momentum equation; we have the equation

$$\left\langle \frac{\partial}{\partial t} (\rho_f \mathbf{v}_f) \right\rangle + \langle \nabla \cdot (\rho_f \mathbf{v}_f \mathbf{v}_f) \rangle = -\langle \nabla P_f \rangle + \langle \mu_f \nabla^2 \mathbf{v}_f \rangle. \quad (2-13)$$

After the manipulations of the equation and the estimation the order of each term according to their characteristic length, we can obtain the non-closed momentum equation

$$\begin{aligned} & \frac{\partial}{\partial t} (\rho_f \varepsilon_f \langle \mathbf{v}_f \rangle^f) + \nabla \cdot (\varepsilon_f \rho_f \langle \mathbf{v}_f \rangle^f \langle \mathbf{v}_f \rangle^f) + \nabla \cdot (\varepsilon_f \rho_f \langle \tilde{\mathbf{v}}_f \tilde{\mathbf{v}}_f \rangle^f) + \frac{1}{V} \int_{A_{fs}} \mathbf{n}_{fs} \cdot (\mathbf{v}_f - \\ & \mathbf{w}_{fs}) \rho_f \mathbf{v}_f dA = -\varepsilon_f \nabla \langle P_f \rangle^f + \varepsilon_f \mu_f \nabla^2 \langle \mathbf{v}_f \rangle^f + \frac{1}{V} \int_{A_{fs}} \mathbf{n}_{fs} \cdot (-\tilde{P}_f \mathbf{I} + \mu_f \nabla \tilde{\mathbf{v}}_f) dA + \mu_f \nabla \cdot \\ & \left(\frac{1}{V} \int_{A_{fs}} \mathbf{n}_{fs} \tilde{\mathbf{v}}_f dA \right). \end{aligned} \quad (2-14)$$

e. Develop the closure problem. In this step, we use the deviation term $\tilde{\mathbf{v}}_f$ and \tilde{P}_f to represent the intrinsic value of pressure $\langle P_f \rangle^f$ and velocity $\langle \mathbf{v}_f \rangle^f$. We obtain

$$\rho_f \mathbf{v}_f \cdot \nabla \tilde{\mathbf{v}}_f = -\nabla \tilde{P}_f + \mu_f \nabla^2 \tilde{\mathbf{v}}_f - \frac{1}{V} \int_{A_{fs}} \mathbf{n}_{fs} \cdot (-\tilde{P}_f \mathbf{I} + \mu_f \nabla \tilde{\mathbf{v}}_f) dA, \quad (2-15)$$

$$\text{and } \nabla \cdot \tilde{\mathbf{v}}_f = 0, \quad (2-16)$$

with the boundary conditions

$$\tilde{\mathbf{v}}_f = -\langle \mathbf{v}_f \rangle^f \quad \text{at } A_{fs}, \quad (2-17)$$

$$\text{and } \tilde{P}_f(\mathbf{r} + l_i) = \tilde{P}_f(\mathbf{r}), \quad \tilde{\mathbf{v}}_f(\mathbf{r} + l_i) = \tilde{\mathbf{v}}_f(\mathbf{r}), \quad i = 1, 2, 3 \quad \text{at } A_{fe}. \quad (2-18)$$

f. After solving the above closure problem, we can obtain the mapping equation, the detail about the solution of the closure problem can be found in (Bousquet-Melou et al., 2002)

$$\frac{1}{V} \int_{A_{fs}} \mathbf{n}_{fs} \cdot (-\tilde{P}_f \mathbf{I} + \mu_f \nabla \tilde{\mathbf{v}}_f) dA = -\varepsilon_f^2 \mu_f \mathbf{K}^{-1} \cdot \langle \mathbf{v}_f \rangle^f - \varepsilon_f^2 \mu_f \mathbf{K}^{-1} \cdot \mathbf{F} \cdot \langle \mathbf{v}_f \rangle^f, \quad (2-19)$$

where, K is the permeability tensor, and F is the Forchheimer correction tensor which accounts for microscopic inertia effects.

g. Simplifying the Eq. (2-14) with estimating the order can obtain the equation

$$\frac{\partial \varepsilon_f \rho_f \langle v_f \rangle^f}{\partial t} + \nabla \cdot \varepsilon_f \rho_f \langle v_f \rangle^f \langle v_f \rangle^f = -\varepsilon_f \nabla \langle P_f \rangle^f + \varepsilon_f \mu_f \nabla^2 \langle v_f \rangle^f + \frac{1}{V} \int_{A_{fs}} \mathbf{n}_{fs} \cdot (-\tilde{P}_f \mathbf{I} + \mu_f \nabla \tilde{v}_f) dA. \quad (2-20)$$

Substituting the mapping from the closure problem can obtain

$$\frac{\partial \varepsilon_f \rho_f \langle v_f \rangle^f}{\partial t} + \nabla \cdot \varepsilon_f \rho_f \langle v_f \rangle^f \langle v_f \rangle^f = -\varepsilon_f \nabla \langle P_f \rangle^f + \varepsilon_f \mu_f \nabla^2 \langle v_f \rangle^f + -\varepsilon_f^2 \mu_f \mathbf{K}^{-1} \cdot \langle v_f \rangle^f - \varepsilon_f^2 \mu_f \mathbf{K}^{-1} \cdot \mathbf{F} \cdot \langle v_f \rangle^f. \quad (2-21)$$

Forchheimer correction tensor is accounted for the inertia effects under higher Reynolds number, such as in the transient flow regime. In our problem, the Reynolds number is low, and the flow can be regarded as the Darcy flow. In Darcy flow, the viscosity dominates the flow, and the inertia effect can be neglected. Thus, we can finally obtain the DBS momentum equation

$$\frac{1}{\varepsilon_f} \left(\frac{\partial \rho_f \bar{v}_f}{\partial t} + \nabla \cdot \left(\frac{\rho_f}{\varepsilon_f} \bar{v}_f \bar{v}_f \right) \right) = -\nabla \bar{p}_f + \frac{\mu_f}{\varepsilon_f} \nabla^2 \bar{v}_f - \mu_f k^{-1} \bar{v}_f, \quad (2-22)$$

where, \bar{v}_f is the average velocity; \bar{p}_f is the average pressure; μ_f is the dynamic viscosity; ρ_f is the fluid density in the system. The last term ($\mu_f k^{-1} \bar{v}_f$) is Darcy resistance term (Soulaine et al., 2017). k is the local permeability, which is computed by the Kozeny–Carman relationship:

$$k^{-1} = k_0^{-1} \frac{(1-\varepsilon_f)^2}{\varepsilon_f^3}, \quad (2-23)$$

where, k_0 is the initial local permeability which should be small enough. In our work, we take the k_0 as 10^{-15} .

2.3 Discretization of the DBS equation using Finite Volume Method

The Finite Volume Method (FVM) was used to discretize the partial differential equations into algebraic format. The value of the variables always saved on the centroid of the

control volume. We assumed that the variables have linear distribution in both space and time. For the simplicity, P represents the owner cell and N represents the neighboring cell; F represents the value on the face of control volume, which also represents the point in the middle of the face. Take the integral form of each term in the momentum equation except the gradient of pressure, and we get

$$\int_t^{t+\Delta t} \frac{1}{\varepsilon_f} \left[\frac{\partial}{\partial t} \int_{VP} \rho_f \bar{v}_f dV + \int_{VP} \nabla \cdot \left(\frac{\rho_f}{\varepsilon_f} \bar{v}_f \bar{v}_f \right) dV \right] dt = \int_t^{t+\Delta t} \left[\int_{VP} \frac{\mu_f}{\varepsilon_f} \nabla^2 \bar{v}_f dV - \int_{VP} \mu_f k^{-1} \bar{v}_f dV \right] dt. \quad (2-24)$$

Apply the Gauss's theorem and obtain the equation

$$\int_t^{t+\Delta t} \left[\frac{1}{\varepsilon_f} \frac{\partial}{\partial t} (\rho_f \bar{v}_f)_P V_P + \frac{1}{\varepsilon_f} \int_A \left(\frac{\rho_f}{\varepsilon_f} \bar{v}_f \right) \bar{v}_f \cdot \vec{n} dA - \int_A \frac{\mu_f}{\varepsilon_f} \nabla \bar{v}_f \cdot \vec{n} dA \right] dt = - \int_t^{t+\Delta t} S_P \bar{v}_f V_P dt, \quad (2-25)$$

where, S_P denotes the source term of the momentum equation, which equals to $S_P = \mu_f k^{-1}$.

The convection term can be written as

$$\int_A \left(\frac{\rho_f}{\varepsilon_f} \bar{v}_f \right) \bar{v}_f \cdot \vec{n} dA = \sum_F \left(\frac{\rho_f}{\varepsilon_f} \bar{v}_f \right)_F \bar{v}_{f,F} \cdot \vec{n}_{i,F} A_F = \sum_F F \bar{v}_{f,F}, \quad (2-26)$$

where, F is the flux through the face and has

$$F = \left(\frac{\rho_f}{\varepsilon_f} \bar{v}_f \right)_F \cdot \vec{n}_{i,F} A_F. \quad (2-27)$$

The diffusion term has the equation

$$\int_A \frac{\mu_f}{\varepsilon_f} \nabla \bar{v}_f \cdot \vec{n} dA = \sum_F \left(\frac{\mu_f}{\varepsilon_f} \right)_F (\nabla \bar{v}_f)_F \cdot \vec{n}_{i,F} A_F. \quad (2-28)$$

We use Euler Implicit method to discretize the temporal term. Since Euler Implicit method guarantees boundness and is very stable. It has the first order accuracy. The Euler

Implicit method express the face-values in terms of the new time level (Jasak, 1996). The semi-discrete form of momentum equation can be written as

$$\frac{1}{\varepsilon_f} V_P \frac{\partial}{\partial t} (\rho_f \bar{v}_f)_P + \sum_F F \bar{v}_{f,F} - \sum_F \left(\frac{\mu_f}{\varepsilon_f} \right)_F (\nabla \bar{v}_f)_F \cdot \vec{n}_{i,F} A_F = -\nabla \bar{p}_f - S_P \bar{v}_f V_P. \quad (2-29)$$

The convection term was interpolated by the upwind scheme, and we use the symbol $\|a, b\|$ to represent the maximum value between a and b . According to the Euler Implicit method and the upwind scheme, we have the equation for the convection term

$$\sum_F F \bar{v}_{f,F}^{t+\Delta t} = \sum_F (\|F, 0\| \bar{v}_{f,P}^{t+\Delta t} - \|-F, 0\| \bar{v}_{f,N}^{t+\Delta t}). \quad (2-30)$$

We have the diffusion term

$$\sum_F \left(\frac{\mu_f}{\varepsilon_f} \right)_F (\nabla \bar{v}_f)_F \cdot \vec{n}_{i,F} A_F = \sum_F \left(\frac{\mu_f}{\varepsilon_f} \right)_F \frac{\bar{v}_{f,N}^{t+\Delta t} - \bar{v}_{f,P}^{t+\Delta t}}{\mathbf{d}} \cdot \frac{\vec{A}_F}{A_F} A_F = \sum_F \left(\frac{\mu_f}{\varepsilon_f} \right)_F \frac{\bar{v}_{f,N}^{t+\Delta t} - \bar{v}_{f,P}^{t+\Delta t}}{|\mathbf{d}|} A_F, \quad (2-31)$$

where, \mathbf{d} is the vector between two grids; \vec{A}_F is the vector normal to the cell face. The above equation can be arranged as

$$\frac{1}{\varepsilon_f} V_P \frac{\rho_{f,P}^{t+\Delta t} \bar{v}_{f,P}^{t+\Delta t} - \rho_{f,P}^t \bar{v}_{f,P}^t}{\Delta t} + a_P \bar{v}_{f,P}^{t+\Delta t} - \sum_F a_N \bar{v}_{f,N}^{t+\Delta t} = -\nabla \bar{p}_f^{t+\Delta t} - S_P \bar{v}_{f,P}^{t+\Delta t} V_P, \quad (2-32)$$

where, S_P is the source term and calculated by $S_P = \mu_f k^{-1}$; k^{-1} is calculated by $k^{-1} = k_0^{-1} \frac{(1 - \varepsilon_f^{t+\Delta t})^2}{\varepsilon_f^{t+\Delta t^3}}$. The coefficients a_P and a_N are composed by the convection, diffusion fluxes across the cell face, interpolation schemes, and gradient schemes. a_P is the coefficient for the centroid cell, and a_N is the coefficient for the influenced neighboring control volumes, respectively. a_P and a_N can be written as

$$a_P = \sum_F \|F, 0\| + \sum_F \left(\frac{\mu_f}{\varepsilon_f} \right)_F \frac{A_F}{|\mathbf{d}|}, \quad (2-33)$$

$$\text{and } a_N = \|F, 0\| - \left(\frac{\mu_f}{\varepsilon_f} \right)_F \frac{A_F}{|\mathbf{d}|}. \quad (2-34)$$

The above equation can be arranged as

$$\left(\frac{V_P}{\Delta t \varepsilon_f} + S_P V_P + a_P\right) \bar{v}_{f,P}^{t+\Delta t} = \sum_F a_N \bar{v}_{f,N}^{t+\Delta t} - \nabla \bar{p}_f^{t+\Delta t} + \frac{V_P}{\Delta t \varepsilon_f} \rho_{f,P}^t \bar{v}_{f,P}^t. \quad (2-35)$$

Then, use $A_P = \frac{V_P}{\Delta t \varepsilon_f} + S_P V_P + a_P$ and $S_u = \frac{V_P}{\Delta t \varepsilon_f} \rho_{f,P}^t \bar{v}_{f,P}^t$ to substitute in the above equation

Eq. (2-35). A_P is the diagonal term of the matrix. We write the above equation in the form:

$$A_P \bar{v}_{f,P}^{t+\Delta t} = \sum_F a_N \bar{v}_{f,N}^{t+\Delta t} - \nabla \bar{p}_f^{t+\Delta t} + S_u. \quad (2-36)$$

Use the operator $\mathbf{H}(\bar{v}^{t+\Delta t}) = \sum_F a_N \bar{v}_{f,N}^{t+\Delta t} + S_u$ to substitute in the above equation

$$A_P \bar{v}_{f,P}^{t+\Delta t} = \mathbf{H}(\bar{v}^{t+\Delta t}) - \nabla \bar{p}_f^{t+\Delta t}. \quad (2-37)$$

Apply Green–Gauss theorem and Green–Gauss Cell Based scheme to discretize the gradient of pressure

$$\nabla \bar{p}_f^{t+\Delta t} = \frac{1}{V_P} \sum_F A_F \bar{p}_{f,F}^{t+\Delta t} = \frac{1}{V_P} \sum_F A_F \frac{\bar{p}_{f,N}^{t+\Delta t} + \bar{p}_{f,P}^{t+\Delta t}}{2}. \quad (2-38)$$

The above equation is the semi–discretized form of momentum equation. Thus, we divided A_P for each term. After taking the divergence of each term, and substitute the continuity equation

$\nabla \cdot \bar{v}_{f,P}^{t+\Delta t} = 0$, Eq. (2-37) can be written into

$$\nabla \cdot \bar{v}_{f,P}^{t+\Delta t} = \nabla \cdot \frac{\mathbf{H}(\bar{v}^{t+\Delta t})}{A_P} - \nabla \cdot \frac{\nabla \bar{p}_f^{t+\Delta t}}{A_P}, \quad (2-39)$$

$$\text{and } 0 = \nabla \cdot \frac{\mathbf{H}(\bar{v}^{t+\Delta t})}{A_P} - \nabla \cdot \frac{\nabla \bar{p}_f^{t+\Delta t}}{A_P}. \quad (2-40)$$

Then, we obtain the Poisson equation for pressure

$$\nabla \cdot \frac{\mathbf{H}(\bar{v}^{t+\Delta t})}{A_P} = \nabla \cdot \frac{\nabla \bar{p}_f^{t+\Delta t}}{A_P}. \quad (2-41)$$

2.4 PISO algorithm

The momentum equation shows linear dependence of velocity on pressure and vice-versa (Jasak, 1996). We need a coupling method to treat with the momentum equation. The

most common method for solving the transient incompressible problem is Pressure–Implicit with Splitting of Operators (PISO) algorithm (Jasak, 1996). In PISO algorithm, the equations are solved in sequence. The PISO algorithm can be described as follows.

First, we solve the following equation to calculate the predicted velocity ($\bar{v}_{f,P}^*$), which is known as momentum predictor. The exact value for pressure at the current time step is unknown, and we use the pressure of previous time step instead. Thus, the predicted velocity does not satisfy the continuity equation so far. We have the equation

$$A_P \bar{v}_{f,P}^* = \sum_F a_N \bar{v}_{f,N}^* - \nabla \bar{p}_f^t + S_u^t = \sum_F a_N \bar{v}_{f,N}^* - \sum_F A_F \bar{p}_{f,F}^t + S_u^t. \quad (2-42)$$

Within the certain time step, the coefficient A_P , a_N , S_u^t remain unchanged. We have obtained the predicted velocity so far. However, the predicted velocity will not guarantee the continuity equation, which still needs iterative correction.

Under the convergent condition, the pressure and velocity of the next time step satisfy $A_P \bar{v}_{f,P}^{t+\Delta t} = \sum_F a_N \bar{v}_{f,N}^{t+\Delta t} - \nabla \bar{p}_f^{t+\Delta t} + S_u^t = \sum_F a_N \bar{v}_{f,N}^{t+\Delta t} - \sum_F A_F \bar{p}_{f,F}^{t+\Delta t} + S_u^t$. (2-43)

The above equation is accurate since we don't have any omitted term on the above equation. Let Eq.(2-43) substitute Eq. (2-42)

$$A_P \bar{v}'_{f,P} = \sum_F a_N \bar{v}'_{f,N} - \sum_F A_F \bar{p}'_{f,F}, \quad (2-44)$$

where, $\bar{v}'_{f,P} = \bar{v}_{f,P}^{t+\Delta t} - \bar{v}_{f,P}^*$, and $\bar{p}'_{f,F} = \bar{p}_{f,F}^{t+\Delta t} - \bar{p}_{f,F}^*$. By ignoring the influence of neighboring cell, the above equation can be written into

$$A_P \bar{v}'_{f,P} = \sum_F A_F \bar{p}'_{f,F}. \quad (2-45)$$

Add the above equation to Eq. (2-42):

$$A_P \bar{v}_{f,P}^{**} = \sum_F a_N \bar{v}_{f,N}^* - \sum_F A_F \bar{p}_{f,F}^* + S_u^t, \quad (2-46)$$

where, $\bar{v}_{f,P}^{**} = \bar{v}_{f,P}^* + \bar{v}'_{f,P}$, $\bar{p}_{f,F}^* = \bar{p}_{f,F}^t + \bar{p}'_{f,F}$. Arrange the above equation:

$$\bar{v}_{f,P}^{**} = \frac{1}{A_P} (\sum_F a_N \bar{v}_{f,N}^* + S_u^t) - \frac{1}{A_P} \sum_F A_F \bar{p}_{f,F}^*. \quad (2-47)$$

Use the notation $\mathbf{H}(\bar{v}^{t+\Delta t}) = \sum_F a_N \bar{v}_{f,N}^{t+\Delta t} + S_u$ to represent the above equation

$$\bar{v}_{f,P}^{**} = \frac{1}{A_P} \mathbf{H}(\bar{v}^*) - \frac{1}{A_P} \sum_F A_F \bar{p}_{f,F}^*. \quad (2-48)$$

Then we can obtain this Poisson equation for pressure for the predicted value with $\nabla \cdot$

$$\bar{v}_{f,P}^{**} = 0$$

$$\nabla \cdot \frac{1}{A_P} \mathbf{H}(\bar{v}^*) = \nabla \cdot \left(\frac{1}{A_P} \nabla \bar{p}_{f,F}^* \right). \quad (2-49)$$

We can obtain the predicted pressure $\bar{p}_{f,F}^*$ from the predicted velocity \bar{v}^* by solving the above equation. Then substituting the predicted pressure into Eq.(2-49) and repeating this process for several times can decrease the error between the predicted value with the convergent value.

2.5 Derivation of mass balance equation

The change of the mass of species within the control volume has the following relationship (Bear & Buchlin, 1991):

$$\boxed{\begin{array}{c} \text{Change of the} \\ \text{mass of species } i \\ \text{over time } \Delta t \end{array}} = \boxed{\begin{array}{c} \text{Surface flux of the} \\ \text{mass of species } i \\ \text{over time } \Delta t \text{ across} \\ \text{the control volume} \end{array}} + \boxed{\begin{array}{c} \text{Source/sink of the} \\ \text{mass of species } i \\ \text{overtime } \Delta t \end{array}}. \quad (2-50)$$

For the fixed control volume, the change of the mass of species over time within the material volume can be written as Reynolds Transport theorem as

$$\frac{d}{dt} \int_{MV} \rho_f \omega_{f,i} dV, \quad (2-51)$$

where, ω_i is the volume species i per unit volume fluid, F is the flux on the differential element surface (mass per unit area per unit time) and has the following relationship

$$F = v_i \rho_f \omega_{f,i} - \varepsilon_f \rho_f D_m \left(\frac{\partial \omega_{f,i}}{\partial x} + \frac{\partial \omega_{f,i}}{\partial y} + \frac{\partial \omega_{f,i}}{\partial z} \right). \quad (2-52)$$

The first term of the right-hand side is the Flux of species i flowing over the differential element, and the second term of right-hand side is the Flux of species i by the diffusion from Fick's Law.

The conversion of mass has the relationship

$$\dot{m}_{in} - \dot{m}_{out} \pm \dot{m}_{source/sink} = \dot{m}_{change}, \quad (2-53)$$

The volume of mass flow through the differential element has the equation

$$\begin{aligned} & \rho_f \varepsilon_f \Delta x \Delta y \Delta z [C_{f,i}(\Delta t + t) - C_{f,i}(t)] \pm \dot{m}_{source/sink} = \Delta t \Delta y \Delta z \left[F \left(x - \frac{\Delta x}{2}, y, z \right) - \right. \\ & F \left(x + \frac{\Delta x}{2}, y, z \right) \left. \right] + \Delta t \Delta x \Delta z \left[F \left(y - \frac{\Delta y}{2}, x, z \right) - F \left(y + \frac{\Delta y}{2}, x, z \right) \right] + \Delta t \Delta y \Delta z \left[F \left(z - \right. \right. \\ & \left. \left. \frac{\Delta z}{2}, x, y \right) - F \left(z + \frac{\Delta z}{2}, x, y \right) \right]. \end{aligned} \quad (2-54)$$

After arranging the above equation gives, we have

$$\begin{aligned} & \frac{\varepsilon_f \rho_f [\omega_{f,i}(\Delta t + t) - \omega_{f,i}(t)]}{\Delta t} \pm \dot{m}_{source/sink} = \frac{[F(x - \frac{\Delta x}{2}, y, z) - F(x + \frac{\Delta x}{2}, y, z)]}{\Delta x} + \\ & \frac{[F(y - \frac{\Delta y}{2}, x, z) - F(y + \frac{\Delta y}{2}, x, z)]}{\Delta y} + \frac{[F(z - \frac{\Delta z}{2}, x, y) - F(z + \frac{\Delta z}{2}, x, y)]}{\Delta z}. \end{aligned} \quad (2-55)$$

Take the limit the above equation, and we have

$$\begin{aligned} & \lim_{\Delta t \rightarrow 0} \frac{\varepsilon_f \rho_f [\omega_{f,i}(\Delta t + t) - \omega_{f,i}(t)]}{\Delta t} + \lim_{\Delta x \rightarrow 0} \frac{[F(x + \frac{\Delta x}{2}, y, z) - F(x - \frac{\Delta x}{2}, y, z)]}{\Delta x} + \\ & \lim_{\Delta y \rightarrow 0} \frac{[F(y + \frac{\Delta y}{2}, x, z) - F(y - \frac{\Delta y}{2}, x, z)]}{\Delta y} + \lim_{\Delta z \rightarrow 0} \frac{[F(z + \frac{\Delta z}{2}, x, y) - F(z - \frac{\Delta z}{2}, x, y)]}{\Delta z} = \dot{m}_{source/sink}. \end{aligned} \quad (2-56)$$

The above equation can be reduced into the form

$$\frac{\partial \rho_f \varepsilon_f \omega_{f,i}}{\partial t} + \frac{\partial F}{\partial x} + \frac{\partial F}{\partial y} + \frac{\partial F}{\partial z} = \dot{m}_{source/sink}. \quad (2-57)$$

Substitute Eq. (2-52) in the above equation

$$\begin{aligned} \frac{\partial \varepsilon_f \rho_f \omega_{f,i}}{\partial t} + \frac{\partial v_x \rho_f \omega_{f,i}}{\partial x} + \frac{\partial v_y \rho_f \omega_{f,i}}{\partial y} + \frac{\partial v_z \rho_f \omega_{f,i}}{\partial z} &= \frac{\partial}{\partial x} (\varepsilon_f \rho_f D_m \frac{\partial \omega_{f,i}}{\partial x}) + \frac{\partial}{\partial y} (\varepsilon_f \rho_f D_m \omega_{f,i}) + \\ \frac{\partial}{\partial z} (\varepsilon_f \rho_f D_m \frac{\partial \omega_{f,i}}{\partial z}) &+ \dot{m}_{source/sink}. \end{aligned} \quad (2-58)$$

We finally obtain the equation

$$\frac{\partial \varepsilon_f \rho_f \omega_{f,i}}{\partial t} + \nabla \cdot (u_f \rho_f \omega_{f,i}) = \nabla \cdot (\varepsilon_f \rho_f D_i \nabla \omega_{f,i}) + m_i. \quad (2-59)$$

The temporal term is discretized with the Euler Implicit scheme. The convection term is discretized by the linear upwind scheme, which has the second-order accuracy.

2.6 Summary of the governing equations and solution sequence

We summarized the governing equations in Table 2-1. The equations can be used to describe the reactive transport and mineral–fluid interactions. The mass dissolution rate (\dot{m}) and chemical reaction rate (\dot{m}_A) have a relationship of $\dot{m} = \beta \dot{m}_A$, where β is a stoichiometric coefficient. For the reaction between hydrochloric acid and carbonate, β equals to $M_{CaCO_3}/2M_{HCl}=1.37$.

Table 2-1 The governing equations of pore-scale model to describe the dissolution

Equation names	Main governing equations	Supplemental equations
Darcy–Brinkman– Stokes momentum equation	$\frac{1}{\varepsilon_f} \left(\frac{\partial \rho_f \bar{v}_f}{\partial t} + \nabla \cdot \left(\frac{\rho_f}{\varepsilon_f} \bar{v}_f \bar{v}_f \right) \right) = -\nabla \bar{p}_f + \frac{\mu_f}{\varepsilon_f} \nabla^2 \bar{v}_f - \mu_f k^{-1} \bar{v}_f$	$k^{-1} = k_0^{-1} \frac{(1-\varepsilon_f)^2}{\varepsilon_f^3}$
Advection–diffusion equation	$\frac{\partial \varepsilon_f \rho_f \bar{\omega}_{f,A}}{\partial t} + \nabla \cdot (\rho_f \bar{v}_f \bar{\omega}_{f,A}) = \nabla \cdot (\varepsilon_f \rho_f D_A^* \nabla \bar{\omega}_{f,A}) - \dot{m}_A$	$\varepsilon_f D_A^* = \varepsilon_f^2 D_A$ $\dot{m}_A = \rho_f a_v k_r \bar{\omega}_{f,A}$
Mass balance equation	$\frac{\partial \varepsilon_s \rho_s}{\partial t} = -\dot{m}$ $\frac{\partial \varepsilon_f \rho_f}{\partial t} + \nabla \cdot (\rho_f \bar{v}_f) = -\dot{m}$	$\dot{m} = \beta \dot{m}_A$ $a_v = \ \nabla \varepsilon\ \psi$ $\psi = 4\varepsilon_f(1 - \varepsilon_f)$

The pore-scale dissolution and transport model is developed based on OpenFOAM, an open-source Computational Fluid Dynamics (CFD) platform (Weller, Tabor, Jasak, & Fureby, 1998). This work was done by additionally describing the relevant physical-and-chemical phenomena in the sources codes of pisoFOAM, which was originally designed to solve the incompressible transient flow (Leal, 1992). The partial differential equations were discretized into linear algebraic equations by the Finite Volume Method (FVM). The geometry models were generated by the open-source 3-D computer graphics software Blender (Blender Foundation, 1994). The initial volume fractions of the pores were initialized and the boundary condition is as follows: $\bar{v}_f|_{t=0} = \bar{v}_{f0}$, $\bar{v}_f|_{x=0} = \bar{v}_{f0}$, $\frac{\partial \bar{p}_f}{\partial n}|_{x=0} = 0$, $\bar{p}_f|_{x=x_0} = \bar{p}_{out}$, $\bar{\omega}_{f,A}|_{x=0} = \bar{\omega}_{f,A0}$, and $\bar{\omega}_{f,A}|_{t=0} = 0$. We used the relative pressure in this work regarding the incompressible flow. The top and bottom walls were set as non-slip boundary condition which has $\bar{v}_f = 0$. The governing equations were solved by the following procedures: (1) we first assigned the solid zone and fluid zone over the control volume; (2) we calculated the relevant

parameters such as mass transfer rates by chemical reactions, local permeability (which will be used in the Darcy resistance term in the momentum equation), effective diffusion coefficient, and then solved the advection–diffusion equation to get concentration of species; (3) the mass transfer rate was updated using the new concentration of species; (4) the mass conservation equation was solved to get the local porosity; (5) Pressure–Implicit with Splitting of Operators (PISO) algorithm was implemented to solve the DBS momentum equation; (6) iterated from the step (2) until the simulation end time. The calculation step is shown in Fig. 2-4.

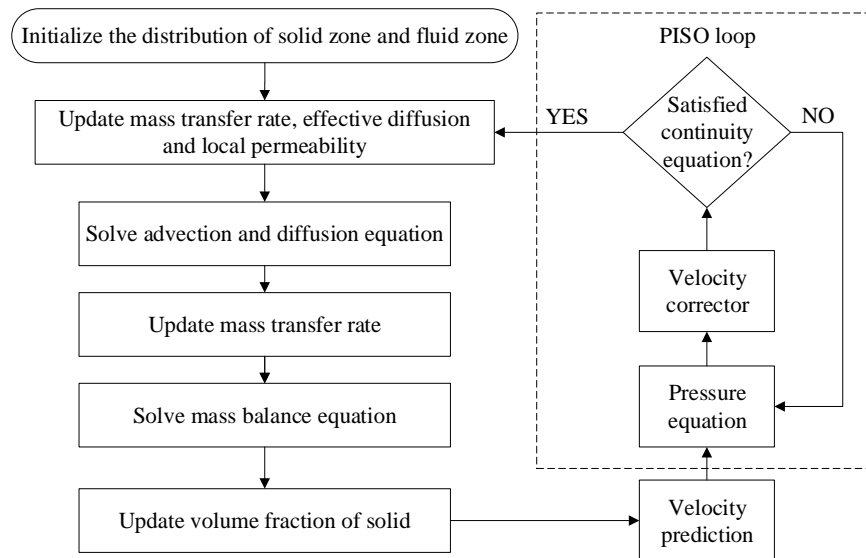


Fig. 2-4 The solution sequence for the numerical method.

3 PORE-SCALE MODEL FOR ACID DISSOLUTION

3.1 Application of Darcy–Brinkman–Stokes equation in pore–scale model

DBM solves the equations over the control volume for both solid and fluid zone. The structured Cartesian meshes were used to discretize the control volume, which provides high computational efficiency and easy implementation to the description and computation of problems in the porous media with complex geometry.

We employed the DBS method and used structured Cartesian meshes to describe the complex pore structure. The method avoids regenerating mesh after the solid–liquid boundary evolution induced by the chemical reaction. In this way, we take advantage of the uniform, structured grids while making it possible to solve the Partial Difference Equations (PDE) stably and efficiently. The evolution of the pore structure can be clearly tracked during the acidizing. In addition, it also enables us to consider multi–mineral compositions in a flexible way. The pore–scale model is defined as the scale at which each point of space is occupied by a specific phase, whether fluid or solid (Molins et al., 2020). The whole computational domain is discretized into structured grids on which the momentum, advection–diffusion, and mass balance equations are calculated. In this way, the spatial distribution of solid and fluid zones can be accurately distinguished; the evolution of solid–liquid interface is dynamically tracked as acid dissolves the rock, and the variation of acid distribution due to the chemical reaction and changing pore structures is described. As shown in Fig. 3-1, in Darcy–scale modelling, porosity (ϕ) is used to measure the void fraction of the porous media, which is in the range from 0 to 1. In pore–scale modelling, local porosity (ε) represents the volume fraction of pore zone or solid zone within a control volume. Within a control volume of the fluid area, $\varepsilon_f = 1$, and $\varepsilon_s = 0$. For solid zone, $\varepsilon_f = 0$, and $\varepsilon_s = 1$. ε_f and ε_s have the relationship of $\varepsilon_s + \varepsilon_f = 1$. In

the DBS method, Darcy's law describes the solid–liquid interface, where $0 < \varepsilon_f < 1$. The governing equations are listed in Table 1 (Soulaine et al., 2017; Soulaine & Tchelepi, 2016).

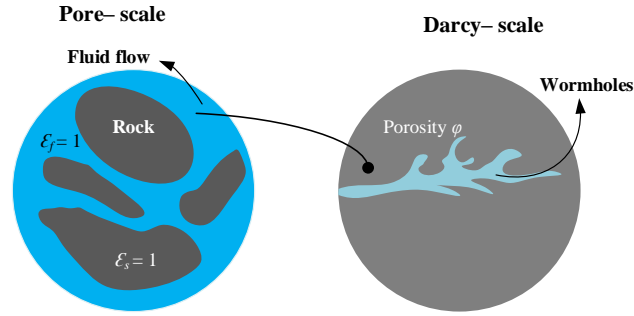


Fig. 3-1 Schematic graph showing the different scale simulations. Darcy-scale model uses porosity (φ) to describe the porous media with the range from 0 to 1.

Fig. 3-2 is the example of implementing the DBS pore-scale model on the digital rock. In the digital rock image (left hand side), the red color represents the fluid zone, and the blue color represents the solid zone. In the fluid zone, $\varepsilon_f = 1$, and $\varepsilon_s = 0$. Here, the Darcy resistance term ($\mu_f k^{-1} \bar{v}_f$) becomes zero, and the DBS momentum equation turns into normal Navier–Stokes equation. In the solid zone, $\varepsilon_f = 0$, and $\varepsilon_s = 1$. Here, the Darcy resistance term reaches to 10^{15} magnitude and is treated as the sink term by its negative sign. Thus, the velocity in the solid zone is zero. In the solid–fluid interface, the fluid flow is solved by the DBS equation of Eq. (2-22).

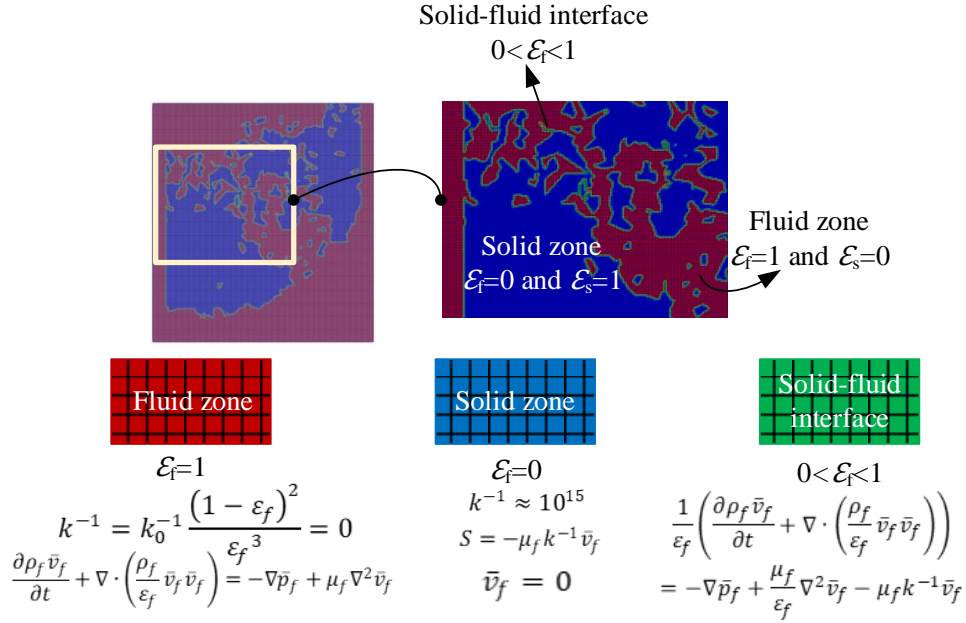


Fig. 3-2 The example of pore-scale model on the digital rock.

3.2 Rate law and solid-liquid interface

The reaction rate law can be used to describe the reaction rate on the mineral surface

$$R = \frac{1}{v_{mi}} \frac{dN_i}{dt} = \frac{d\omega_i}{dt} = k_r a_v \omega_i \left(1 - \frac{Q}{K_m}\right), \quad (3-1)$$

where, N_i is the molar concentration of species i ; ω_i is the concentration of the species i with the unit of %. k_r is the reaction rate constant. When the rate law is the first order correlation, k_r has the unit of m/s. When the rate is the second order correlation, k_r has the unit of mol/m²s for the second order rate law. Q is the ion activity product, and K_m is the equilibrium constant. a_v is the reactive surface area with unit of 1/m, which can be approximated by the effective surface area or the specific surface area. In this study, we used the effective surface area a_v to quantify the reactive surface area. The effective surface area can be defined as the surface area to the volume.

According to the volume averaging theorem, the surface area of the control volume can be calculated as

$$A = \int_{A_{fs}} \mathbf{n}_{fs} dA. \quad (3-2)$$

After dividing the volume of the control volume, we have

$$-\nabla \varepsilon_f = \frac{1}{V} \int_{A_{fs}} \mathbf{n}_{fs} dA, \quad (3-3)$$

$$\text{and } a_v = \|\nabla \varepsilon_f\|. \quad (3-4)$$

The volume fraction of fluid is 1 in the liquid zone, and the volume fraction of fluid is 0 in the solid zone. Thus, we calculated the magnitude of the gradient of the volume fraction of fluid to obtain the effective surface area. Only on the solid–liquid interface, there is non–zero value of the effective surface area. The value of the effective surface area is zero in the solid zone and fluid zone. After calculating the mass transfer rate by multiplying the effective surface area, the solid zone and fluid zone have zero mass transfer rate by reaction, and solid–liquid interface has non–zero value of the mass transfer rate. In addition, we multiply the effective surface area to a function that characterizes the diffuse interface to enforce the localization of the reactive boundary solution at the solid–liquid interface (Luo, Quintard, Debenest, & Laouafa, 2012). The function that characterizes the diffuse interface is $\psi = 4\varepsilon_f(1 - \varepsilon_f)$. In this way, we can guarantee that the effective surface area is only non–zero at liquid–solid interface.

3.3 Numerical method validation

To validate the developed pore–scale DBS model in simulating the dissolution of minerals such as calcite, we compared the numerical results with the experimental results and confirmed that our numerical results are in accordance with the values reported in the published

study under similar conditions (Soulaine et al., 2017). This work has been published in (You & Lee, 2021b).

We conducted the numerical simulation using a 2-D model with a 1.5 mm × 1.5 mm computational domain, which was discretized into 100 × 100 Cartesian grids. An octagonal calcite, which had the same shape and size with the experiment, was used to initialize the volume fraction of the solid zone. The schematic geometry model and boundary condition are shown in Fig. 3-3. The second Damköhler number (Da_{II}) and Péclet (Pe) number were about 500 and 15, respectively. When hydrochloride acid reacted with calcite, these dimensionless numbers changed due to the variation of characteristic length, and the indicated Da_{II} and Pe in each case results are the values, which were estimated at the initial stage. The dimensionless numbers are calculated as

$$Da_{II} = \frac{r}{a_v D_A}, \quad (3-5)$$

$$Pe = \frac{v_o l}{D_A} = \frac{v_o \sqrt{K}}{D_A}, \quad (3-6)$$

$$\text{and } Re = \frac{\rho v_o l}{\mu} = \frac{\rho v_o \sqrt{K}}{\mu}, \quad (3-7)$$

where a_v is the volume-averaged effective surface area; Re is the Reynolds number; v_o is the injection velocity; l is the characteristic length of porous media and related to the pore throat size in the flow pathway (Soulaine et al., 2017). We used the square root of permeability of porous media to calculate the characteristic length. K is the volume-averaged absolute permeability for entire domain, which is computed by arranging the Darcy's law

$$K = -\frac{\bar{v}_f \mu_f}{\nabla \bar{p}_f}, \quad (3-8)$$

where, K is computed by the volume-averaged velocity and pressure gradient of the control volume. We only considered the permeability in the flow direction while computing the above

parameters. The input parameters are listed in Table 3-1. The experiment was conducted under the atmospheric pressure (0.1 MPa) and temperature was 25 °C. Thus, we assumed that numerical simulation in Chapter 3 to Chapter 5 had the same temperature of 25 °C under atmospheric pressure. We also assumed that the cases had liquid water saturation of 1.

Table 3-1 Input parameters in the simulation case for the validation (Soulaine & Tchelepi, 2016).

Parameter	Symbol	Value
Fluid density	ρ_l	920 kg·m ⁻³
Fluid viscosity	μ_l	2.4 × 10 ⁻³ Pa·s
Injection velocity	v_{inj}	1.16 × 10 ⁻³ m·s ⁻¹
Reaction constant	k_r	5 × 10 ⁻³ m·s ⁻¹
Molecular diffusivity of acid	D_A	5 × 10 ⁻⁹ m ² ·s ⁻¹
Density of calcite	ρ_s	2710 kg·m ⁻³
Inlet acid concentration	$\bar{\omega}_{f,A}$	0.05 wt%

Fig. 3-4 (a) shows the change of calcite while injecting acid during the experiment and simulation. The calcite was elongated and displayed an oval–shape. This was due to the asymmetrical distribution of acid in the domain. Advective flow dominated the system, and fluid velocity was lower on the right–hand side. Thus, more acid was transported to the left–hand side of calcite. The changing solid mass and normalized surface area (a_v) are plotted in Fig. 3-4 (b) and Fig. 3-4 (c), respectively. The numerical results are in accordance with the experimental results. There is an insignificant deviation between the numerical simulation results and experimental results, which can be explained by the unknown information on the first–order reaction rate, which resulted in the uncertainty in estimating the actual reaction rate and the roughness of calcite surface (Guo, Laouafa, & Quintard, 2016; Soulaine et al., 2017).

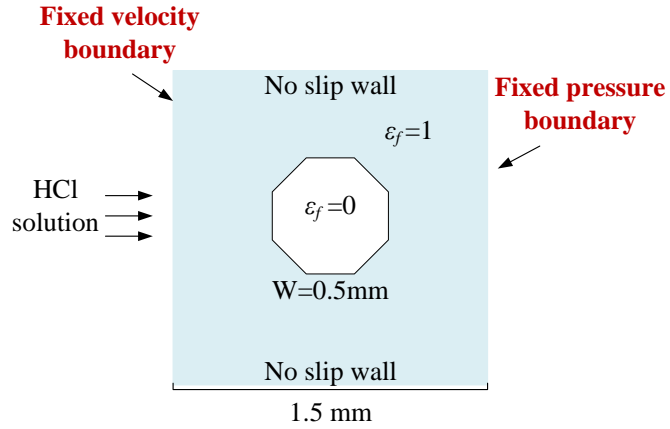


Fig. 3-3 Schematic geometry model and boundary condition of the validation case.

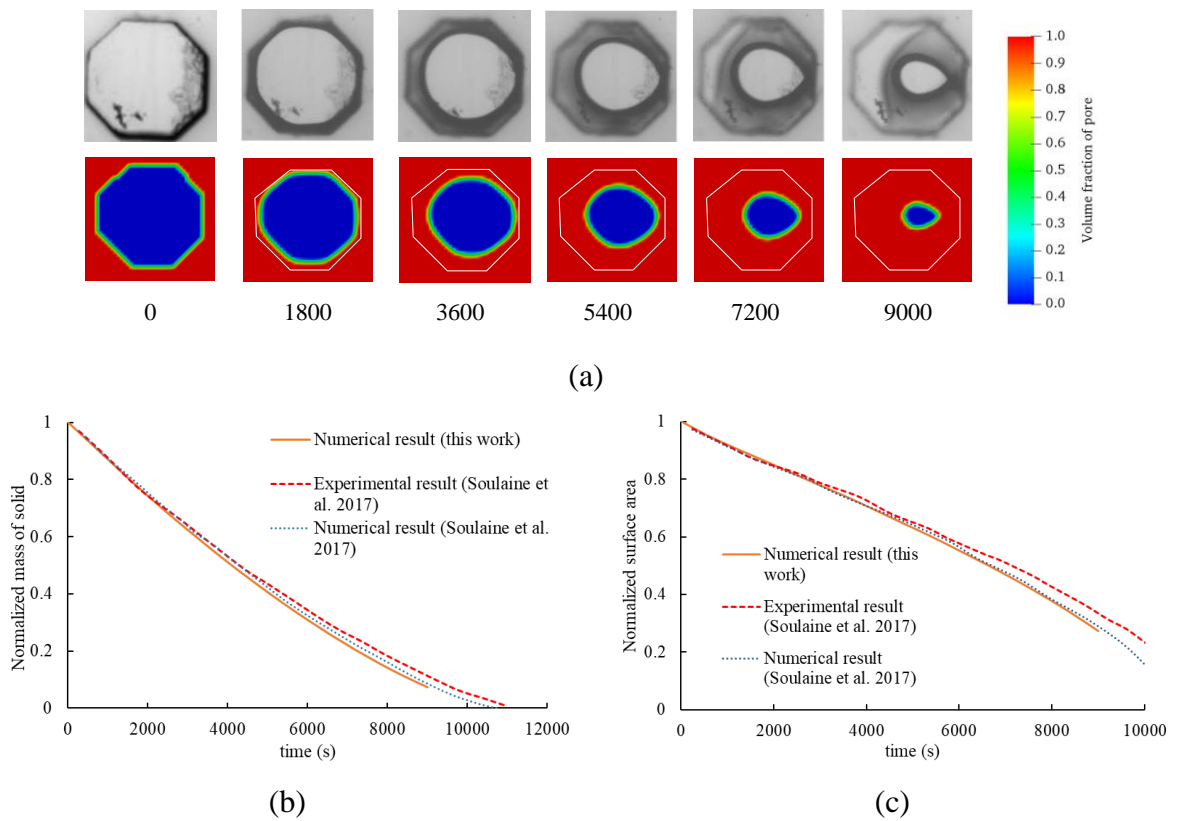


Fig. 3-4 (a) Changing of calcite during the acidizing; the first row was obtained from experimental results (Soulaine et al. 2017), and the second row was obtained from the presented work. (b) Changing normalized solid mass with time. (c) Changing normalized surface area with time.

3.4 Grid size sensitivity analysis

A sensitivity analysis of grid size on the simulation results was conducted, by using the different grid sizes of 0.05 mm, 0.03 mm, 0.019 mm, 0.015 mm, and 0.01 mm (shown in Fig. 3-5). The time step was 0.001 s to guarantee that the courant number was smaller than 1. The contours of the pore volume fractions in different grid sizes are shown in Fig. 3-6.

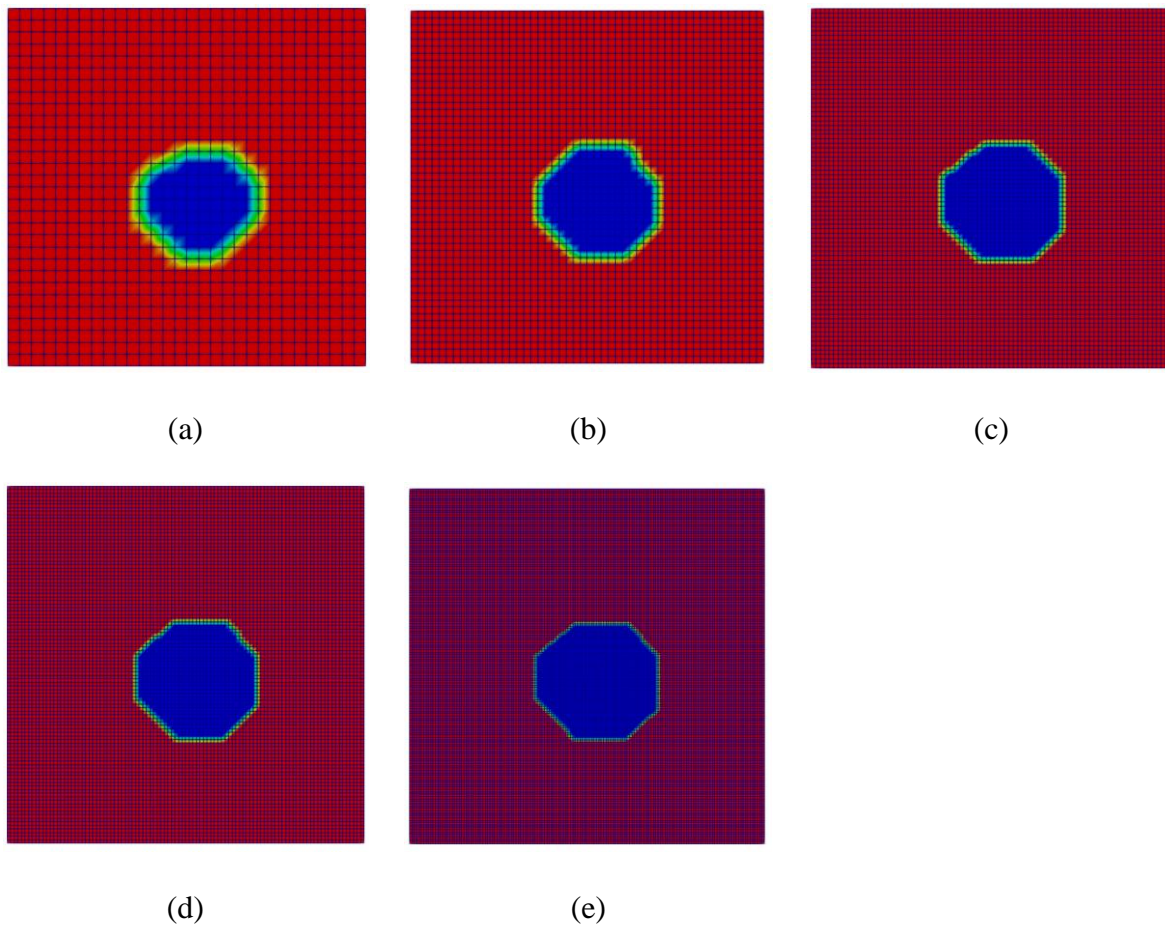


Fig. 3-5 The discretization the computation domain with different grid size.

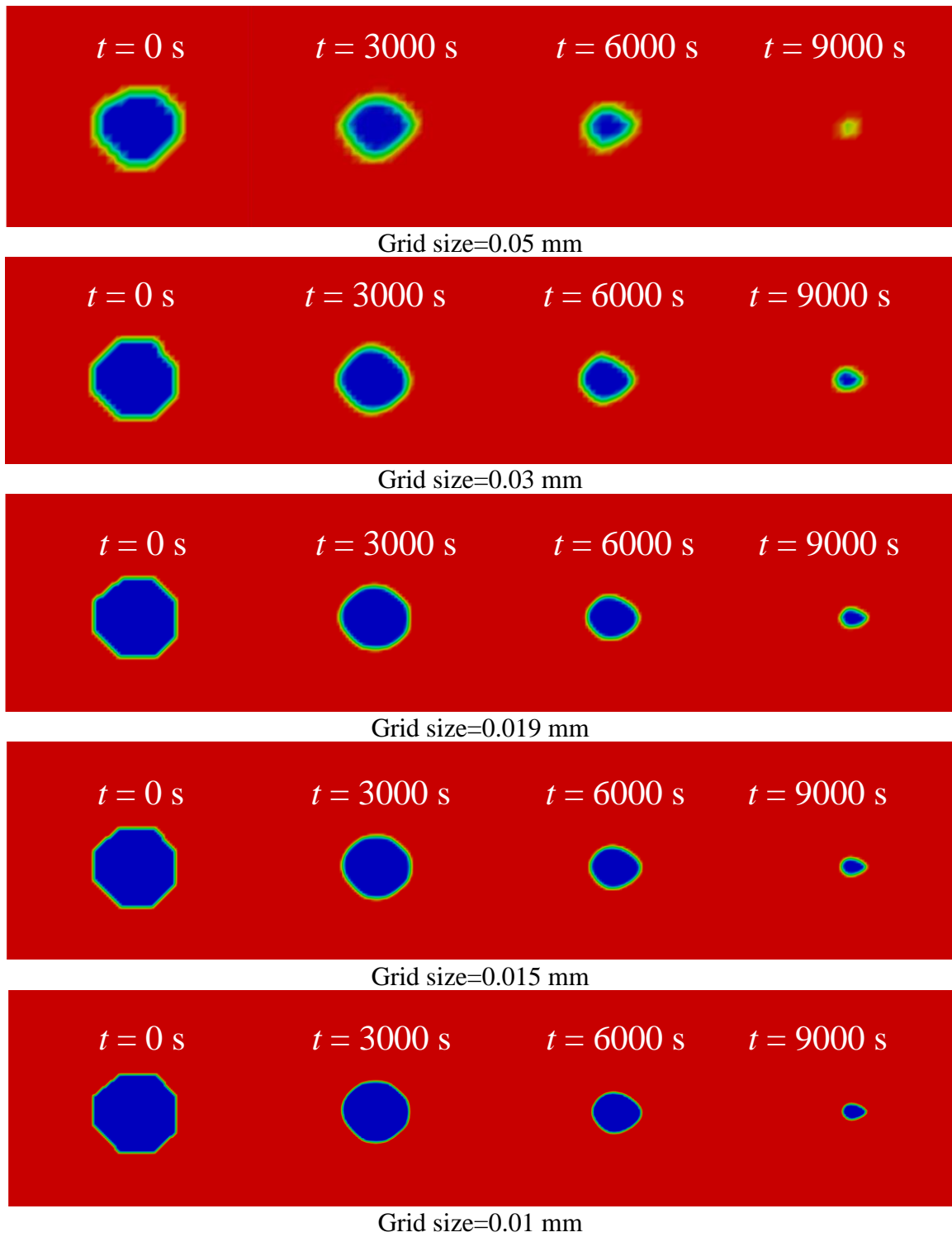


Fig. 3-6 The contours of the pore volume fraction in different grid sizes.

When the grid size was smaller than 0.03 mm, the solid–fluid boundary was sharp and clear. Regarding the computational efficiency, the best range of grid size can be from 0.019 mm to 0.015 mm. The values of the simulation results were quantified in Fig. 3-7. The X axis denotes the grid size, and the Y axis shows the volume fraction of calcite. Different color represents the values at different times as calcite was consumed. When grid size was smaller than 0.03 mm, the error between each case was small, and the result is not sensitive to the grid size.

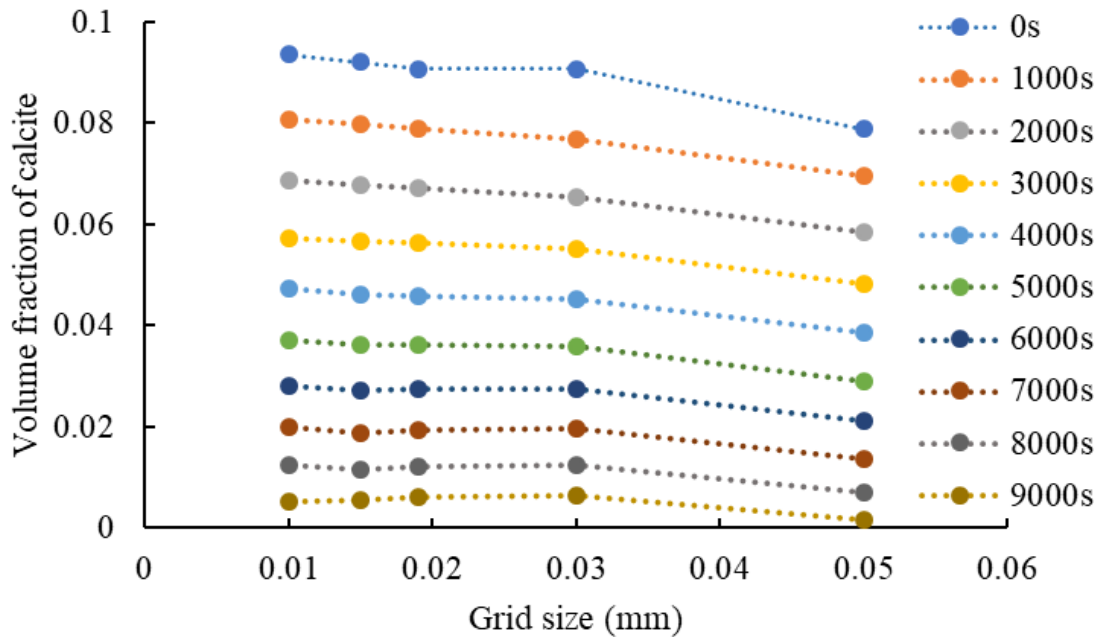


Fig. 3-7 The values of the simulation result (volume fraction of calcite) with different grid sizes.

3.5 Stability analysis

The time step is set as 0.002 s, and the grid size is from 1×10^{-5} to 5×10^{-5} m, where the Courant number is about 0.046-0.23 under the inlet velocity of 1.16×10^{-3} m/s. The Courant

number, calculated by Eq. (3-9), follows the Courant–Friedrichs–Lewy (CFL) condition ($C < 1$) to guarantee the convergence. The tolerances for advection–diffusion equations, mass balance equation and momentum equation were set as 5×10^{-9} . According to Von Neumann stability analysis (Eq.(3-10)), these computational parameters satisfy the numerical stability criteria for the advection diffusion equation. The CFL convergence condition and stability criteria are listed as

$$C = u \frac{\Delta t}{\Delta x} < 1, \quad (3-9)$$

$$\text{and } S_x + S_y = D_i \frac{\Delta t}{(\Delta x)^2} + D_i \frac{\Delta t}{(\Delta y)^2} \leq \frac{1}{2}, \quad (3-10)$$

where, u is the magnitude of velocity; Δt is the time step; D_i is the diffusivity coefficient; Δx is the grid size in x direction, and Δy is the grid size in y direction.

The residuals for calculating velocity in x axis and acid concentration are shown in Fig. 3-8. We set the different input parameters for the simulation to analyze the stability. For the first case, the inlet velocity was 1.16×10^{-3} m/s, and diffusion coefficient was 1×10^{-10} m²/s, which gave the Péclet number value of about 1,400. The second case was set with the inlet velocity of 1.16×10^{-4} m/s, and diffusion coefficient of 1×10^{-7} m²/s. The time step was set as 0.002 s, and other parameter settings were same with the simulation in Section 3.3. The initial residuals for the simulation of fluid flow and reactive transport were smaller than 10^{-4} , which shows good stability of the simulation and efficient convergence.

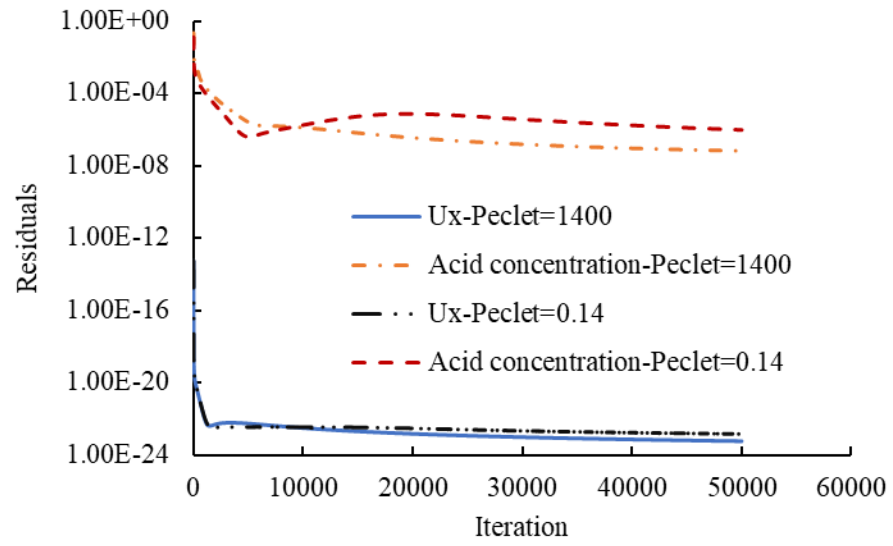


Fig. 3-8 Residuals for the simulation under different input parameters.

4 INVESTIGATION OF ACID DISSOLUTION ON THE DIGITAL ROCK IMAGES

4.1 Introduction

The previous studies covered in the Chapter 1 of Introduction provide a comprehensive insight into the phenomena relevant to reactive transport and calcite dissolution in porous media. They demonstrated that the patterns of acidized wormholes depended not only on Damköhler number (Da) and Péclet number (Pe) but also on the specific structure of porous media and its flow pattern (Kang et al., 2014; Molins et al., 2012). They showed that the variable distributions of fluid velocity in porous media could limit the diffusive transport of injected solvent to the surface of minerals, giving rise to the ineffective calcite dissolution (Molins et al., 2017). As a result, heterogeneous dissolution rate, transport regime, and velocity gradient influenced the pore structure evolution. In the meantime, the evolution of pore structure is significantly affected by the spatial distributions of mineral components. Full-physics pore-scale models can thoroughly describe the fluid flow and the transport pattern of injected solvent depending on the spatial distribution of pores. Raeini et al. also mentioned that sub-pore-scale fluid dynamics insights can be utilized for improving pore-network models (Raeini, Bijeljic, & Blunt, 2014). With the significant advancement of imaging technologies, there have been a substantial improvement in the pore-scale modeling technologies in the last decade. For example, in X-ray CT, the resolution ranges from 100 nm to 1 mm. SEM (Scanning Electron Microscopy) produces images down to the resolutions of 10 nm (Blunt et al., 2013). Pore-scale models can range from millimeter to centimeter, and sizes of published work was summarized in Table 4-1.

Table 4-1 Typical sizes of previous pore-scale modeling.

Author	Research	Size
Huang et al. (H. Huang, Meakin, & Liu, 2005)	Simulated multiphase flow in unsaturated fractures.	3 mm length × 20 mm height
Ferrari and Lunati (Ferrari & Lunati, 2013)	Simulated immiscible displacements in 2D, and studied the relation between macroscopic capillary pressure and pore-scale properties.	88 mm length × 114 mm height and 45 mm length × 58 mm
Raeini et al. (Raeini et al., 2014)	Related the pore-scale forces with Darcy-scale properties.	1.8 mm × 1.18 mm
Liu et al. (H. Liu, Valocchi, Werth, Kang, & Oostrom, 2014)	Simulated flows in 2D geometries of heterogeneous permeabilities.	4.2 mm length × 4.2 mm height
Molins et al. (Molins et al., 2017)	Simulated rock evolution during CO ₂ enriched brine.	10 mm length × 5 mm height

To investigate the effects of the rock heterogeneity on the dissolution rate of minerals, reactant transport rate, and its concentration distribution, we estimated the impact of dimensionless numbers that determine the dominancy between advection, diffusion, and reaction on the morphological changes of rock grains in the digital rock images. Two categorized models with idealized grain geometry and digital rock images were simulated to give a microscopic understanding of reactive transport phenomena. With the idealized grain models, we performed sensitivity analyses regarding the size and distribution of rock grains. We found that the pore structures significantly affected the acid concentrations and transport rates in the system, which resulted in different dissolution rates. For the digital rock cases, we compared the six cases of different Damköhler numbers (Da_{II}) and Péclet numbers (Pe) from

the Niobrara formation (Prodanovic, 2016). The microscopic insights obtained from this study is expected to help improve current Darcy-scale models to accurately simulate the formation of wormholes during acidizing processes, and give guidance on the improved saturation of acid in the porous media with inherent complex structure, by correctly choosing effective operating parameters, successfully predicting large-scale input parameters, and efficiently implementing an acidizing project. This work has been published in (You & Lee, 2021b).

4.2 Simulation of micro-grain porous media model

Previous studies showed that the pore configurations had substantial effects on the concentration gradient and velocity distribution of hydrochloric acid, while significantly decreasing the accuracy of the dissolution rate in upscaled continuum-scale simulation (Kang et al., 2014). In this regard, eight different ideal grain models were simulated to investigate the effects of grain size and structure on the acid transport characteristics and fluid flow, while the acid dissolved the rock minerals. The input parameters are listed in Table 4-2. We took the inlet velocity by considering the published paper about acidizing of pore-scale modelling (Molins et al., 2017; Soulaine et al., 2017). In Soulaine's work, the domain size was 0.024 m-length \times 0.0072 m-height, and the inlet velocity was 10^{-3} m/s with $Re=0.1$ (Soulaine et al., 2017). The inlet velocity is in range of 10^{-3} to 10^{-5} m/s. Grains in case A1, B1, and D1 had a uniform radius and were evenly distributed. Cases A2, A3, and A4 had binary grain radius, where the larger grains were distributed uniformly as a staggered array, and the smaller size grains were inserted with a regular pattern within the void space. Grains were distributed randomly in the cases DD1 and SD1 with binary and single sizes, respectively. The computational domain of the grain model was 0.014 m-length \times 0.0068 m-height. The grid resolution of the simulation was 400

$\times 200$. The discretization the computation domain and the large view of the geometric model was shown in Fig. 4-1, which was fine enough to capture reactive transport in the computational domain. The grain size and porosity are listed in Table 4-3. The initial value of the dimensionless number and permeability was influenced by the structure of the porous media. Took the example of case A3, the volume-averaged absolute permeability for the entire domain at the initial stage was about $2.6 \times 10^{-9} \text{ m}^2$. The Re number was 10^{-2} based on the current setting.

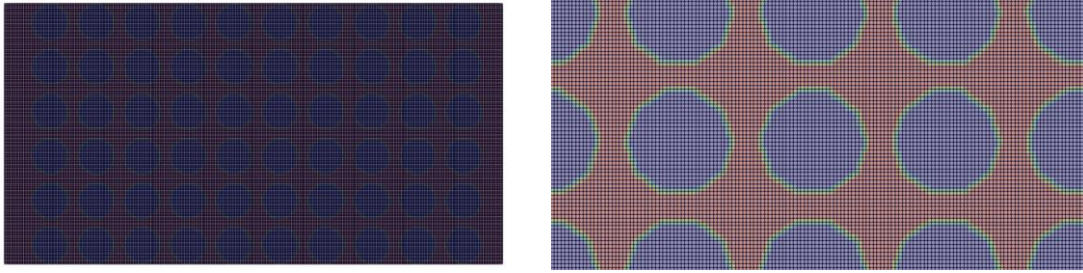


Fig. 4-1 The discretization the computation domain and the large view of the geometric model.

Table 4-2 Input parameters in the simulation case for the validation (Soulaine et al., 2017).

Parameter	Symbol	Value
Fluid density	ρ_l	$920 \text{ kg}\cdot\text{m}^{-3}$
Fluid viscosity	μ_l	$2.4 \times 10^{-3} \text{ Pa}\cdot\text{s}$
Injection velocity	v_{inj}	$1.1 \times 10^{-3} \text{ m}\cdot\text{s}^{-1}$
Reaction constant	k_r	$5 \times 10^{-2} \text{ m}\cdot\text{s}^{-1}$
Molecular diffusivity of acid	D_A	$5 \times 10^{-9} \text{ m}^2\cdot\text{s}^{-1}$
Density of calcite	ρ_s	$2710 \text{ kg}\cdot\text{m}^{-3}$
Inlet acid concentration	$\bar{\omega}_{f,A}$	0.5 wt%

Table 4-3 Size and initial porosity of ideal grain model.

Model	Porosity	Maximum grain size (m)	Minimum grain size (m)
A1	0.72	8×10^{-4}	-
B1	0.54	1×10^{-3}	-
D1	0.44	1.1×10^{-3}	-
A2	0.69	8×10^{-4}	2.5×10^{-4}
A3	0.67	8×10^{-4}	3.5×10^{-4}
A4	0.63	8×10^{-4}	4×10^{-4}
SD1	0.71	8×10^{-4}	-
DD1	0.69	8×10^{-4}	3.5×10^{-4}

The different pore structures gave rise to the different acid distributions and velocity distribution inside the pores, although these cases shared the same geochemical parameters. Fig. 4-2 shows the acid concentration along the outlet boundary and corresponding acid distribution contours at $t = 5$ s. Five microchannels for fluid flow were generated, and they were numbered from bottom to top. For the cases A1, B1, A2, and A3, acid mainly transported through these five channels. However, as can be seen from the concentration curve, the acid concentration was non-uniform within these channels, even under the uniform distribution of grains. For the cases of D1 and A4, acid was mainly transported through channels 1, 3, and 5. It can be explained by the limited flow around the non-slip wall, as observable from the velocity streamline and vector. The existence of grains at the top and bottom blocked the flow, forcing the acid to flow through its nearest channel.

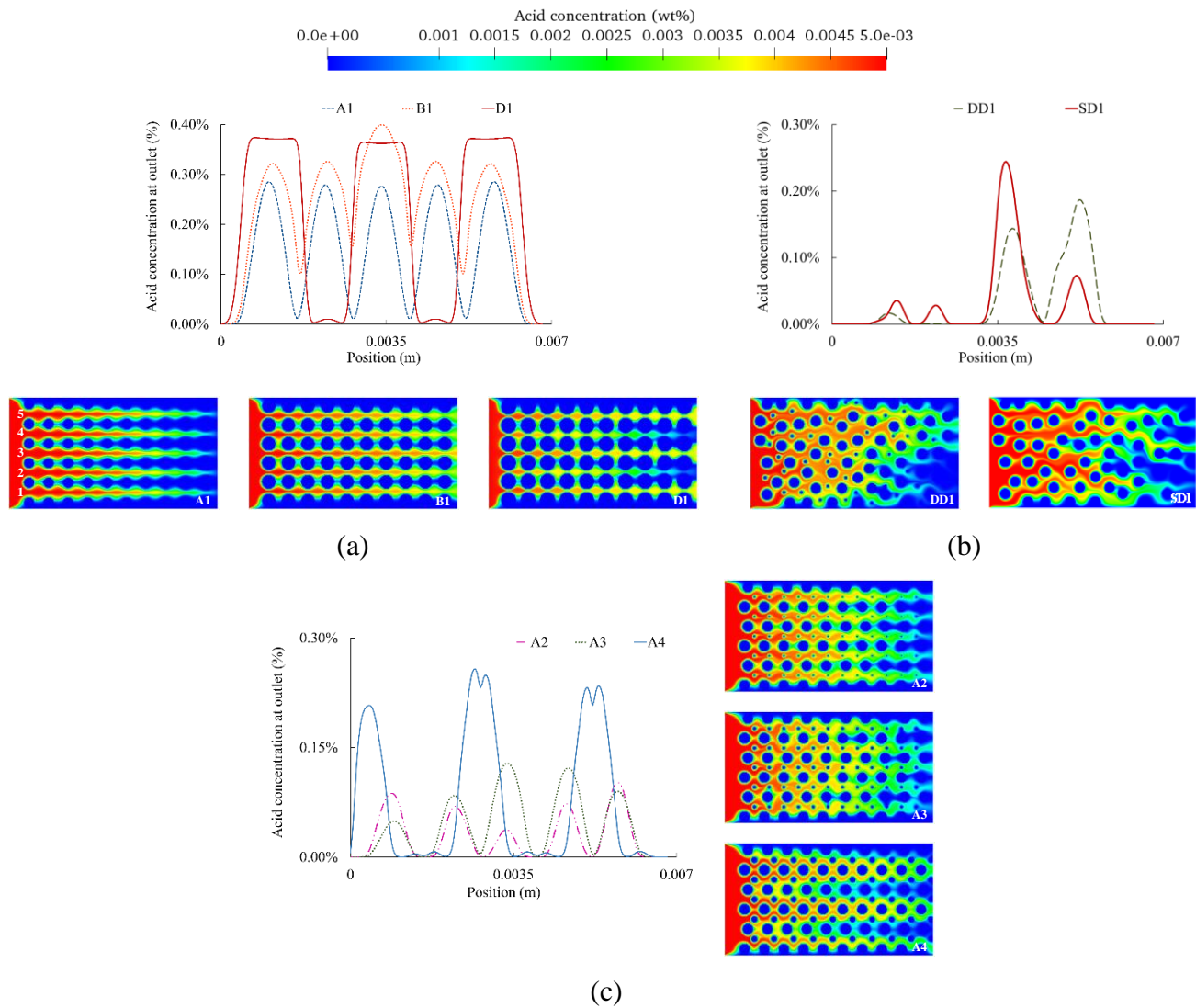


Fig. 4-2 Acid concentration and corresponding contour at $t = 5$ s. (a) Cases A1, B1 and D1; (b) Cases DD1 and SD1; (c) Cases A2, A3 and A4. X axis corresponds to the vertical position along the outlet boundary.

Fig. 4-3 shows the change of normalized effective surface area (A_n) with time in the eight ideal grain models. A_n is the key factor to influence the reaction rate. In general, A_n decreased with time, while acid consumed the minerals. In the binary grain system (A2, A3, and DD1), A_n curve decreased faster at the beginning, then declined slower and showed a linear

proportionality with time after each turning point. The turning points were at 320 s, 620 s, and 600 s in the cases of A2, A3, and DD1 respectively. Small grains speeded up the dissolution rate at the beginning. The larger the variation size ratio (= ratio of the maximum grain size to the minimum grain size in the system) was, the faster the rock was dissolved. This also explains the reason that the case A4 did not have apparent turning point. The turning points also reflected the approximate time when the smaller grains were consumed up. As can be seen from the volume fraction on the right-hand side in the pore space contours, when small grains were almost consumed up, a few larger grains near the inlet were just starting to react. We can observe that the parts of the curves in the cases A2 and A3 were parallel to each other at the later stage, which indicate that the two cases had the same chemical reaction rate, after small grains were exhausted. After all small grains were consumed up, the cases A2 and A3 had the same size grains.

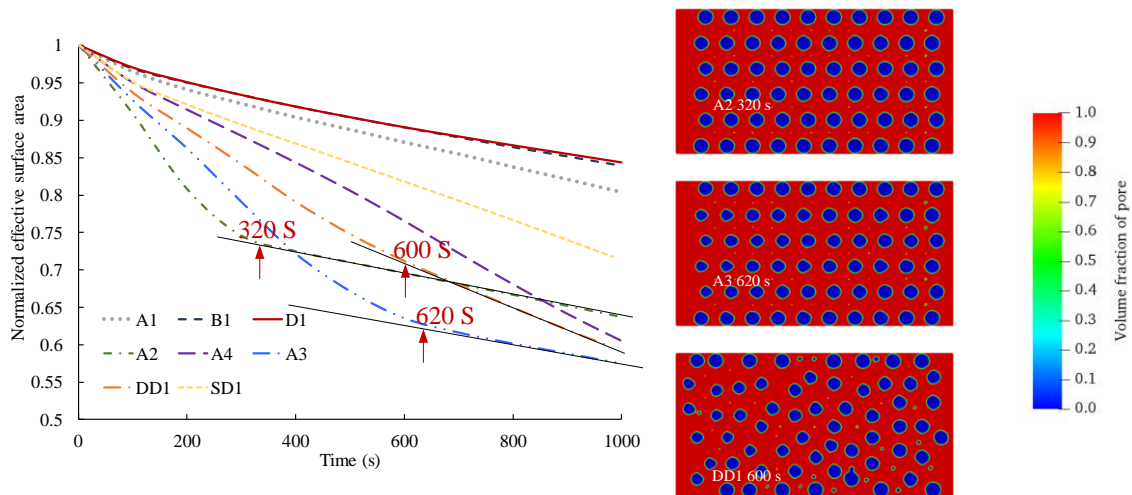


Fig. 4-3 Normalized effective surface area with time and volume fraction of pore space for A2, A3 and DD1 at 320 s, 620 s and 600 s.

Fig. 4-4 indicates the chemical reaction rate with time. Several factors influenced the reaction rates, such as acid concentration, tortuosity, and rock surface area. The reaction rates have increased dynamically from 0 kg/m³s to the peaks with acid flowing into the systems, and the models with larger grains could reach to higher peaks. The small grains in the model could speed up the chemical reaction at first, but the reaction rate dramatically decreased and reached a constant value after the consumption of small grains, especially when the variation size ratio was large. In the cases A2 and A3, the stable reaction rate was very close to that in the single model of A1 after $t = 700$ s, because the A2 and A3 models had the same maximum size and even distribution of grains. However, this trend was only observable when the variation size ratio was large enough. The cases that had the single size and evenly distributed grains have larger average reaction rate as the grain size increased. For the cases with the random distribution of grains, grain size was not the key factor influencing the reaction rate. The cases A3 and DD1 had the same grain sizes but displayed different tendencies of reaction rates. This was because, the concentration gradient was more complex in case DD1, and thereby the partial breakthrough in the random distribution model occurred.

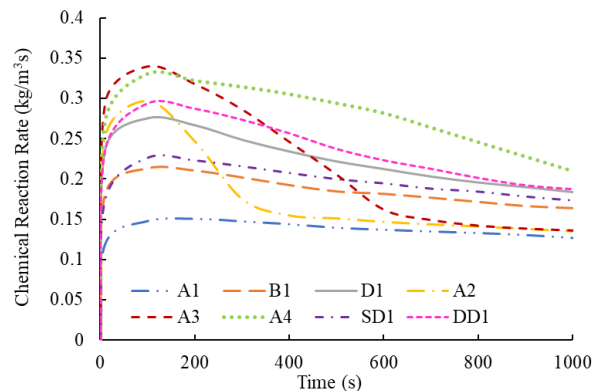


Fig. 4-4 Chemical reaction rate of different grain models with time.

As can be seen in this section, the ideal grain models could provide the insight on the characteristics of calcite dissolution rate and acid concentration in porous media. The pore-scale grain size, tortuosity, and distribution influenced the reaction rate, flow pattern, and solid-liquid interface evolution, even though they had the similar value of porosity. During the acidizing, the homogeneous distribution of grains has a relatively stable dissolution rate. In contrast, when the variation size ratio was large, the dissolution rate has significantly changed from a high rate to a low rate, about 2.3 times of change for the largest variation size ratio case. Under the same variation size ratio, the heterogeneity of distribution led to different dissolution trends.

4.3 Simulation of digital rock under different dimensionless numbers

To illustrate the characteristics of the acidizing process and clarify the dissolution and transport pattern in real porous media in a pore-scale perspective, an x-ray microtomography (CT)-scanned digital rock image from Niobrara formation (Fig. 4-5) was simulated (Prodanovic, 2016). The dynamic change of grain's shape, calcite dissolution rate, rock surface area, and flow velocity distribution under different dimensionless numbers have been analyzed as well. The digital rock image was obtained from a tight volume around the segmented fracture space. In this digital rock image, there are two clusters of grains displayed at the bottom left and top right, and a large number of smaller grains are connected to these two grain clusters, forming an irregular diagonal path in the center. The original image has the size of $730 \times 600 \times 170$ voxels, and resolution of $29.69 \times 29.69 \times 29.69 \mu\text{m}$, respectively. The schematic of this digital rock was 0.0178 m-length and 0.0193 m-height. The grid resolution was 250×300 and the discretization of the computational domain is shown in Fig. 4-5. The inlet velocity of acid

solution was set as 0.0011 m/s. Six cases of different Damköhler number (Da_{II}) and Péclet (Pe) number were designed and simulated. Da_{II} numbers were set in the range of 2.88×10^{-2} - 2.88×10^5 , while Pe numbers were set in the range of 0.0836-836 with different diffusivity coefficients (5×10^{-7} m²/s - 5×10^{-11} m²/s) and reaction rate constants (1×10^{-5} m/s- 1×10^1 m/s). The initial absolute permeability for the whole computational domain was 1.8×10^{-8} m². The Re number was about 10^{-1} . We considered a broad range of Da_{II} and Pe to cover most of the situation. The previous studied categorized the wormhole patterns during the acidizing regarding the different Da_{II} numbers and Pe numbers (Starchenko & Ladd, 2018). The Da_{II} numbers ranged into 10^{-3} - 10^2 , and Pe ranged into 10^0 to 10^3 . The acid dissolution usually is in the magnitude of 10^{-9} m²/s, and is influenced by the temperature and other additives (Leaist, 1984). Detailed numbers are listed in Table 4-4. Other parameters were same with the simulation cases in Section 3.3.

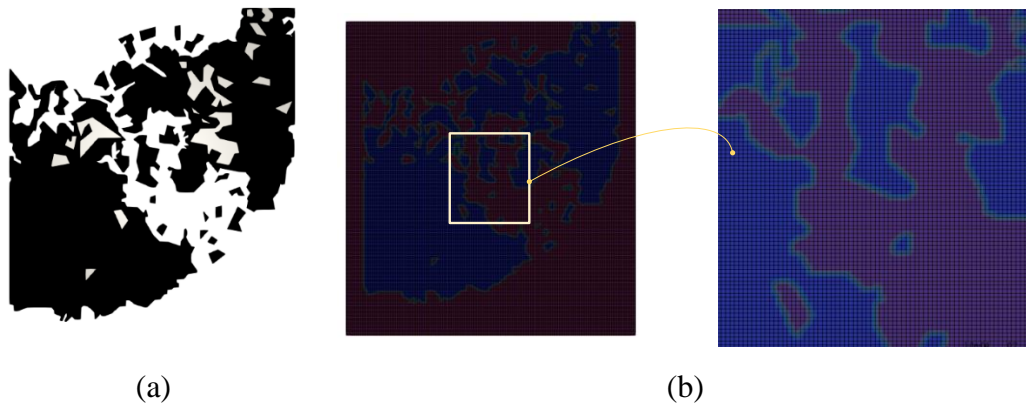


Fig. 4-5 (a) Digital rock of Niobrara formation, CO, USA (Prodanovic 2016); (b) The discretization of the computational domain.

Table 4-4 Parameters for the simulations of the cases for Niobrara formation digital image.

Case	Da_{II}	Pe
1	2.88×10^{-1}	0.836
2	2.88×10^3	8.36
3	2.88×10^5	0.836
4	2.88×10^{-2}	0.0836
5	2.88×10^4	836
6	2.88×10^{-1}	0.0836

Acid concentrations after 50 s of chemical reaction is presented in Fig. 4-6. It shows a gradual concentration transition from the pore area to the rock boundary layer when $Pe < 1$. Da_{II} would determine how far acid could penetrate to tiny space. When $Pe < 1$, the diffusion dominated the acid transport, and advection was relatively weak. Thus, acid was easily penetrating to tiny crevice and corner. This trend was in accordance with the previous work, where the low Pe numbers caused the solute to be transported to a deeper distance from the inlet (Dashtian, Bakhshian, Hajirezaie, Nicot, & Hosseini, 2019). When $Pe > 1$, advection dominated the system, and acid concentration gradient was small. Under small Da_{II} and Pe ($Da_{II}, Pe < 1$), such as the cases 1, 4, and 6, acid saturated the pore space, as penetrating deeply inside the tiny corner and crevice. However, acid concentration was very low in complex configuration with poorly connected pores. When Da_{II} was larger than 1, and Pe was smaller than 1, the gradient of acid concentration was large (case 3), and acid only flowed into the area with wide path and well-connected pores. When Da_{II} and Pe were larger than 1 at the same time (cases 2 and 5), acid could penetrate well to the tiny pores. Acid concentration distribution was relatively uniform within the central pathway, and the acid concentration gradient was small in the case 5. While acid was reacting with the rock surface, the concentration distribution

in the system dynamically changed. At $t_2 = 1,500$ s, acid in the cases 2 and 3 had deeper penetration than that at $t_1 = 50$ s. The central grains, which were highlighted in Fig. 4-7, have been consumed up under high Da_{II} . It indicates the chemical reaction dominancy, as acid could flow easily through these areas while accelerating the dissolution rate. In the cases 1, 4, and 6 of Fig. 4-7, where Da_{II} and Pe were smaller than 1, the majority of streamlines was distributed near the rock surface and had velocity around 0. A large amount of acid solution bypassed through the bottom channel by the advection effects, and little amount of acid could diffuse to the area with complex structure and high tortuosity. To penetrate to the complex structure at the center, fluid needed to pass a very thin throat highlighted with red circle in the case 1 in Fig. 4-7. Under large Da_{II} , acid dissolved the rock and enlarged the thin throat, allowing more fluid to pass through the throat. Subsequently, the local calcite dissolution rate at the downstream area was speeded up.

Fig. 4-8 (a) shows the change of volume fraction of pore space with time. We could categorize the curve into three patterns—linear growth (cases 1, 4, and 5), pseudo-linear growth (cases 2, and 3), and a flat S-curve growth (case 6). In the linear growth, the ratio of Da_{II} to Pe was smaller than 50, and the volume fraction of pore kept a stable growth speed. Cases 1 and 4 had a minimal dissolution rate of minerals, and their Da_{II}/Pe ratio was 0.034.

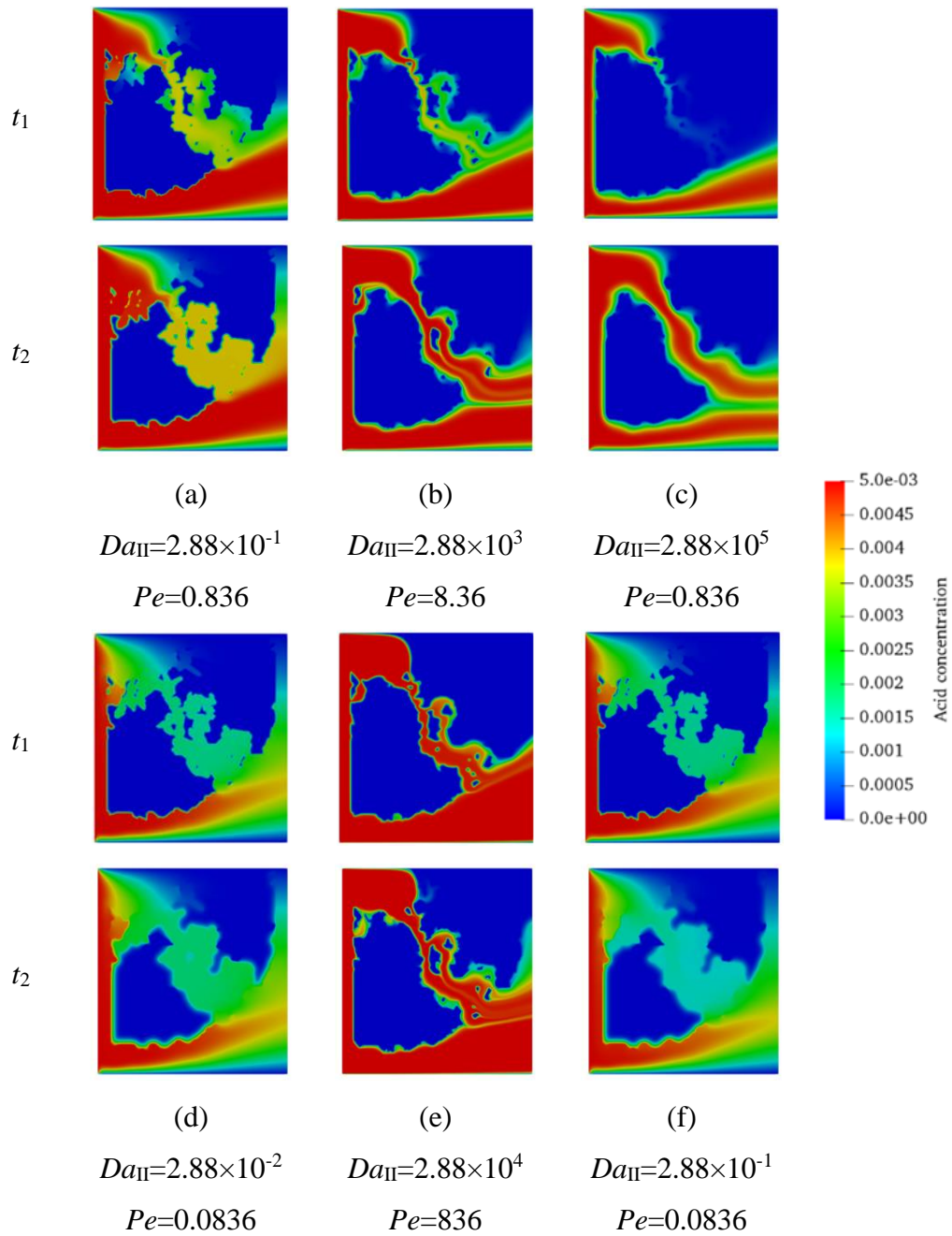


Fig. 4-6 Acid concentration contours for different Damköhler numbers and Péclet numbers at $t_1 = 50$ s and $t_2 = 1,500$ s. (a), (b), (c), (d), (e), and (f) correspond to the case 1, 2, 3, 4, 5, and 6, respectively.

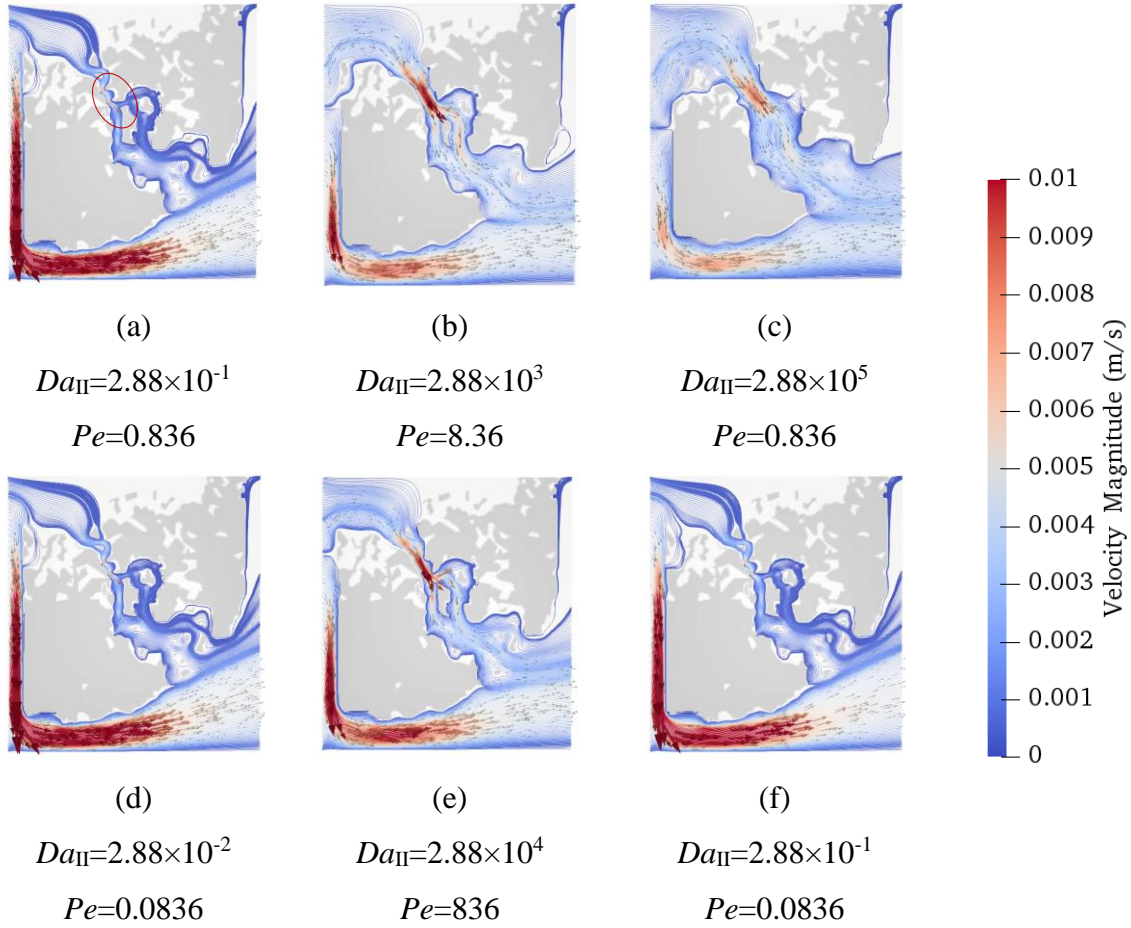


Fig. 4-7 Streamline and velocity vector of fluid flow at $t = 1,500$ s. Arrow denotes the direction of flow; size and color denote the magnitude of the velocity. (a), (b), (c), (d), (e), and (f) correspond to the case 1, 2, 3, 4, 5, and 6, respectively.

The pore volume fraction is shown in Fig. 4-9, where Case 1 and 4 kept the same volume fraction of pore value. We found that when the Da_{II} and Pe were very close, and Da_{II}/Pe ratio was smaller than 1, the pore only showed a slight change even when the value of Da_{II} was larger. Under the low Da_{II}/Pe ratio, the acid firstly consumed the lower left corner area and the scattered grains distributed in the central area, where a large amount of acid transport passed through. In the pseudo-linear growth, the growth speed decreased gradually until it reached a stable velocity. Acid could easily penetrate to deep area with complex structure, where the grain was consumed uniformly, and the grain surface

became smoothed after the reaction. Case 6 is exceptional, because it had lower growth velocity of pore spaces at the beginning, and then it speeded up after $t = 2,000$ s. Under this condition, acid easily saturated the upper-left corner, and the grain surface had sharp edges. Compared with the cases 1 and 4, the case 6 had larger Da_{II} and smaller Pe , which denoted stronger chemical reaction and diffusion. In the case 6, acid tended to penetrate to the small corner and complex structure, dissolving more small grains. Therefore, a wider channel was formed and gave rise to the faster dissolution rate afterwards. This was also shown in Fig. 4-8 (b); in the case 6, normalized effective surface area decreased with an approximately constant speed while the rock grains were dissolved.

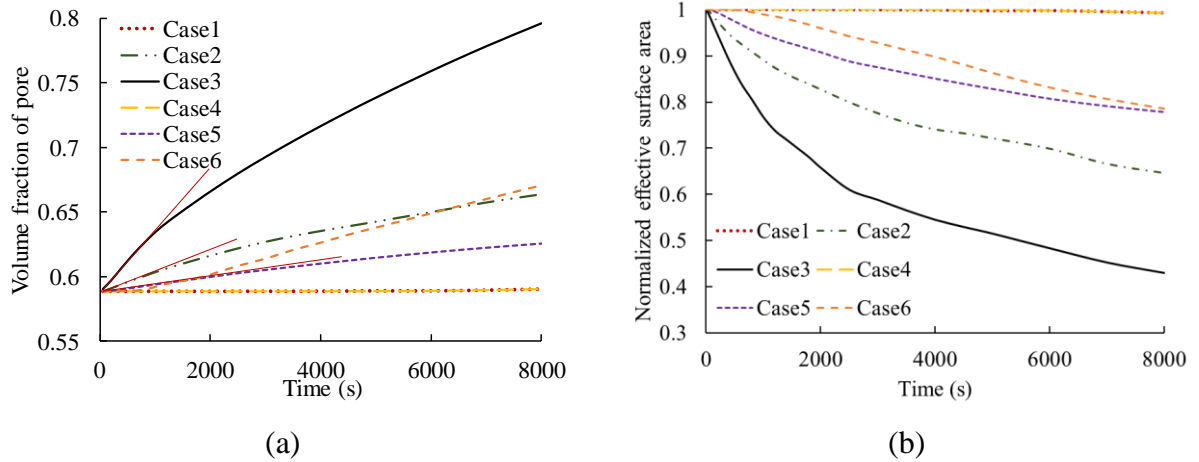


Fig. 4-8 (a) Volume fraction of pore with time. (b) Normalized effective surface area with time.

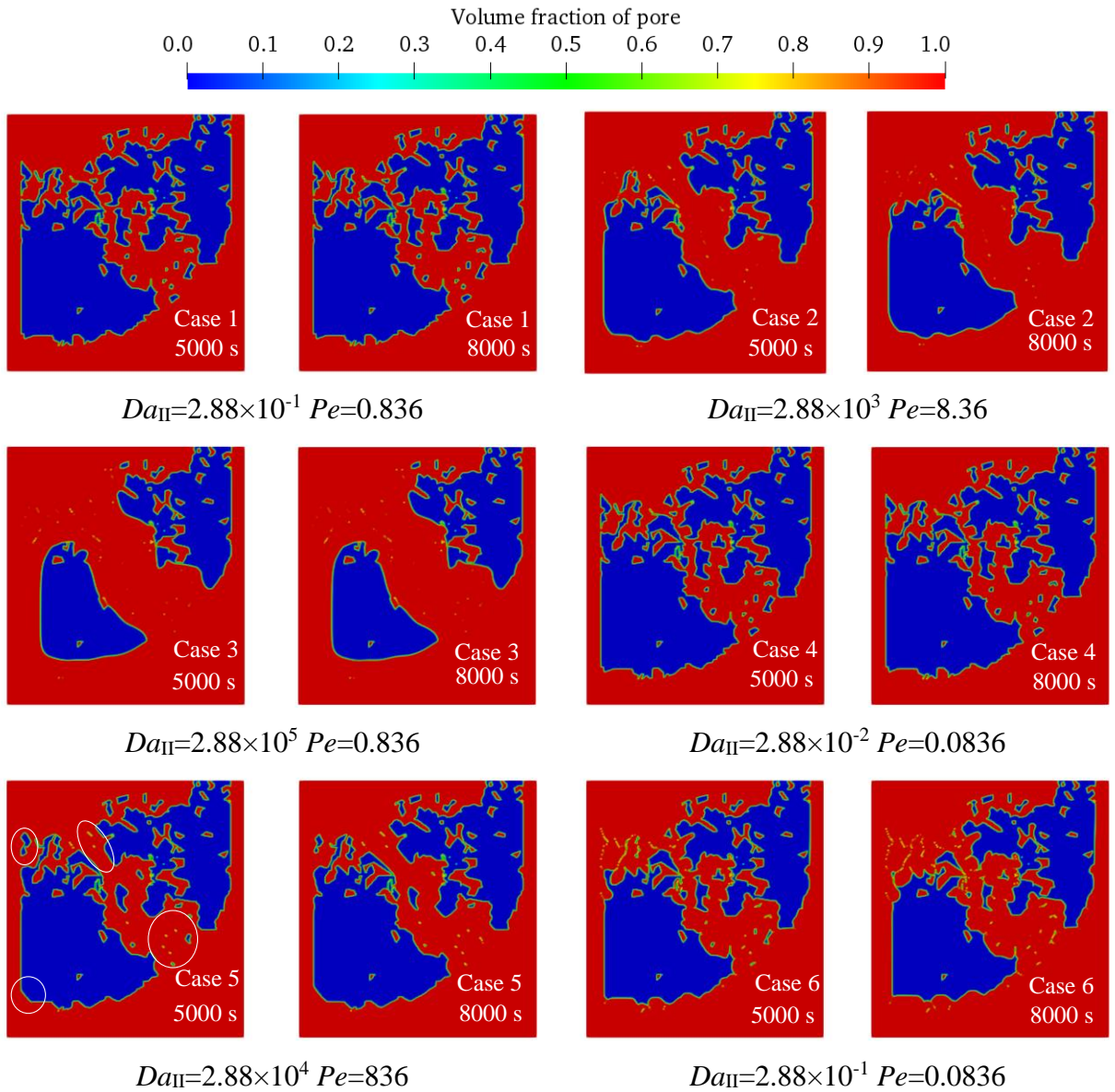


Fig. 4-9 Volume fractions of pore at $t_1=5,000$ s and $t_2=8,000$ s.

5 INVESTIGATION OF SURFACE ROUGHNESS ON THE ACID DISSOLUTION OF NATURAL FRACTURES

5.1 Introduction

Natural fractures are the essential pathways by which water, hydraulic fracturing fluids, oil and gas, reactants, and contaminants can travel in the porous media. The geological structure of the fractures in the porous media governs the fluid flow, solvent transport, and chemical reaction. In the acidizing project, these subsurface phenomena depend on the dynamic evolution of geological structure induced by the calcite dissolution. The pore-scale parameters such as flow characteristics, reactants concentration, fluid–solid interfacial area, and chemical reaction kinetics are essential to the numerical simulation in the continuum model. Most continuum models use porosity–permeability relationship, Darcy’s Law, effective diffusion coefficient, and effective surface area to characterize the flow and reactive transport. However, Darcy’s law is not valid enough to describe the fluid flow in fracture because the heterogeneous flow pattern and transport behavior result in the overestimation of the reaction rate, especially in porous media with high roughness fracture (Deng et al. 2018). Therefore, a better understanding and accurate description of the dynamically changing parameters can help correct the relevant relationships, effective surface area, and mass transfer coefficient in the porous media with fractures.

To investigate the impact of fracture surface roughness on fluid flow, reactive transport, dissolution mechanisms, and fracture structure evolution during the acidizing process, we first studied the dissolution and transport pattern in the parallel plates in terms of the second Damköhler number and Péclet number. Then, we generated twenty–nine single and multiple sine wave profiles to describe the various surface roughness of the fractures. Finally, an Indiana

limestone sample with different calcite and quartz contents was employed to elucidate the impact of stable minerals in the dissolution process. We analyzed the dissolution rate, volume fraction of pores, effective surface area, and normalized porosity–permeability relationship, and the investigation reveals several interesting findings. We categorized the solid dissolution of fractures into three dissolution patterns regarding the second Damköhler number and the Péclet number. We implemented the pore–scale modeling and found these informative experimental parameters of dissolution rate, effective surface area, and porosity–permeability relationship in the fractured porous media. This information can be directly used as the input parameters for the Darcy–scale models describing the acidization in porous media containing fractures with various characteristics to decrease error between the actual conditions and the simulated conditions. This work has been published in (You & Lee, 2021c).

5.2 Fracture roughness generation and volume–averaged parameters

The roughness surface of the fracture was profiled by sine waves, where the fracture was mirror symmetry. We selected a 2–D cross–section of the fracture. The cross–section size was 0.02 m in length, and the average aperture was 0.001 m. The size mimics the rough fracture from the Niobrara tight Formation (Tokan-Lawal, Prodanović, Landry, & Eichhubl, 2017). We have two types of the sine waves—the single sine wave and the multiple sine waves—, which have been proved to be effective in representing the fracture roughness profile regarding the fluid flow and transport (Deng et al., 2018). These equations respectively generated the single sine wave profile and the multiple sine wave profiles

$$y = a \cdot \sin\left(\frac{2\pi}{WL}(x - x_0)\right) \quad (5-1)$$

$$\text{and } y = \sum_i a_i \cdot \sin\left(\frac{2\pi}{WL_i} \cdot R_{i-1}(x - x_{i,0})\right), \quad (5-2)$$

where, k is the wave number; a is amplitude; WL is wavelength; x_0 is the sine wave phase, which is half of the wavelength; R_{i-1} is the random number. We overlaid three sine waves with different wavelengths and amplitudes to generate irregular surface roughness. Nineteen single wave profiles and ten multiple wave profiles were considered in this study.

In order to quantify the roughness, we use the roughness factor to calculate the arithmetic mean deviation of the mean line

$$Ra = \frac{L_{surface}}{L_f} = \frac{1}{L_f} \int_0^{L_f} \sqrt{1 + (y(x)')^2} dx, \quad (5-3)$$

where, $y(x)$ denotes the fracture roughness function; $L_{surface}$ is the length of the roughness surface. As Ra grows larger, the surface becomes coarser. Oppositely, the small Ra denotes the smooth surface.

5.3 Dissolution and transport in smoothed fracture

Before estimating the effects of surface roughness on the dissolution and transport, we first investigated the dissolution and transport pattern in the smoothed fracture in terms of the second Damköhler number and Péclet number, as listed in Table 5-1. The inlet velocity was set in the range of 10^{-2} to 10^{-6} . For the smooth surface fracture, the initial absolute permeability for the whole computational domain was $2.6 \times 10^{-8} \text{ m}^2$. The Re number was from 10^0 to 10^4 . The domain size is about $0.02 \text{ m} \times 0.003 \text{ m}$ and the grid resolution is 400×100 . The discretization of the computational domain is shown in Fig. 5-1.

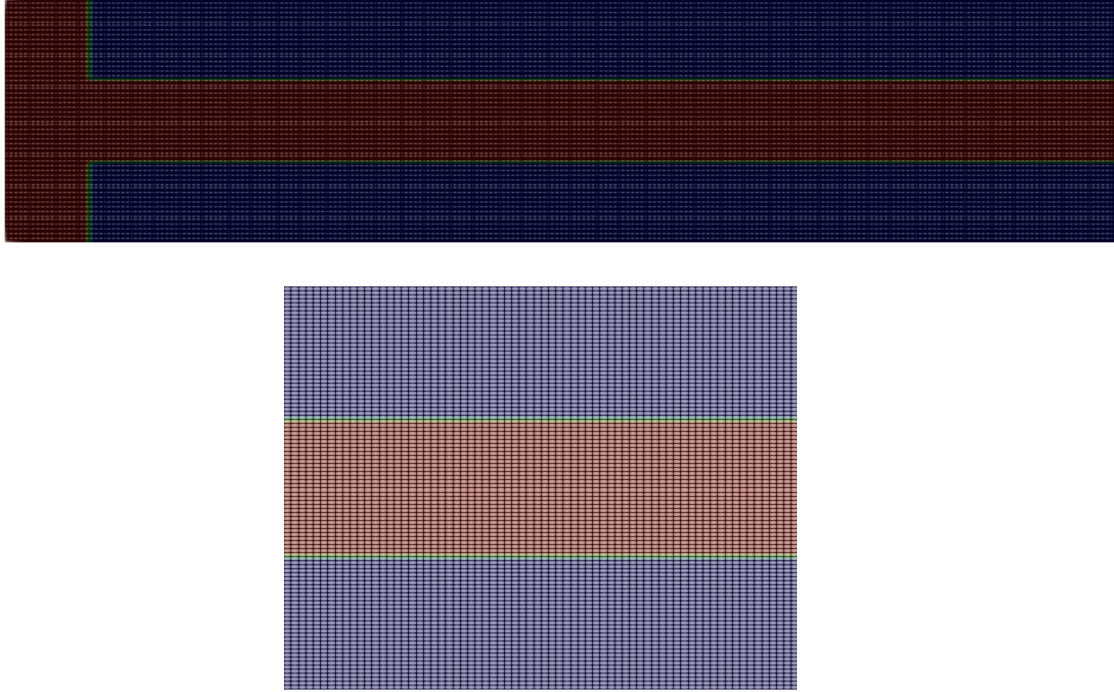


Fig. 5-1 The discretization of the computational domain (above) and the expanded view (below).

Table 5-1 Parameters for the smoothed surface fracture simulation.

	Damköhler number (Da_{II})	Péclet number (Pe)	Dissolution pattern
C1	2.22×10^7	3.23×10^4	Edge dissolution
C2	2.22×10^5	3.23×10^2	Edge dissolution
C3	2.22×10^3	3.23×10^0	Face dissolution
C4	2.22×10^1	3.23×10^{-2}	Front dissolution
C5	2.22×10^{-1}	3.23×10^{-4}	Front dissolution
C6	2.22×10^3	3.23×10^1	Face dissolution
C7	2.22×10^4	3.23×10^1	Face dissolution
C8	2.22×10^3	3.23×10^{-1}	Front dissolution
C9	2.22×10^3	3.23×10^{-2}	Front dissolution
C10	2.22×10^1	3.23×10^1	Edge dissolution

We categorized the solid dissolution of fractures into three dissolution patterns regarding the second Damköhler number (Da_{II}) and the Péclet number (Pe)—face dissolution, front dissolution, and edge dissolution (Fig. 5-2). These patterns are summarized by the values of dimensionless numbers in Fig. 5-4. When $Pe > 1$ and $Da_{II} > 10^2$, the acid has a relatively uniform distribution within the fracture among three regimes. Thus, the acid consumed the fracture's top and bottom surface, known as the face dissolution. As shown in Fig. 5-3, the acid thoroughly saturated the fractures, but the acid concentration gradient varied with the different Da_{II} and Pe . With $Pe > 1$ (C3 and C6), the advection effect was dominant in the system; the acid concentration was low in the deep area of the fracture, leading to the asymmetric dissolution from upstream region to downstream region. However, under the same Péclet number, when the chemical reaction effect became stronger, the upstream region and downstream region had a similar dissolution rate (C7). When $Pe < 1$, the diffusion effect was significant, the acid slowly saturated the fracture from the inlet, and the dissolution pattern was the front dissolution. The edge dissolution occurred when $Pe > 10^2$, or $1 < Pe < 10^2$ and $Da_{II} < 10^2$ at the same time. When $Pe > 10^2$, the advection effects were very strong. Although the acid concentration was uniform with the fracture under this condition, the advection effect was too strong to dissolve the rock inside the fracture. When $1 < Pe < 10^2$ and $Da_{II} < 10^2$, the ratios of Da_{II} and Pe were smaller than 1, and the reaction effect was weaker than the advection effect. Thus, the dissolution started from the edges of the fracture at the inlet and outlet.

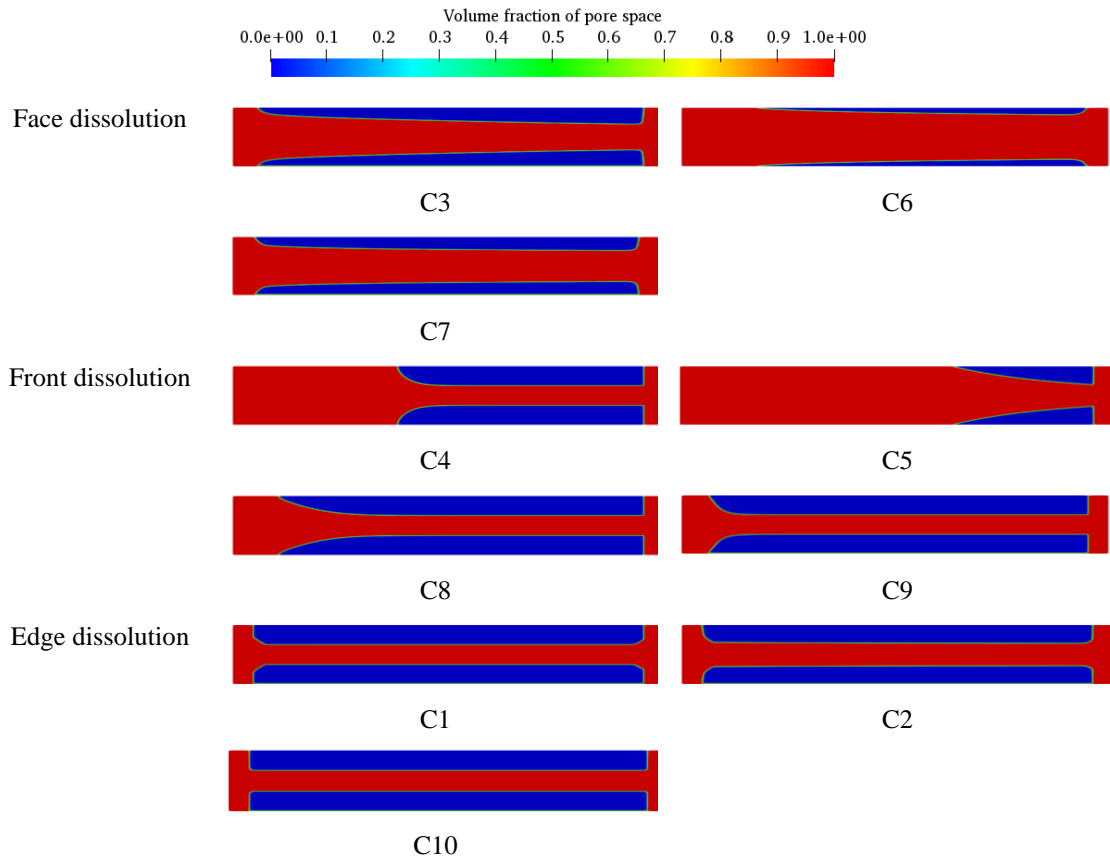


Fig. 5-2 The different dissolution patterns under different dimensionless numbers, where the results of C3, C4 and C6 were observed at $t = 1,000$ s, C10 at $t = 100,000$ s, and the others at $t = 3,000$ s.

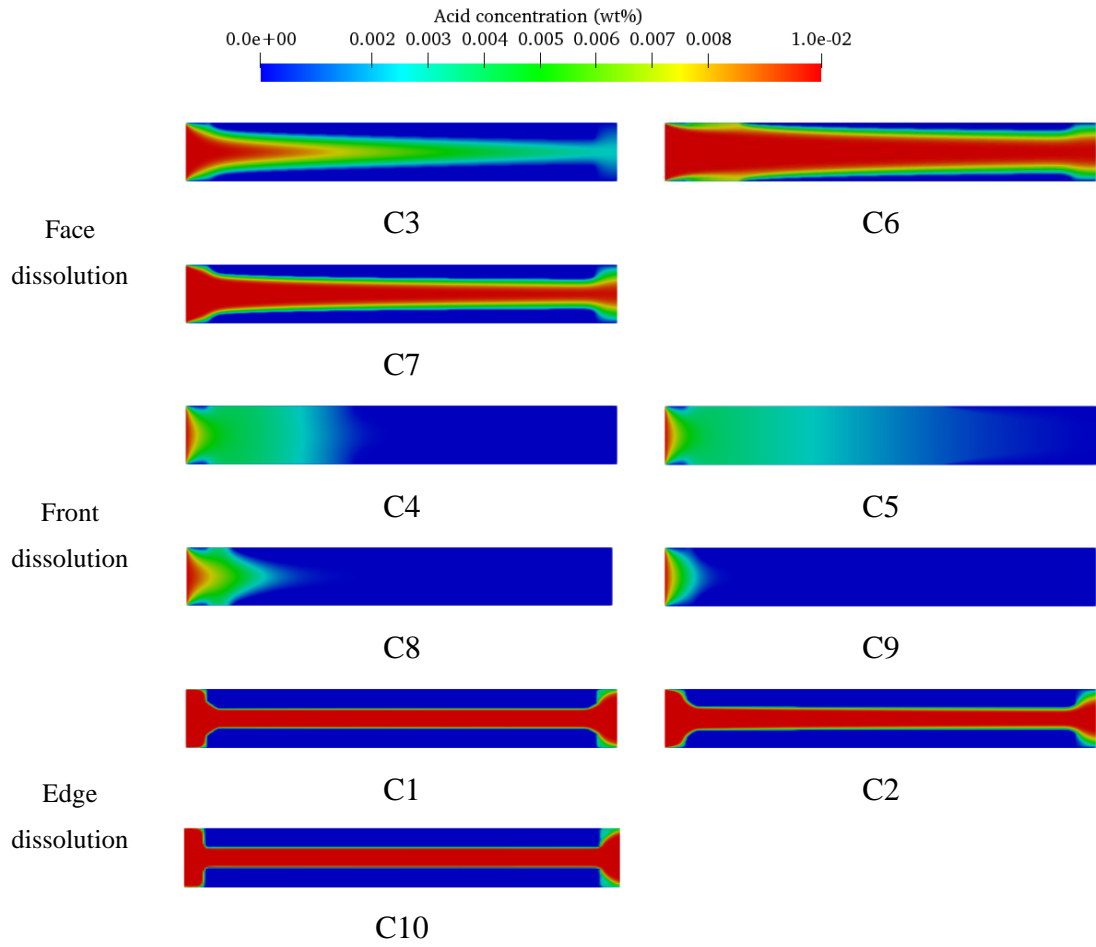


Fig. 5-3 The acid concentration distribution under different dimensionless numbers, where C3, C4 and C6 were observed at $t = 1,000$ s, C10 at $t = 100,000$ s, and the others at $t = 3,000$ s.

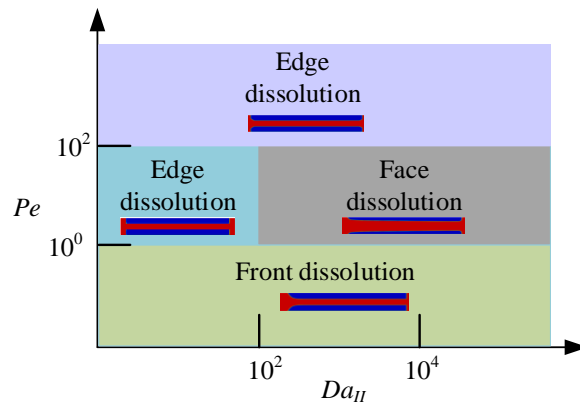


Fig. 5-4 Calcite dissolution patterns.

Fig. 5-5 (a) shows the averaged volume fraction of pore space, which indicates that the front dissolution pattern and the face dissolution pattern have a shorter time to consume the rock in the fractured system. The three dissolution patterns can be reflected by the different types of effective surface area curves (Fig. 5-5 (b)). For the edge dissolution (blue curve), the effective surface area decreased linearly and slowly. In the front dissolution (red curve), the effective surface area decreased fast at the beginning and then decreased with a relatively slow speed, distributing an “L” shape curve. The face dissolution (green curve) has an “S” shape decrease curve, where the effective surface area firstly decreased, then kept a constant value for a while, and finally decreased again. Fig. 5-5 (c) shows the changing dissolution rate with time, where the edge dissolution has the smallest value among the three dissolution patterns. The dissolution rate of edge dissolution fluctuated around a constant value. One possible reason is that the advection dominated the system and caused the unstable acid concentration near the fracture surface. We found that the dissolution rate was low when Pe or Da_{II} were very large ($Da_{II} > 10^4$, $Pe > 10^2$), as can be seen in C1 and C2. For efficient acidizing, the ratio of Da_{II} and Pe should be very big or very small, or the dissolution rate will be significantly low (C8, C9, and C10). The best range of Da_{II}/Pe for efficient acidizing is $10^1 \sim 10^2$.

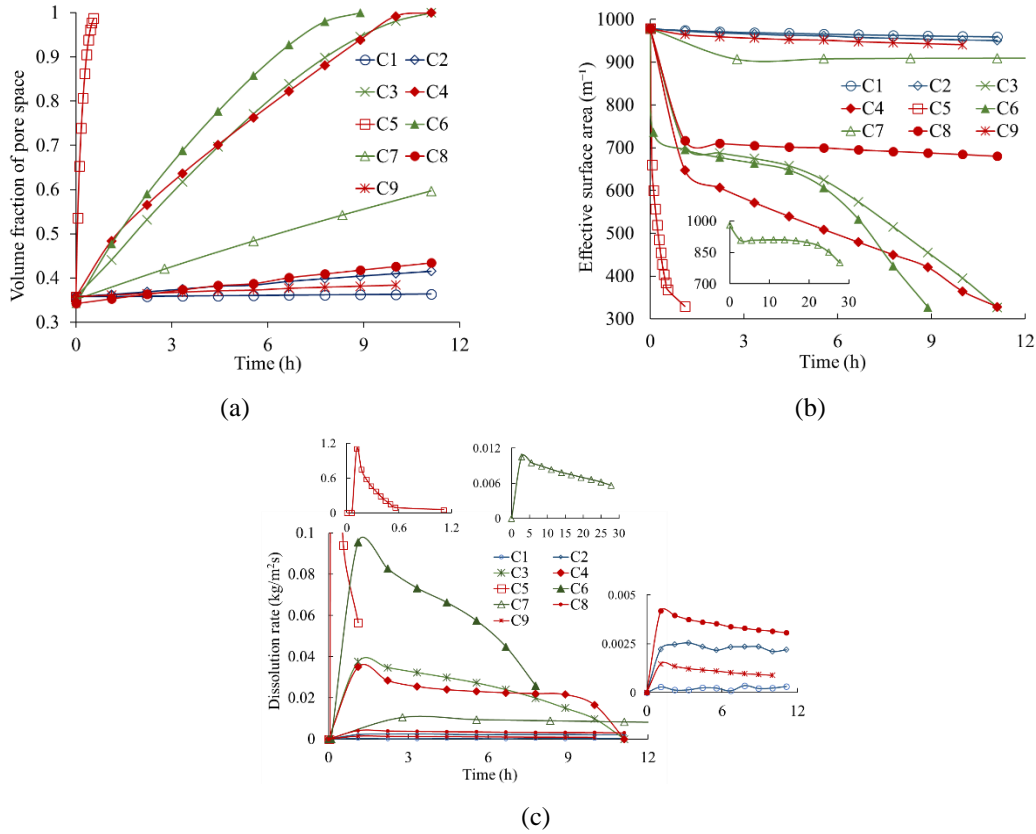


Fig. 5-5 (a) Volume fraction of pore space with time; (b) Effective surface area with time; (c) Dissolution rate with time.

5.4 Dissolution and transport in fracture with rough surface

In this section, we generated twenty-nine single- and multi-wave profiles to mimic the rough surface of the nature fracture, as shown in Table 5-2 and Table 5-3. The black color indicates the solid zone, and the white color indicates the fracture. The domain size is about $0.02 \text{ m} \times 0.003 \text{ m}$, and the grid resolution is 400×100 , which is shown in Fig. 5-6. The input parameters are listed in Table 5-4. The absolute permeability of the whole computational domain at the initial stage is about $2.6 \times 10^{-8} \text{ m}^2$. The Re number is about 10^{-2} . Under the following simulation parameters, the dissolution regime was in the face dissolution pattern. The solution of 1 %-hydrochloric acid was injected from left hand side. The sensitivity analysis

from Section 3.1 indicates that the acid can saturate the deep fracture and consume the rock uniformly in the face dissolution. The dissolution pattern has a relatively high dissolution rate as well. Therefore, the fracture roughness investigation under the current parameters will guide us for the practical acidizing project.

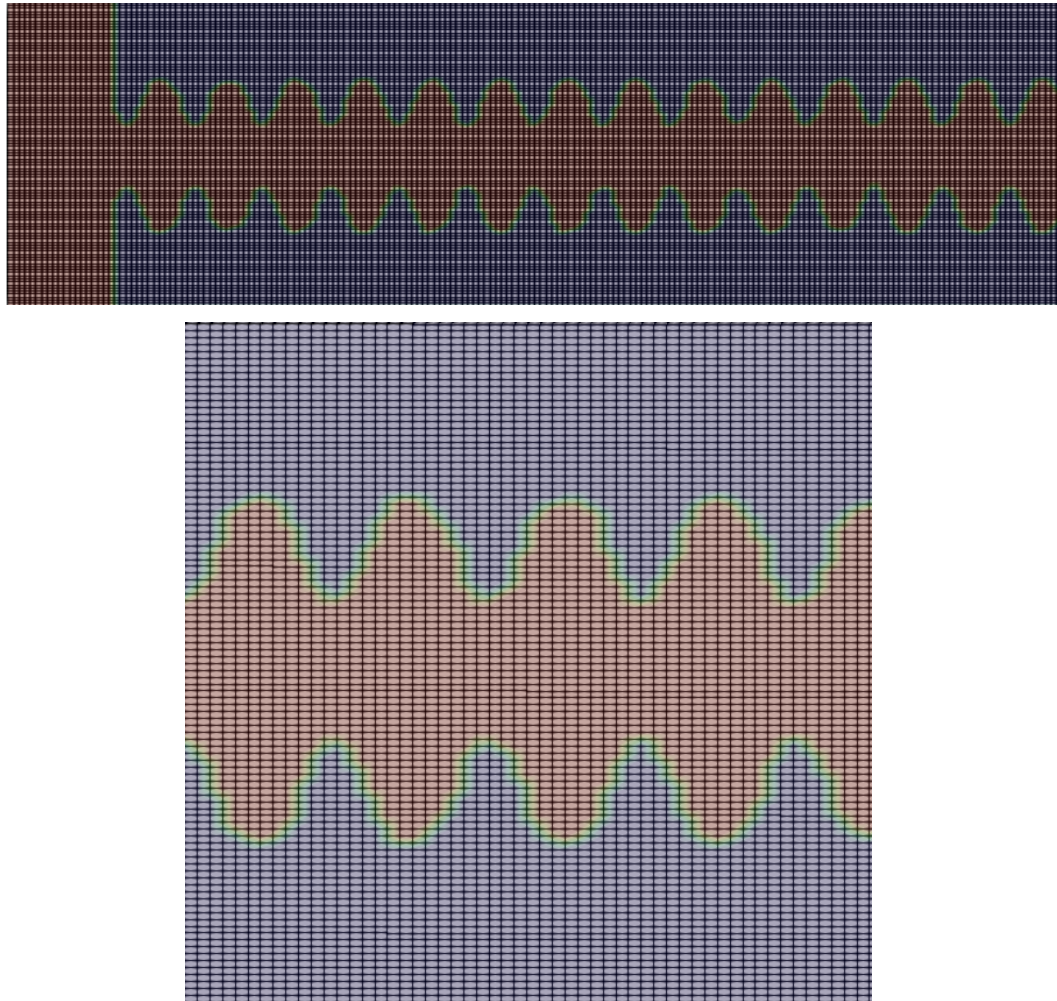


Fig. 5-6 The discretization of the computational domain (above) and the expanded view (below).

Table 5-2 Geometric parameters of single sine wave profiles and the corresponding surface roughness pattern.

	<i>WL</i> (mm)	<i>a</i> (mm)	Roughness factor	Surface roughness pattern
P1	5.815	0.10	1.004	
P2	1.163	0.10	1.063	
P3	0.831	0.10	1.135	
P4	5.815	0.25	1.025	
P5	1.163	0.25	1.331	
P6	0.831	0.25	1.643	
P7	5.815	0.38	1.056	
P8	1.163	0.38	1.647	
P9	0.831	0.38	2.192	
SW1	0.850	0.08	1.082	
SW2	0.850	0.30	1.791	
SW3	0.850	0.38	2.115	
SW4	1.350	0.10	1.052	
SW5	1.350	0.20	1.190	
SW6	1.350	0.30	1.382	
SW7	1.350	0.35	1.491	
SW8	2.000	0.05	1.006	
SW9	2.000	0.15	1.053	
SW10	2.000	0.25	1.140	

Table 5-3 Geometric parameter of multiple sine wave profiles and the corresponding surface roughness pattern.

	WL_{\max} (mm)	a_{\max} (mm)	WL_{\min} (mm)	a_{\min} (mm)	Roughness factor	Surface roughness pattern
M1	0.067	0.30	0.0190	0.0600	1.024	
M2	0.111	0.30	0.0092	0.0675	1.028	
M3	0.222	0.30	0.0114	0.0675	1.020	
M4	0.183	0.30	0.0058	0.0675	1.026	
M5	0.333	0.30	0.0139	0.0675	1.013	
M6	0.833	0.30	0.0139	0.0675	1.006	
M7	0.067	0.15	0.0139	0.0360	1.017	
M8	0.278	0.10	0.0139	0.0300	1.008	
M9	0.278	0.08	0.0003	8.0000	77.198	
M10	0.067	0.09	0.0222	0.1000	1.006	

Table 5-4 Parameters in the simulation

Parameter	Symbol	Value
Fluid density	ρ_l	920 kg·m ⁻³
Fluid viscosity	μ_l	2.4 × 10 ⁻³ Pa·s
Injection velocity	v_{inj}	1 × 10 ⁻⁴ m·s ⁻¹
Constant of reaction	k_r	5 × 10 ⁻³ m·s ⁻¹
Molecular diffusivity of acid	D_A	5 × 10 ⁻⁹ m ² ·s ⁻¹
Density of calcite	ρ_s	2710 kg·s ⁻²
Inlet acid concentration	$\bar{\omega}_{f,A0}$	1 wt%

Fig. 5-7 shows the acid concentration in the fracture at the initial stage when the acid saturated well and did not consume the rock. In general, the acid concentration decreased along

the horizontal direction in the fracture. In the fracture with high wave amplitudes and short wavelength, the acid cannot saturate well the trough (trough and crest area were highlighted in Fig. 5-8 (h)), such as Fig. 5-8 (e), (f), (h), and (i). As shown in Fig. 5-8, the velocity streamlines and vector distribution show the acid transport direction and magnitude. The fluid flow has the highest velocity at the center of the fracture. However, velocity gradually decreased to about zero from center to rock surface. The transported acid changed its flowing pathway along the uneven surface, decreasing average velocity inside the fracture. In Fig. 5-8 (i), we observed some velocity circulation in the deep trough. Once acid flows into this area, it would be trapped. The streamline shows the different flow characteristics with time under various fracture geometric structures, resulting in different dissolution rate on the surface.

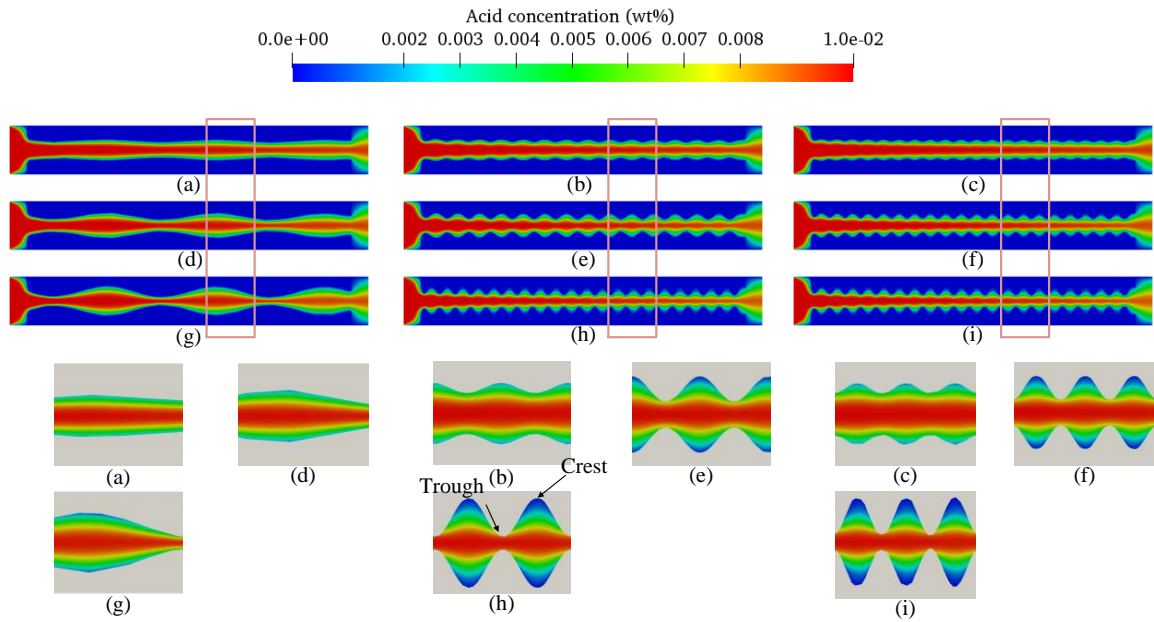


Fig. 5-7 Acid concentration for different surface roughness in the fracture. (a), (b), (c), (d), (e), (f), (g), (h), and (i) correspond to the case P1, P2, P3, P4, P5, P6, P7, P8, and P9, respectively. The bottom figures are the partial enlarged details for the highlighted area.

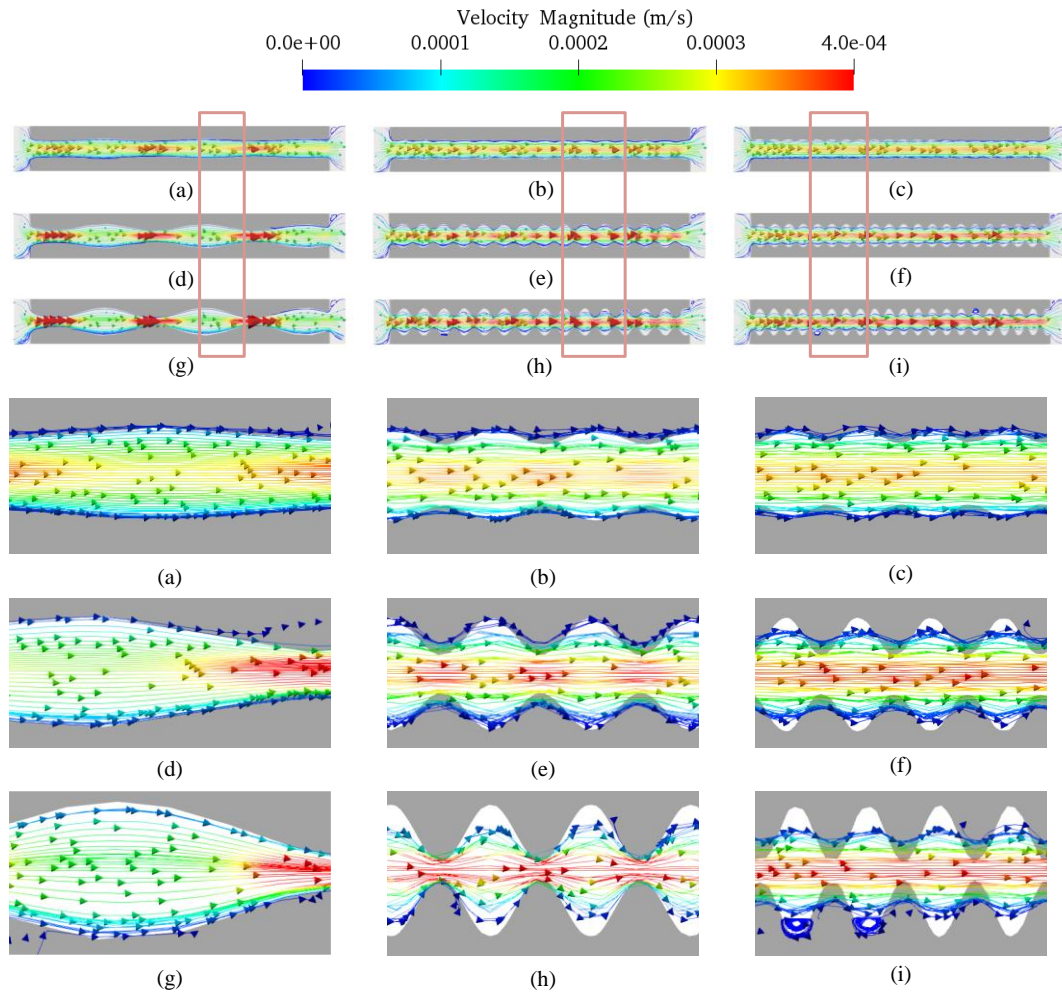


Fig. 5-8 Velocity streamline and velocity vector under different surface geometric model. (a), (b), (c), (d), (e), (f), (g), (h) and (i) correspond to the case P1, P2, P3, P4, P5, P6, P7, P8, P9, respectively. The streamline was colored by the velocity magnitude.

Fig. 5-9 shows the half side of the volume fraction of the pore space during the acidizing. The rough surface became smooth as acid consumed the rock, which indicated the different chemical dissolution rates on the fracture surface. Under small wave amplitudes (Fig. 5-9 (a), (b), and (c)), the surface became smooth as acid dissolved the rock; as the wavelength decreased, the surface was flatter after the reaction. However, as the amplitudes increased, the fracture surface with a large wavelength kept the original roughness configuration during the

dissolution. As shown in Fig. 5-10, the dissolution rate contours presented the larger dissolution rates on the fracture surface. The negative value of the dissolution rate represents that the carbonate mass weight decreased as the chemical reaction occurred. In the following section, we used the magnitude to plot the dissolution rate in curves. The acid firstly consumed the wave trough area, and the dissolution rate variation was eliminated on the surface at the latter reaction stage (as shown in Fig. 5-10 at $t = 27$ h).

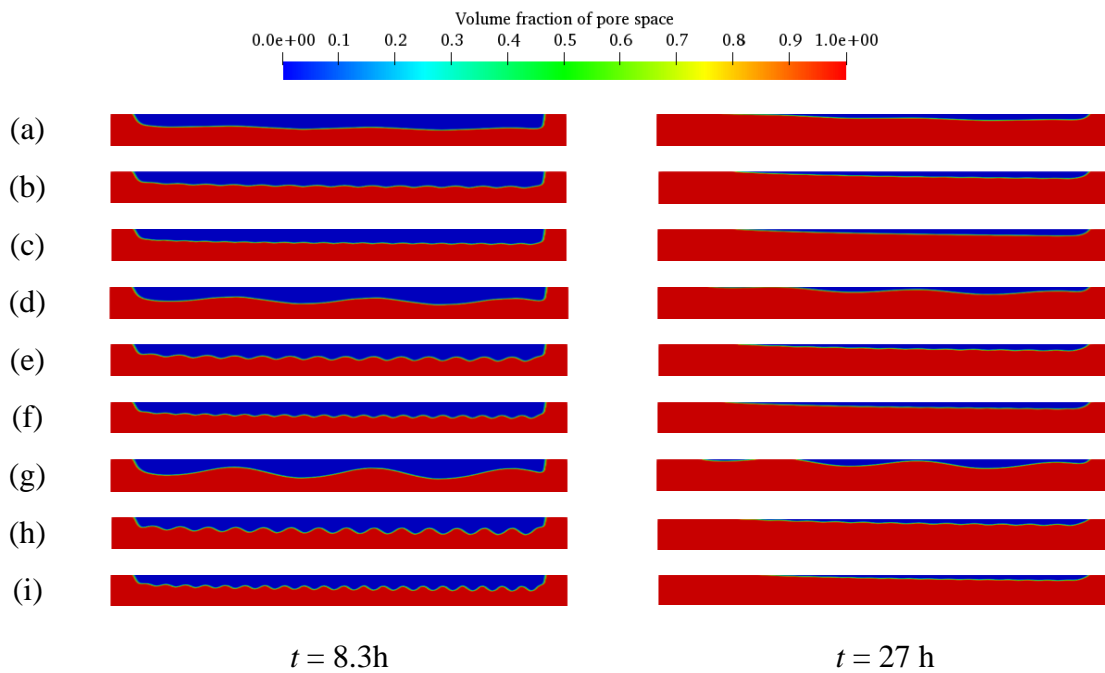


Fig. 5-9 The volume fraction of pore at different time of the half upper side of the computational domain. Red color represents the pore, and blue color represents the solid rock. (a), (b), (c), (d), (e), (f), (g), (h), and (i) correspond to P1, P2, P3, P4, P5, P6, P7, P8, and P9, respectively.

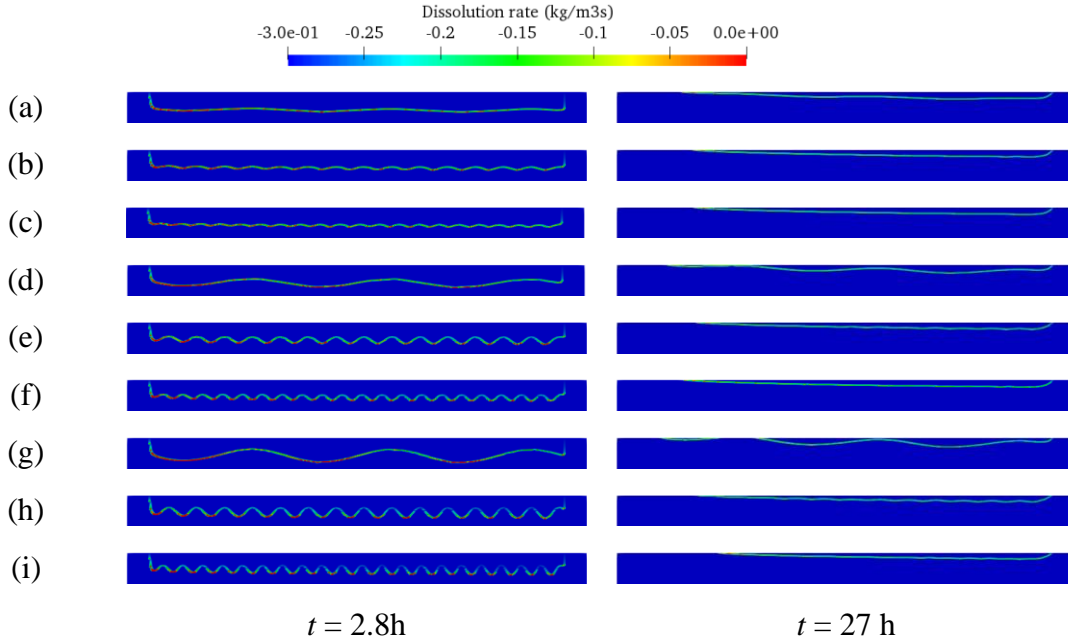


Fig. 5-10 Acid dissolution rate of upper side of the fracture. (a), (b), (c), (d), (e), (f), (g), (h), and (i) corresponds to the case P1, P2, P3, P4, P5, P6, P7, P8, and P9, respectively.

Fig. 5-10 (a) shows the normalized porosity–permeability relationship. The curves were obtained from the averaged local permeability and local porosity over the computational domain. The black curve denotes the cubic law under parallel plane fracture with constant aperture, and the black dots exhibit the simulation result of the smoothed fracture in the present work. The acidizing process significantly increased the permeability in the fracture with roughness. P1, P2, and P3 had the smallest amplitudes, and their wavelength decreased sequentially. Under different wavelengths, P4, P5, and P6 had the same medium amplitudes, and P7, P8, and P9 had the largest amplitudes. Among small amplitudes (P1, P2, and P3) and medium amplitudes (P4, P5, and P6), medium amplitudes cases had faster permeability growing as the porosity increased. Under the same amplitudes, as the wavelength decreased, the normalized porosity–permeability curves became steeper, which denoted that acidizing

minerals could significantly increase the permeability. This tendency was also shown in the cases SW1-SW10 in Fig. 5-12 (a). When the amplitudes were 0.0001 m and 0.00025 m, the porosity- permeability curve became steep with the decrease of the roughness factor. However, when the amplitudes were 0.00038 m, this trend was inverted.

The calcite dissolution rate is shown in Fig. 5-11 (b). The dissolution rate reached to a maximum value around $t = 4$ h and then decreased. The larger amplitudes cases (P7, P8, and P9) had the higher maximum dissolution rate, where the dissolution rate of P8 and P9 decreased fast after reaching the maximum value. The effective surface area was highly relevant to the surface roughness (Fig. 5-11 (c)). Before $t = 8$ h, the effective surface area was large when the roughness factor was high. The effective surface area partially determined the dissolution rate. For example, P6 and P9 had the faster declining speed; accordingly, their dissolution rate was low at the latter stage. The effective surface area curve displayed a flat “S” shape. The dissolution rates of P1, P4, and P7 were mainly dominated by acid transport instead of the effective surface area. These three cases had the lowest effective surface area values; however, their dissolution rate was not the lowest throughout the whole reaction. The small roughness factors led to a small acid concentration gradient within the fracture, and more acid can be accumulated near the fracture’s surface. The changing normalized porosity with time was displayed in Fig. 5-11 (d). P8 had a larger effective surface and dissolution rate; thus, the normalized porosity was large at the end. The smaller amplitude cases had larger relative porosity growth after the reaction (P1, P4, and P7).

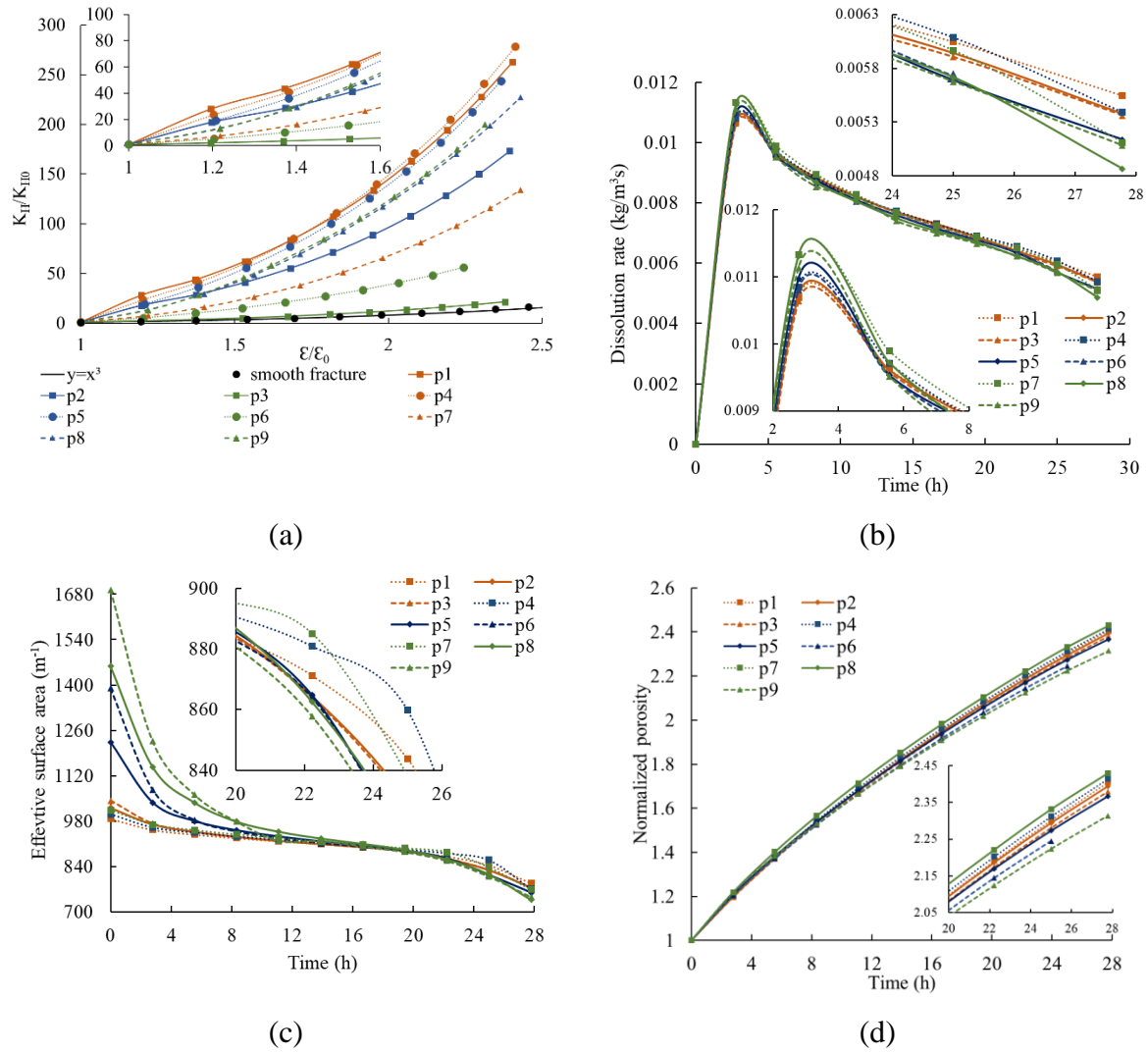


Fig. 5-11 (a) Normalized permeability with normalized porosity for cases P1-P9; (b) Dissolution rate with time for cases P1-P9; (c) Effective surface area with time for cases P1-P9; (d) Normalized porosity with time for cases P1-P9.

To further understand the impact of fracture roughness on reactive transport and dissolution, we also conducted the cases SW1-SW10 to investigate more possible fracture roughness profiles. Fig. 5-12 (a) plotted the normalized permeability with normalized porosity. Under the same wavelength, the cases with larger amplitudes had the steeper normalized porosity–permeability curve. The roughness factor was related to the growth rate of porosity–

permeability curves. If the surface roughness factor of the fracture gets larger, the effective surface area gets larger as well, which directly affects the calcite dissolution reaction. At the same time, the acid concentration around the rock surface is also affected by the fluid transport, which is affected by surface roughness of rock. For example, the roughness factor of SW3, SW7, SW6, and SW2 decreased in order, and the steepness of SW3, SW7, SW2, and SW6 decreased subsequently. SW6 and SW2 had a very close roughness factor but displayed the different porosity–permeability curve, which implies that the structure and morphology of the fracture influenced the dissolution and reactive transport process. As the roughness decreased, the porosity–permeability curve approached the cubic law curve (black line). In Fig. 5-12 (b), the small wavelength and the larger amplitudes surface profile had a bigger effective surface area. However, a larger effective surface area did not always lead to a higher dissolution rate, as shown in Fig. 5-12 (c). In the fracture of small wavelength and large amplitudes sine wave profile, acid cannot saturate well in the micro–cave of the fracture surface. Thus, the dissolution rates of SW1 and SW2 were low during the dissolution. Although SW3 had a relatively large dissolution rate initially, it decreased faster from $t = 5$ h and kept the smallest value until the end. Under the same wavelength, the small amplitudes had a higher maximum dissolution rate. The dissolution rate of SW1 was slightly higher than that of SW2 because the amplitude and roughness factors were close. After the reaction, the larger wavelength profile had a higher dissolution rate from 5 h to 15 h.

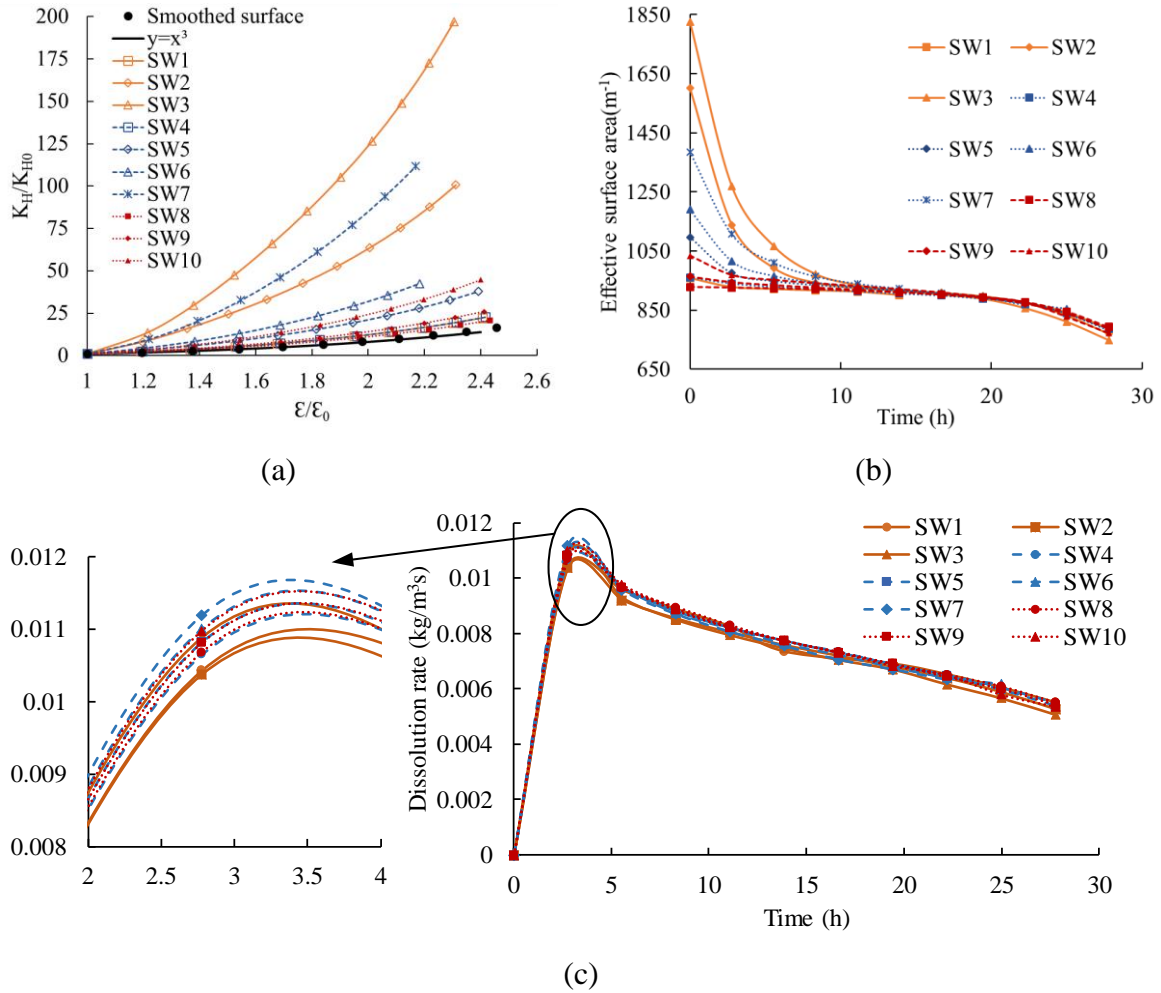


Fig. 5-12 (a) Normalized permeability with normalized porosity for cases SW1-SW10; (b) Effective surface area with time for cases SW1-SW10; (c) Dissolution rate with time for cases SW1-SW10.

Fig. 5-13 (a) shows the normalized permeability with normalized porosity under surface roughness of multiple sine waves. There was no obvious relationship between fracture roughness with the effective surface area (Fig. 5-13 (b)) and dissolution rate (Fig. 5-13 (c)). Permeability in M1 and M10 slightly increased with the porosity, and the porosity–permeability curve was close to the smoothed surface curve. Correspondingly, the effective surface area curves of M1 and M10 had an approximately linear declining tendency from 0 to 22 h.

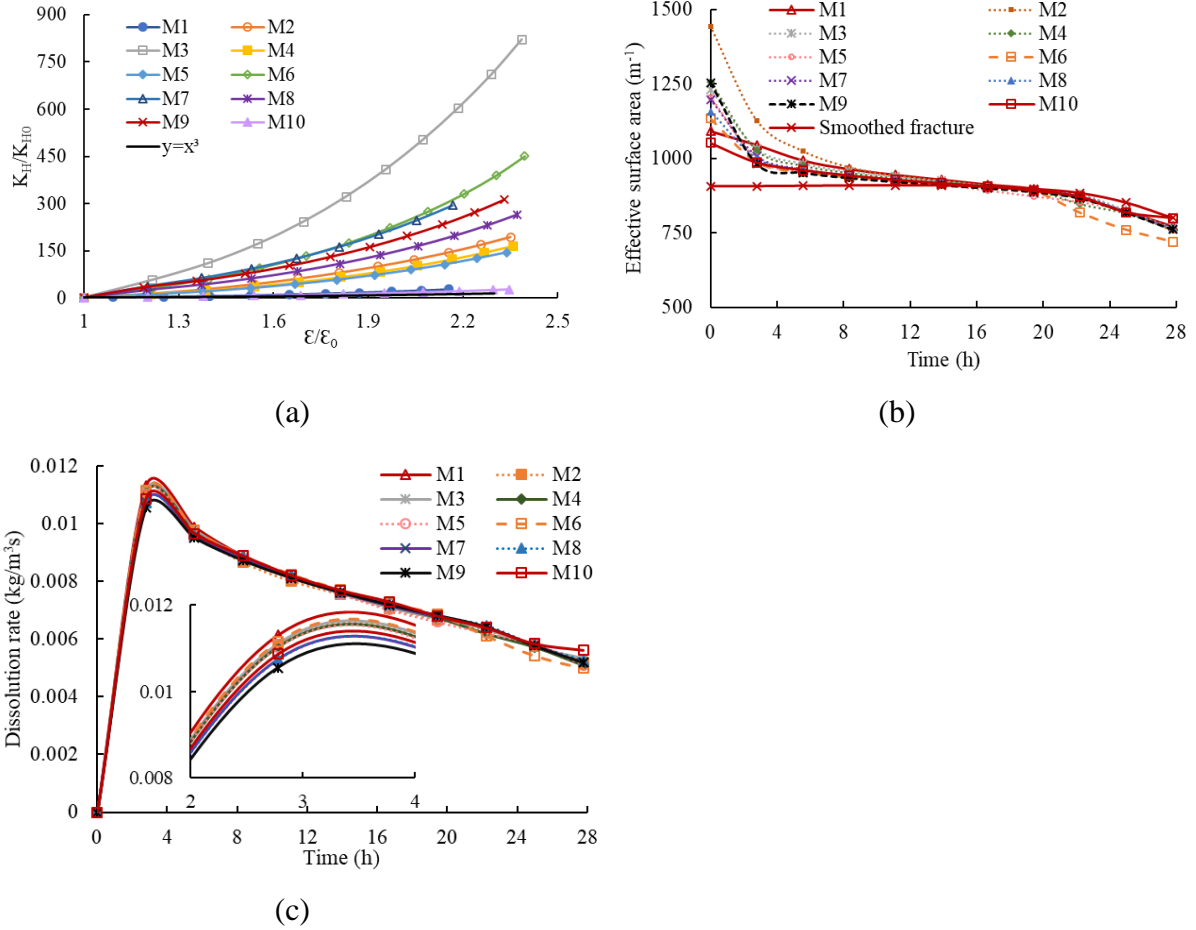


Fig. 5-13 (a) Normalized permeability with normalized porosity for cases M1-M10; (b) Effective surface area with time for cases M1-M10; (c) Dissolution rate with time for cases M1-M10.

We analyzed the different fracture widths of case m1, and the widths are 3.8 mm, 3 mm, and 2.8 mm, respectively. Fig. 5-14 shows the evolution of fracture and acid concentration during acidizing. The black color represents the rock matrix, and the colored distribution shows the acid concentration. Acid has relatively better saturation in the crest area when the fracture width is larger. With the smaller width of fracture, the rock was consumed faster. As shown in Fig. 5-15 (a), the acidizing has a slight impact on the permeability in the wider fracture. When the solid was almost consumed up, the permeability only showed a nine–time increase.

However, with the smaller fracture width, the acidizing had a significant impact on the permeability. The permeability showed about 300 times increase compared with the initial permeability. With the decrease of the fracture width, the dissolution rate increased. Because the acid velocity was larger under smaller fracture width, more acid was transported in the system and reacted with the rock.

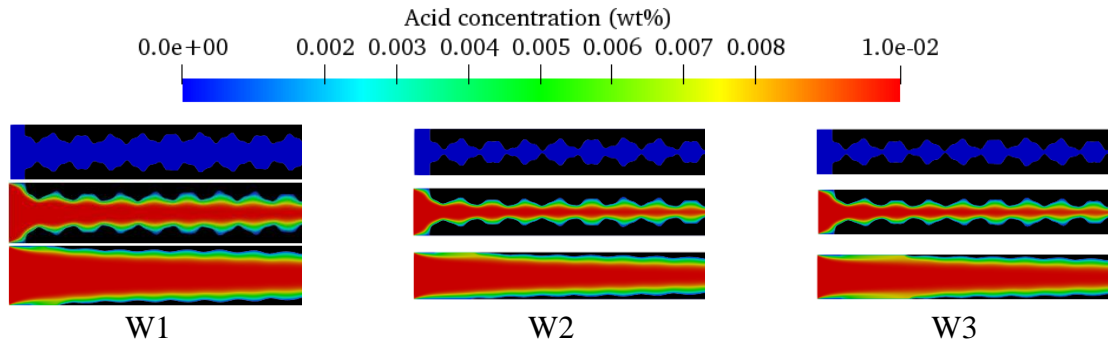


Fig. 5-14 Evolution of fracture during acidizing of different fraction widths. The first row was at the initial time. The second row and the third row were at 13.9 h and 27.8 h, respectively.

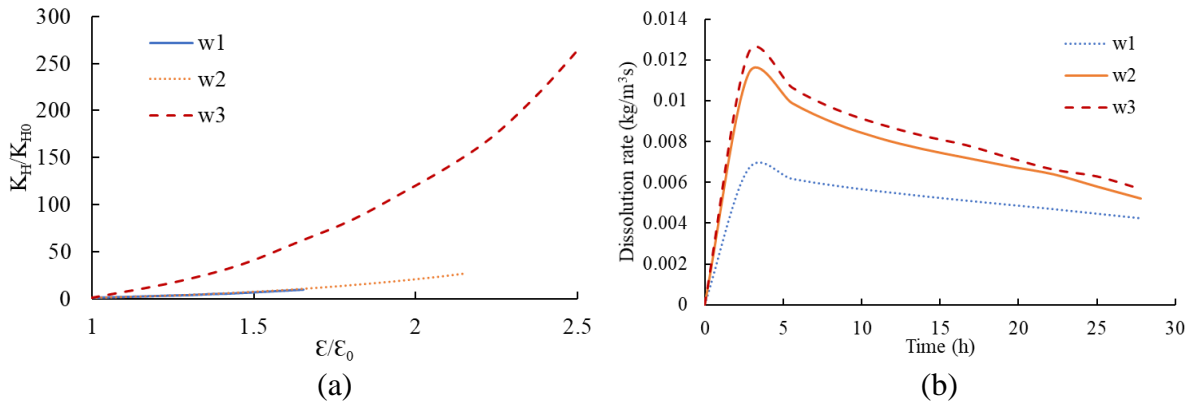


Fig. 5-15 (a) Normalized permeability with normalized porosity under different widths; (b) Dissolution rate with time under different widths.

5.5 Dissolution in mineralogical composition fracture

This section analyzed the dissolution in a μ CT image of an Indiana limestone sample with different calcite and quartz content (Shovkun & Espinoza, 2019), as shown in Fig. 5-17. The size of the sample was 1.35 mm in length and 0.25 mm in height. To thoroughly capture the fracture structure, the sample was discretized into 300×200 grids (shown in Fig. 5-16). The input parameter was same with the previous section. The initial permeability of the whole computational domain was about $5 \times 10^{-11} \text{ m}^2$. The Re number was about 10^{-4} . We assume that the rock was mainly composed of calcite and quartz. Quartz was stable and did not react with the acid. In the simulation, the quartz content was 0 vol%, 4.5 vol%, 5.6 vol%, 9.2 vol% and 12 vol%.

Fig. 5-18 shows the changing velocity streamlines with time during the acidizing. At $t = 1,000 \text{ s}$, the fracture aperture was small, and the velocity magnitude was relatively large within the fracture. As acid consumed the mineral, the fracture was enlarged, and averaged fluid velocity in the fracture was decreased. The unreacted quartz had obvious impact on the fluid flow after the surface calcite was consumed up, and quartz was exposed to the fluid. After $t = 1,000 \text{ s}$, the velocity was low near the quartz, and a few streamlines were distributed, especially under large quartz content. Since the quartz increased the fracture surface geometry's complexity, the velocity was large in the thin fracture and small near the surface.

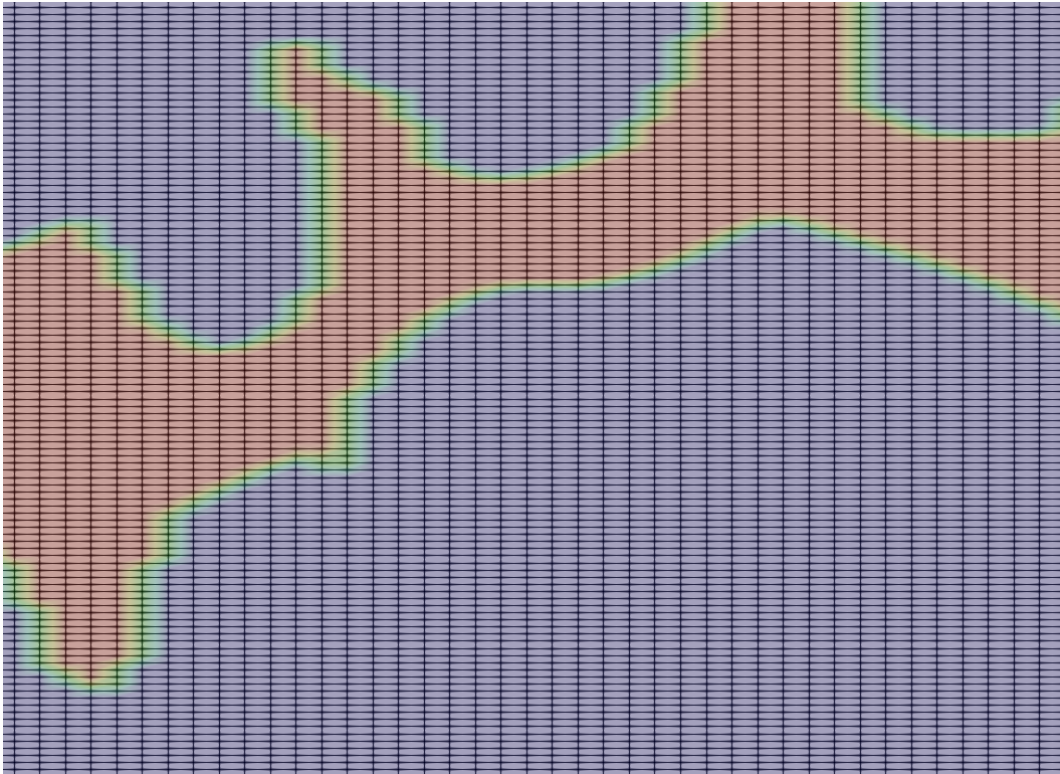
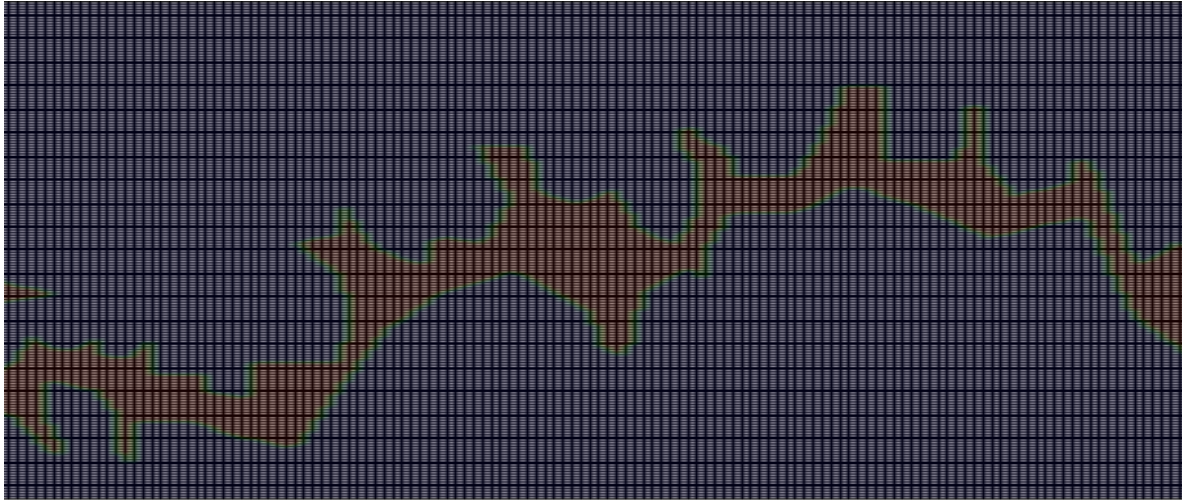


Fig. 5-16 The discretization of the computational domain (above) and the expanded view (bottom).

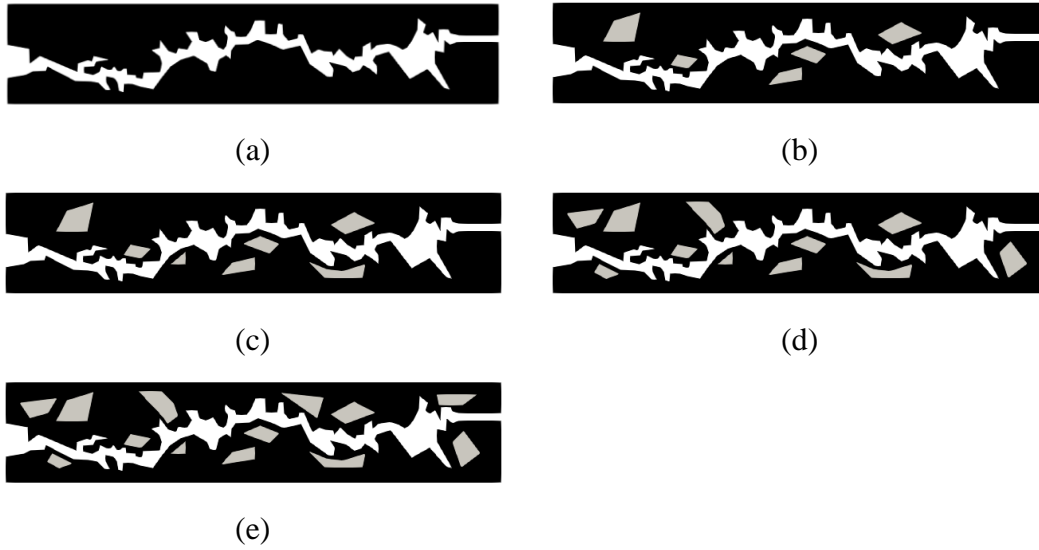


Fig. 5-17 μ CT image of Indiana limestone sample containing different contents of quartz: (a) 0 vol%; (b) 4.5 vol%; (c) 5.6 vol%; (d) 9.2 vol%; (e) 12 vol%.

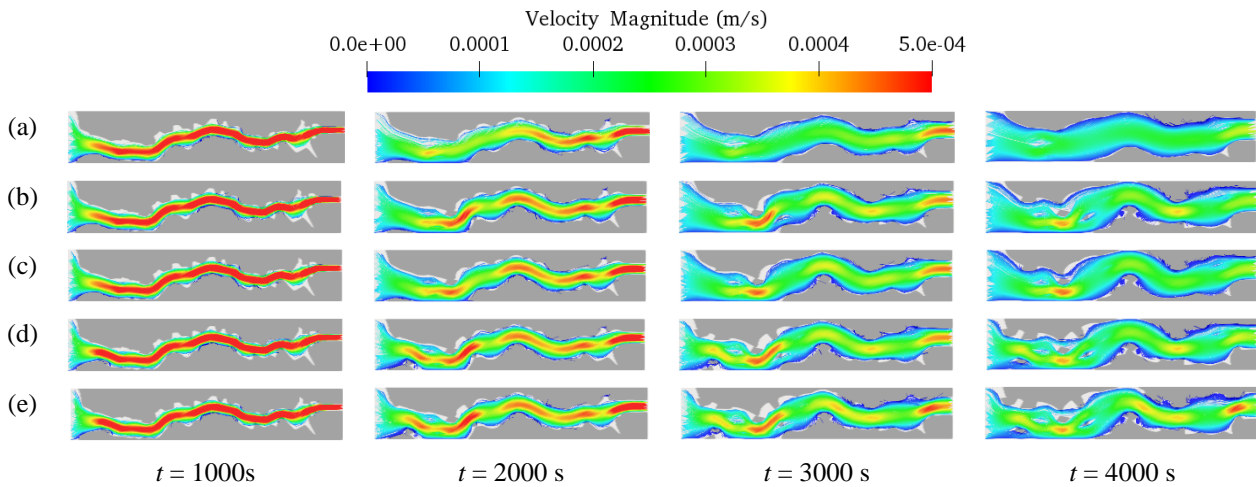


Fig. 5-18 Velocity streamline during the acidizing process with different mineralogical contents.

Fig. 5-19 (a) shows the average volume fraction of pore space with time. Before $t = 1,500$ s, the volume fraction of pore space curves did not differ under different quartz contents. After 1,500 s, with higher quartz contents, the volume fraction of pore space increased slowly.

At $t = 4,000$ s, the final volume fraction of pore space was 0.702, 0.686, 0.677, 0.666 and 0.651. During the acidizing, the quartz in the system resulted in the effective surface area's fluctuated variation. As shown in Fig. 5-19 (b), the effective surface has a slight increase initially and then decreased. The effective surface area decreased with fluctuation when the system contained the quartz. The consumed calcite smoothed the fracture surface, which caused the decreased tendency of the effective surface area. However, during the acidizing, the irregular quartz exposed to the fracture surface and changed the surface configuration, giving rise to the effective surface area's fluctuation. The dissolution rate was mainly influenced by the effective surface area and acid concentration. Thus, as shown in Fig. 5-19 (c), the dissolution rates showed fluctuation. Fig. 5-19 (d) shows the normalized porosity–permeability relationship. The pure calcite fracture had a great increase of permeability as porosity increased. With the increase of quartz content, the permeability growth was limited as quartz exposed to the fluid flow.

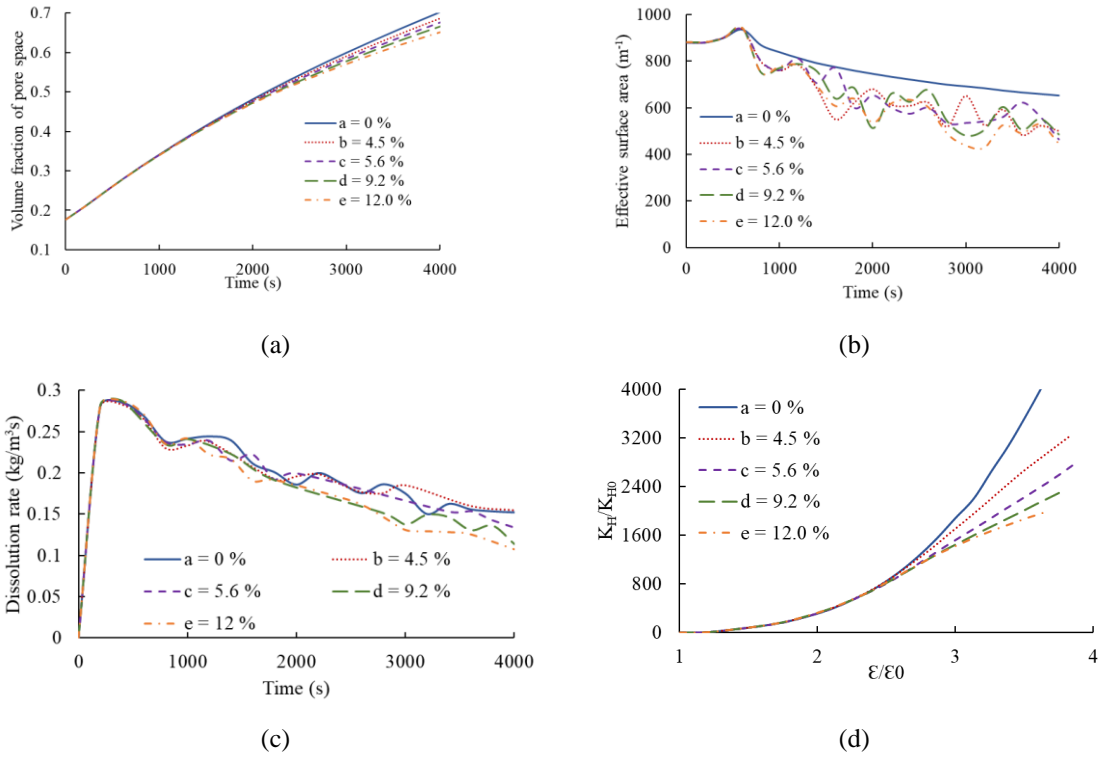


Fig. 5-19 (a) Changing volume fraction of pore space with time; (b) Changing effective surface area with time; (c) Changing dissolution rate with time; (d) The normalized porosity–permeability relationship.

6 INVESTIGATIONS OF MIXED-MINERALS SYSTEMS IN CO₂-ENRICHED BRINE INJECTION

6.1 Introduction

Previous study found that the clay coating was progressively developed, and quartz influenced the flow path as calcite reacted with CO₂-acidified brine, subsequently leading to the decreased of dissolution rate and permeability (Noiriel et al. 2007). CO₂ storage and sequestration are considered as an effective approach to mitigate greenhouse gas emissions. Injected CO₂ can easily move upward by buoyancy or leakage out of the target reservoir through the existing fractures, and negatively influences the CO₂ sealing capacity and security (Deng et al. 2013, Al-Khulaifi et al. 2018). While injecting an enormous amount of CO₂ into carbonate-rich aquifers, CO₂ dissolves in the formation brine under the large pressure, and the subsequently formed CO₂-enriched brine reacts with the calcite. Reaction-induced changes in pore structure and fracture geometry alter the porosity and permeability, giving rise to the concerns of CO₂ storage capacity and environmental safety.

Thus, this study aims to analyze the mineral-fluid interactions and subsequent permeability evolution in the heterogeneous fracture systems during CO₂ injection by implementing a pore-scale reactive transport model. We considered different fracture configurations, mineralogical components—montmorillonite clay, quartz, and calcite fracture-matrix system. During the injection of CO₂ enriched brine, the clay swells and influences the permeability of the system. An additional mineral of quartz was considered non-reactive, while calcite was consumed by carbonic acid. Different fracture configurations and mineralogical contents have been considered to investigate their impact on the dynamic porosity-permeability relationship, dissolution rate, and reactant transport characteristics during CO₂ storage. This work has been published in (You & Lee, 2022).

6.2 Mathematical model of injection of CO₂–acidified brine in mixed–mineral

Reactive transport is described by the multi–component advection–diffusion equation (Molins et al., 2012)

$$\frac{\partial \varepsilon_f C_{f,i}}{\partial t} + \nabla \cdot (u_f C_{f,i}) = \nabla \cdot (\varepsilon_f D_i \nabla C_{f,i}) - a_v R_i(C_{f,i}), \quad (6-1)$$

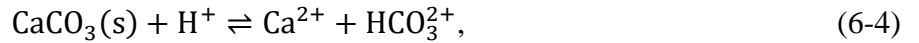
where $C_{f,i}$ is molar concentration of aqueous concentration of species i . D_i is the diffusion coefficient of species i . $R_i(C_{f,i})$ is the reaction rate of species i . a_v is the solid–fluid interface, which is used to make the reaction rate to be non–zero only at the solid–fluid interface. The evolution of rock geometry was calculated by the equation

$$\frac{\partial \varepsilon_s}{\partial t} = a_v R V_m, \quad (6-2)$$

where, R is the dissolution rate of calcite. The right term only has non–zero value on the solid–fluid interface. Thus, the dissolution starts from the solid–fluid boundary and the carbonate rock is consumed by the CO₂–enriched brine.

The dissolution starts from the solid–fluid boundary and the carbonate rock is consumed by the CO₂–enriched brine. The calculations of dissolution rate and the reaction of calcite pathway are as

$$R = (k_{r1} a_{H^+} + k_{r2} a_{H_2CO_3^*} + k_{r3}) \left(1 - \frac{a_{Ca^{2+}} a_{CO_3^{2-}}}{K_{s,cal}}\right), \quad (6-3)$$



where, V_m is the molar volume of calcite, which equals to 36.93 cm³/ mol; $K_{s,cal}$ is the equilibrium constant of the reaction; a_{H^+} , $a_{H_2CO_3^*}$, $a_{Ca^{2+}}$, and $a_{CO_3^{2-}}$ are the species activities calculated by the concentration of the species; k_{r1} , k_{r2} , and k_{r3} are the reaction rate constant

for different reaction pathways. The conditions are far from the equilibrium for the calcite so that we can take the thermodynamic driving force term as unity (Deng, Fitts, Crandall, McIntyre, & Peters, 2015).

The clay swelling and deformation was described by the momentum conservation equation for a plastic solid (Carrillo & Bourg, 2019):

$$\begin{aligned} \frac{\partial \varphi_s \rho_s \hat{u}_s}{\partial t} + \nabla \cdot (\varphi_s \rho_s \hat{u}_s \hat{u}_s) = & -\varphi_s \nabla (\hat{\sigma}_{conf} - \hat{p}_f I - \hat{p}_{swell} I) \\ & + \varphi_s \nabla \left(\mu_s^{eff} \left(\nabla \hat{u}_s + (\nabla \hat{u}_s)^T - \frac{2}{3} \nabla \cdot (\nabla \hat{u}_s) I \right) \right) - \varepsilon_f \mu_f k^{-1} (\hat{u}_s - \hat{u}_f), \end{aligned} \quad (6-7)$$

where, \hat{u}_s is the solid velocity; φ_s is the volume fraction of clay; ρ_s is clay density; $\hat{\sigma}_{conf}$ is confining pressure; \hat{p}_{swell} is swelling pressure; μ_s^{eff} is effective viscosity of clay. The swelling pressure is obtained by the semiempirical formulation proposed by Liu (L. Liu, 2013), which is determined by clay volume fraction and sodium concentration in the system. The solid effective viscosity was calculated by Herschel–Bulkley non–Newtonian plastic viscosity models (Spearman, 2017). The clay volume fraction is updated by the following mass balance equation

$$\frac{\partial \rho_s \varphi_s}{\partial t} + \nabla \cdot (\rho_s \varphi_s \hat{u}_s) = 0. \quad (6-8)$$

6.3 Validation of the numerical method

We have applied the developed DBS method in addressing the dissolution of calcite (You & Lee, 2021a, 2021b, 2021c, 2022). The good agreements between the numerical results and experimental results through various applications give us the confidence of the validation of the method. For the validation of calcite dissolution by CO₂–enriched–brine, we first

compared our numerical results with the published experiment of the injection of CO₂-solution into calcite (Agrawal, Raoof, Iliev, & Wolthers, 2020). The experiment was conducted in the calcite crystal. The solution was injected into the drilled channel with the radius of 2.5×10^{-4} m and the length of 2×10^{-3} m. The detailed parameters were listed in Table 6-1. The fluorescent dye solution was added to the injection solution to capture the pH distribution during the reaction. The solution was injected under two different flow rates of 5 $\mu\text{L}/\text{min}$ and 50 $\mu\text{L}/\text{min}$, which yielded average velocities of 4.2×10^{-4} m/s and 4.2×10^{-3} m/s, respectively.

Table 6-1 Concentration of aqueous species in the experiment (Agrawal et al., 2020).

Parameters	Value (mol/m ³)
H ⁺	1.26×10^1
CO ₂	1.07×10^{-2}
Na ion	2×10^2
Cl ion	2.13×10^2
Ca ion	0
PH	2
Temperature	25 °C
Pressure	0.1 MPa
Water saturation	1

In the numerical simulation, we set the same concentrations of species as the experiment on the inlet boundary condition. We first replicated the experimental condition in a 3-D geometric model. The calcite crystal had the radius of 2.5×10^{-4} m, and the drilled channel had the radius of 2.5×10^{-4} m and the length of 2×10^{-3} m. The calcite crystal was located at 2×10^{-4} m from the inlet boundary. The injection velocity on the inlet boundary was set as 4.2×10^{-4} m/s. The reaction constants for calcite dissolution were 0.083, 1.1×10^{-4} , and 1.5×10^{-5} mol/m²s

for k_{r1} , k_{r2} , and k_{r3} , respectively. The comparison of numerical results and experimental results are shown in Fig. 6-1. Fig. 6-1 (a) is the transmitted detector and the fluorescein detector of acid flow at 36,000s (Agrawal et al., 2020). Fig. 6-1 (b) is the pH value distribution in the 3D case from the numerical simulation at 36,000s. Fig. 6-1 (c) and (d) is the pH value distribution of the cross-section of the 3D case at Z direction, and the 2D case at 36,000 s, respectively. The white line denotes the calcite shape at the initial stage. After 36,000 s, the evolved lengths by calcite dissolution were around 187 μm and 170 μm at the left-hand side of the sample. At the same position, the evolved lengths from 2-D and 3-D numerical simulation were around 170 μm . The 2-D results are in accordance with the 3-D simulation, as shown in Fig. 6-1 (c) and Fig. 6-1 (d). Previous studies have proved that running several 2-D segmentation and then taking the average value can represent the 3-D model system (Fazeli, Patel, & Hellevang, 2018). Since the flow and reaction in the sample is symmetrical, we take the center cross section as the geometric model to run the simulation at the high flow rate (4.2×10^{-3} m/s) and the low flow rate (4.2×10^{-4} m/s). The average pH value and Ca ion concentration at outlet boundary from numerical results were compared with experimental results. Fig. 6-2 shows that the numerical results of pH value and Ca ion concentration match well with the experimental results under lower injection velocity of 4.2×10^{-4} m/s. Under higher injection velocity of 4.2×10^{-3} m/s, the difference of Ca ion concentration between numerical simulation and experiment was in the acceptable value of 6%.

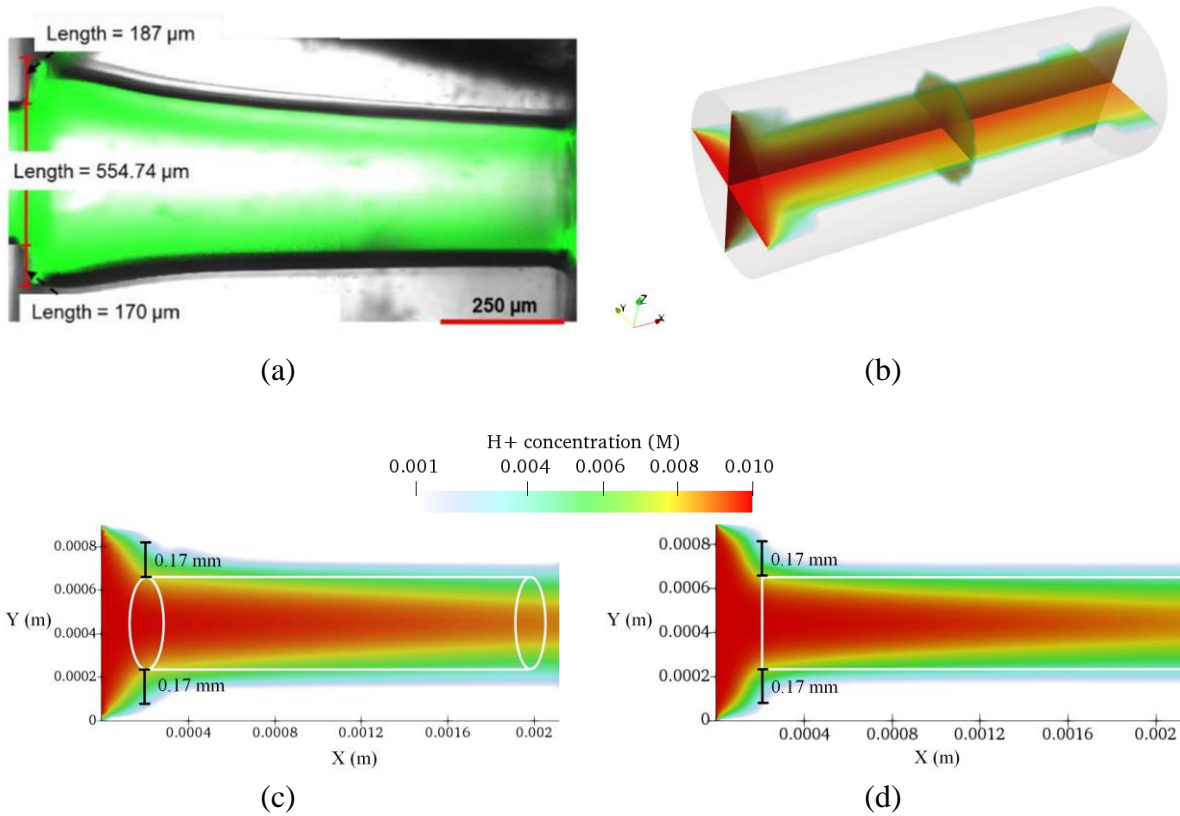


Fig. 6-1 (a) Images of the transmitted detector and the fluorescein detector of acid flow at 36,000s (Agrawal et al., 2020); (b) Numerical result of pH value distribution in the 3D; (c) Numerical pH value distribution of the cross-section; (d) pH value of the 2D case at 36,000 s.

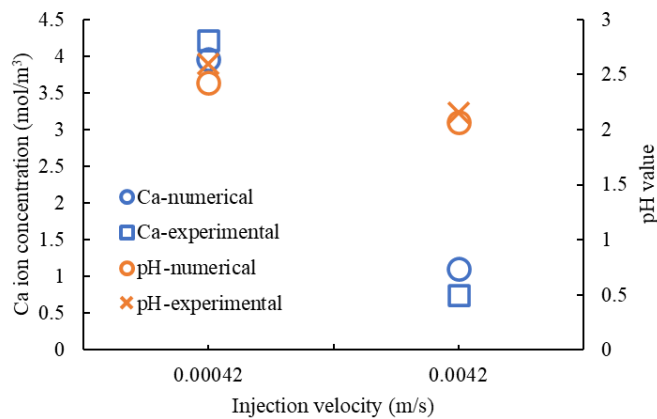


Fig. 6-2 Comparison of measured pH value and Ca ion concentration from experiment (Agrawal et al., 2020) and numerical simulation under different flow rates.

6.4 CO₂-enriched brine in fracture system

6.4.1 Problem background

To address the multi-species transport, calcite dissolution induced by CO₂ injection, and the subsequent change of permeability, we simulated the injection of the reactant (CO₂-enriched brine) into several fracture systems regarding different fracture density, connectivity, and branches' length. The fracture system was assumed to be composed of pure carbonate rock. The numerical investigation was conducted in a macro-scale geometry model with a size of 1.5 cm in length and 0.5 cm in height. The base case for the sensitivity analysis is referred from a 2D Micro-CT image of a tight reservoir (Ning et al., 2019), as shown in Fig. 6-3. In Fig. 6-3 (b), white color indicates the micro-fracture with aperture of 275 μm, and the gray color indicates carbonate rock. The inlet boundary condition is shown in Table 6-2 (Deng et al., 2015), and Section 6.5 used the same setting. The absolute permeability of the initial stage over the whole computational domain is about 2×10^{-10} m². The *Re* number was about 10⁻⁴. We considered deep saline brines saturated with CO₂ in the simulation, and the brine characteristics were measured under 27 °C and 10 MPa. At this condition, the reaction constants for calcite dissolution were 0.083, 1.1×10^{-4} , and 1.5×10^{-5} mol/m²-s for k_{r1} , k_{r2} , and k_{r3} , respectively (Molins et al., 2017). The reaction kinetics was implemented in the validation case in section 6.3 to compare with the published experiment, and we directly used that kinetic parameter in conceptual models. The chemical reaction kinetics and pathways have been investigated by sufficient studies and implemented in the pore-scale modelling to investigate the calcite dissolution in millimeter size model (Dashtian et al., 2019; Molins et al., 2017). Birkholzer et al. showed that the temperature of deep saline aquifer varied from 15 °C to 35 °C on the vertical profile from the aquifer top to bottom over 1,000 m below (Birkholzer, Zhou, & Tsang, 2009).

The reaction rate constants were derived from the experiment data of Pokrovsky et al. and adjusted by Molins et al. (Molins et al., 2017; Pokrovsky, Golubev, & Schott, 2005). The dissolution rate of calcite strongly depends on the H^+ concentration (Pokrovsky, Golubev, Schott, & Castillo, 2009). Alkattan et al. suggested that dissolved CO_2 in an aqueous solution leads to a decrease of pH value which depends on pCO_2 and temperature. However, under the same pH value of 4, the dissolution rate of calcite has a weak dependence on pCO_2 at 25, 60, 100, and 150 °C (Pokrovsky et al., 2009).

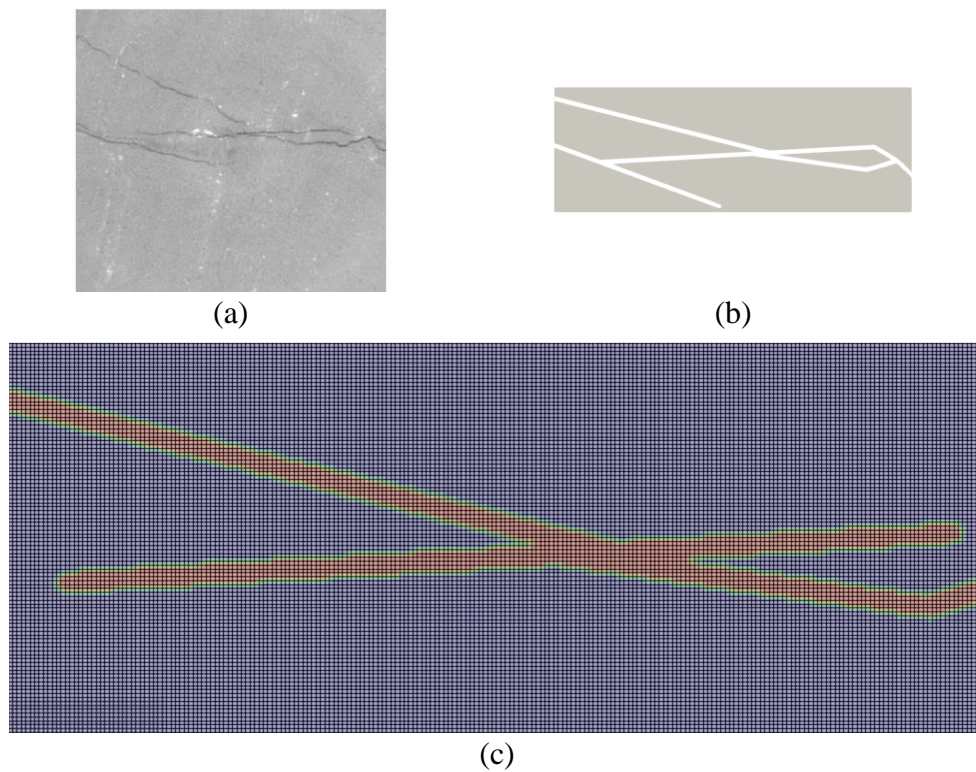


Fig. 6-3 (a) 2D Micro-CT image of tight reservoir (1.5×1.35 cm) (Ning et al., 2019). (b) Geometric model for the simulation. The size is 1.5 cm in length and 0.5 cm in height. (c) Discretization of the computational domain with resolution of 300×100.

Table 6-2 Boundary condition and parameters for the simulation (Molins et al., 2017).

Parameters	Value
PH	4.38
CO ₂	0.98 mol/kgw
Ca ion	6.4×10^{-3} mol/L
Na ion	1 mol/L
Cl ion	1 mol/L
Diffusion coefficient	2×10^{-9} m ² /s
Inlet velocity	5×10^{-5} m/s
Brine viscosity	1×10^{-3} Pa·s
Water saturation	1

In typical mm-scale natural fracture models (shown in Fig. 6-4 (a)), the fracture distribution is random and highly heterogeneous (Berre, Doster, & Keilegavlen, 2019; Ni, Chen, Li, & Gao, 2017; Singh & Cai, 2019). Thus, we selected our models with various fracture densities, length, and connectivity.

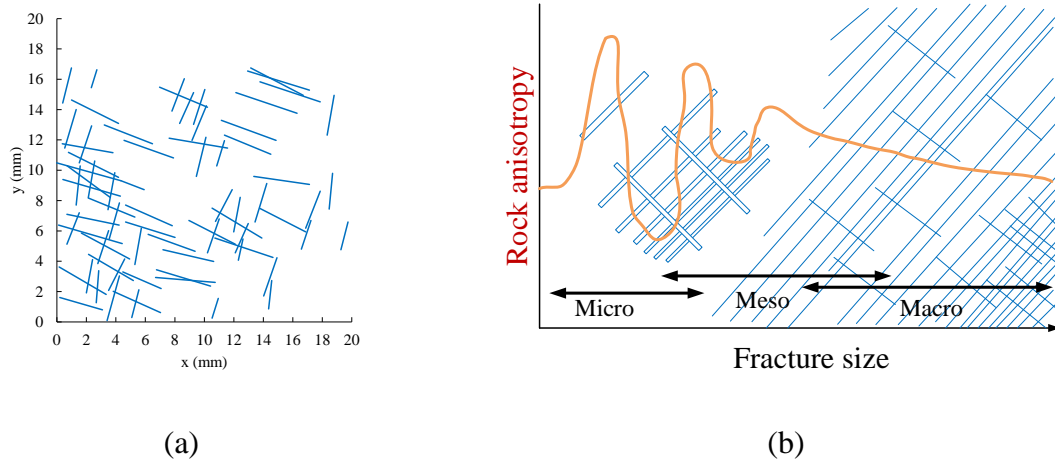


Fig. 6-4 (a) Typical mm-scale natural fracture model; (b) The relation of fracture size and the rock anisotropy (Concil, 2017).

6.4.2 Effects of fracture density

The fracture system evolution with different density is shown in Fig. 6-5 (black color). The fracture density increases from D1 to D5, and the fractures are randomly distributed. In D1, the system only has one fracture from inlet to outlet, and in D2, D3, D4, and D5, the systems have more fractures. In the system with high fracture density, the fracture was well connected. Thus, the acid could saturate the samples well, especially at the branches. For example, high pH values were distributed in the highlighted area in D1, D2, and D3. However, in D4 and D5, several fractures intersected with the dead-end branches. More acid was transported in the system, and the pH value was lower in the highlighted area. At the initial time, Ca ions were mainly distributed in the main path and near the inlet side. As CO₂-enriched brine reacted with calcite, Ca ions were accumulated in the system, and fractures were enlarged. Most generated Ca ions flowed out of the system through connected pathways, and some were trapped in the deep area of dead-end branches (Fig. 6-6 (a)). The black color denotes the rock in the system, and cases D1, D2, D3, D4, and D5 contained the different densities of the fracture. In the high-density system, Ca ions flowed out of the system easily; Ca ion concentration was high in the dead-end branches. Ca ions only occupied the deep area of dead-end branches compared with the low-density system in which occupies the whole length of branches. The changing total amount of Ca ions in the system is shown in Fig. 6-6 (b). Ca ions were accumulated in the system first, and as the fracture was enlarged, Ca ions flowed out of the system. The amount of Ca ions decreased after around $t = 46$ h. Before about $t = 30$ h, the higher-density cases showed higher Ca ions amount. Because more reactants were saturated the system, and more calcite was consumed. During the reaction (between $t = 30$ -80 h), the high-density cases had a good

connection and transported more Ca ions out of the system, as significantly decreasing the Ca ions amount.

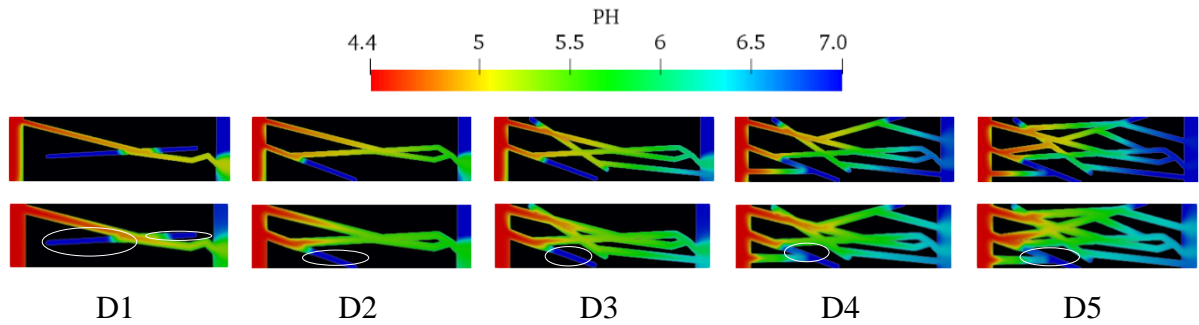


Fig. 6-5 Changing pH in the fracture systems with different fracture density at $t = 27.8$ h (first row) and $t = 83.3$ h (second row).

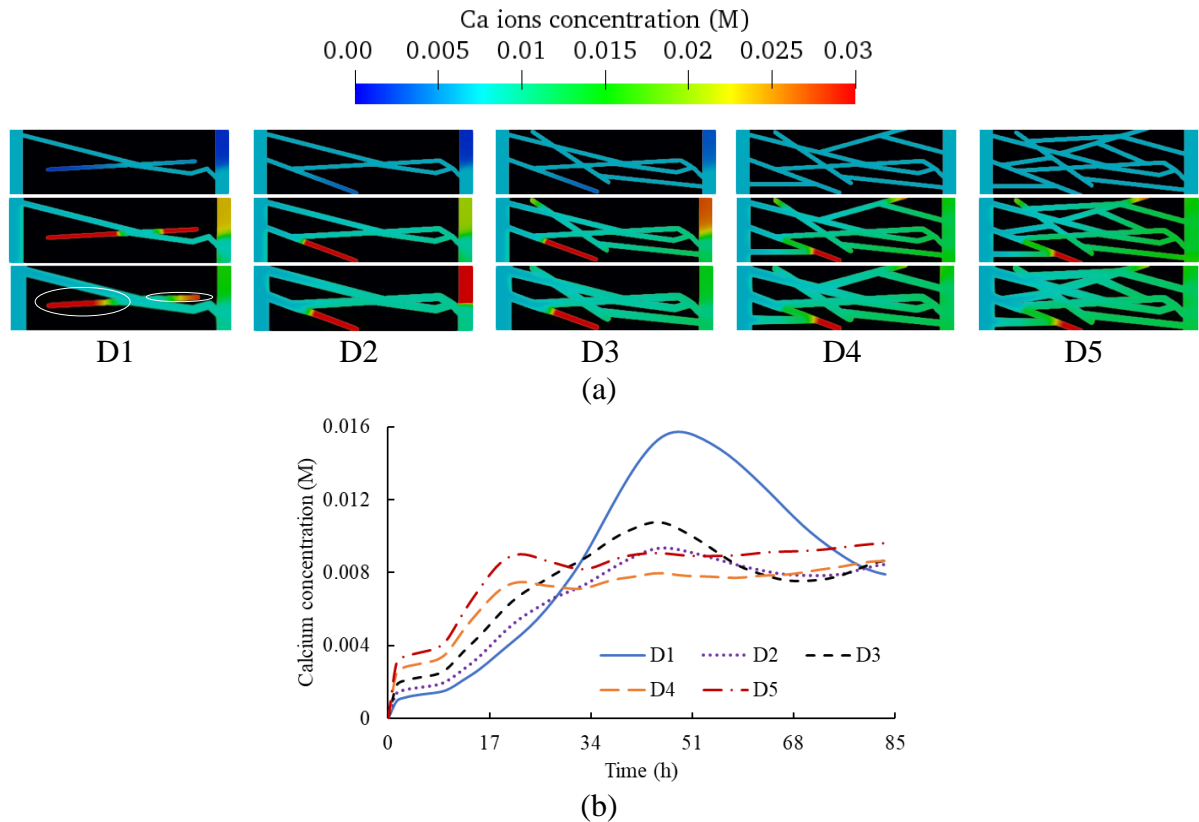


Fig. 6-6 (a) Ca ion concentration and fracture evolution during the CO_2 injection. The first row is at the beginning time of injection ($t = 1.38$ h). The second row and third row are at $t = 27.8$ h and $t = 83.3$ h, respectively; (b) Changing Ca ion concentration over time.

Fig. 6-7 shows the average total dissolution rate and the dissolution rate of different reaction paths. In general, the dissolution rates increased first and then decreased. A higher density fracture system had a higher dissolution rate, because more fractures in the system significantly increased the reactive surface area, and more reactants were transported in the system. R1 and R2 in Fig. 6-7 (a) and (b) denote the dissolution rate devoted by the hydrogen (Eq. (6-4)) and carbonic acid (Eq. (6-5)), respectively. The fracture density gave rise to the different transport patterns. Thus, dissolution rates raised by Eq. (6-4) and Eq. (6-5) all had significant variations in D1, D2, D3, D4, and D5 during the injection.

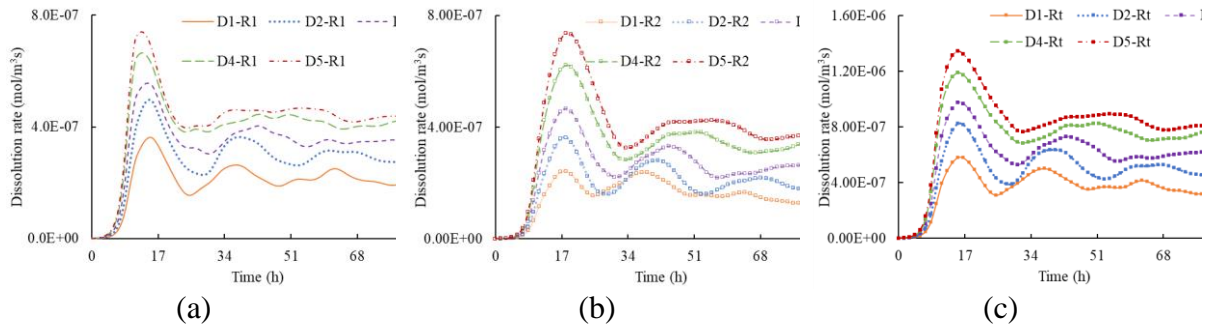


Fig. 6-7 Dissolution rate of different reaction paths under different fracture densities. (a) shows the dissolution rate contributed by the reaction of Eq. 5; (b) shows the dissolution rate contributed by the reaction of Eq. 6; (c) shows the total reaction rate for the calcite.

The normalized porosity–permeability relationship is shown in Fig. 6-8 (a). As CO₂ was injected, the systems with different densities had the noticeable increase of permeability, especially in D1. However, D3, D4, and D5 had similar porosity–permeability relationships. Although they had different density, the velocity streamlines distribution was very similar in these three cases. As shown in Fig. 6-8 (b), the paths followed by black arrows dominated the

fluid flow in the system. In D4, the paths denoted by red arrows were the additional paths to D3, where the velocity magnitudes were lower. Similarly, the paths with white arrows in D5 showed additional paths to D4. The calcite dissolution only enlarged the fracture apertures and did not change the fracture connection. Thus, the flow patterns were not changed, and porosity–permeability curves were similar in D3, D4, and D5.

Low density cases have good CO₂ storage capacity since the dissolution rate between acid and calcite was small. More calcium was trapped in the dead–end branches and limited the reaction rate at this area. The main paths dominated the flow pattern and other dead–end branches only had a slight influence on the porosity–permeability curve when the fracture densities were varying. When the system had similar fracture density, the branches length had the critical effects on the CO₂ storage capacity, because the fracture branches with short lengths were difficult to be penetrated by acid dissolution.

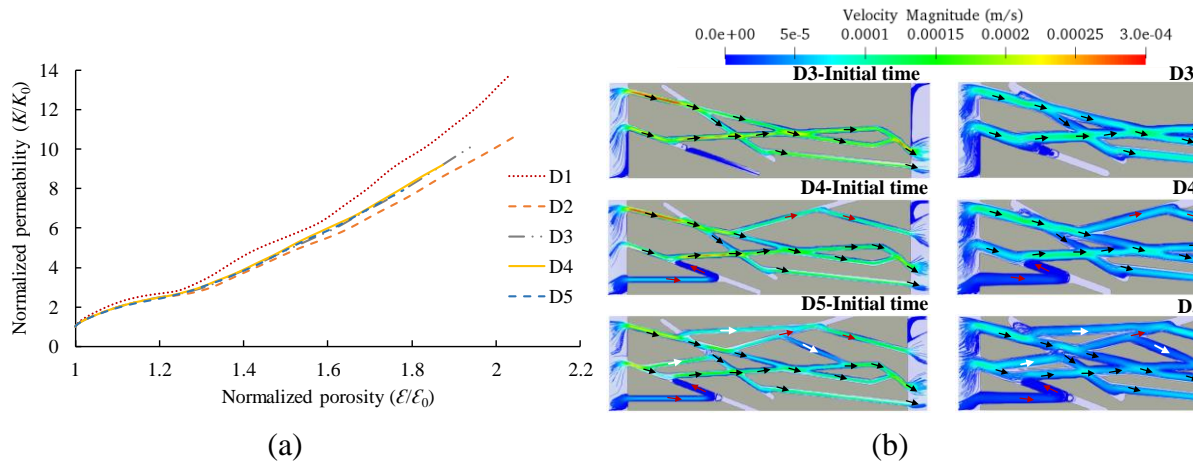


Fig. 6-8 (a) Normalized porosity and permeability relationship; (b) the velocity magnitude and streamlines. The black arrow denotes the main flow direction in D3. The red arrow denotes the additional pathway in D4, and white denotes the additional pathway in D5.

6.4.3 Effects of fracture length

Fig. 6-9 shows the Ca ions evolution under different branches' length at $t = 1.38$, 27.8, and 83.3 h. The black color denotes the rock in the system, and cases L1, L2, L3, L4, and L5 have the different lengths of the fracture branch. There are three main paths in the system, and the branches were attached to the main paths. We have generated five different patterns, which have some connected branches with different lengths attached on the main fracture. L1, L2, L3, L4, and L5 have different lengths of fracture branches from longer one to shorter one. At the beginning of injection, the dead-end branches (circled area in bottom-left of Fig. 6-9) had a low concentration of Ca ion. As CO_2 -enriched brine reacted with the calcite, a large amount of Ca ions was produced. This trend was similar with different density cases.

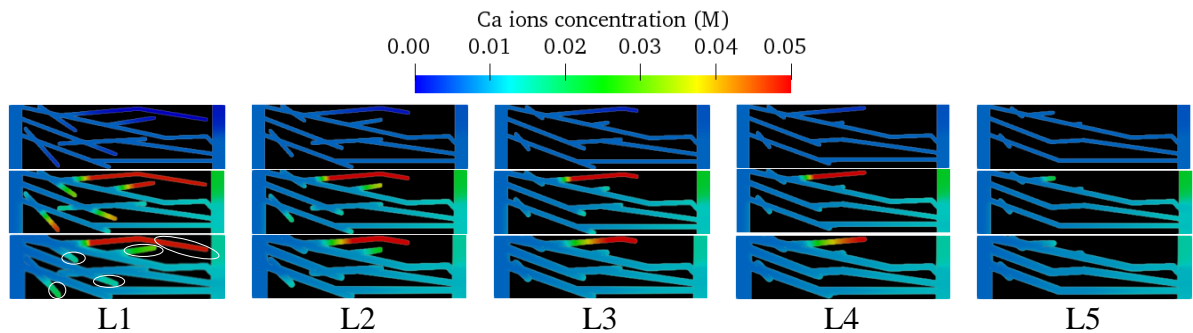


Fig. 6-9 Ca ion concentration and fracture evolution during the CO_2 injection. The first row is at the beginning of the injection ($t = 1.38$ s). The second row and third row are at $t = 27.8$ h and $t = 83.3$ h, respectively.

As shown in Fig. 6-10, low pH value was observed around the inlet area. Thus, the inlet side of the fracture showed a wider aperture than that of the outlet side. By the transport limitation, ion cannot saturate the deep area of the branches. As the calcite was dissolved, the fractures were enlarged, and some branches penetrated the rock intersecting to the main paths.

As shown in Fig. 6-11, the dissolution rates, contributed by the reaction of hydrogen ions, had the similar trends (Fig. 6-11 (a)). However, the reaction contributed by carbonic acid was more sensitive to the fracture geometry. The dissolution rate increased at the beginning and reached the maximum value. Then the reaction was limited due to the fact that the enlarged flow path decreased the concentration of the reactant inside the fracture, while the dissolution rate decreased gradually.

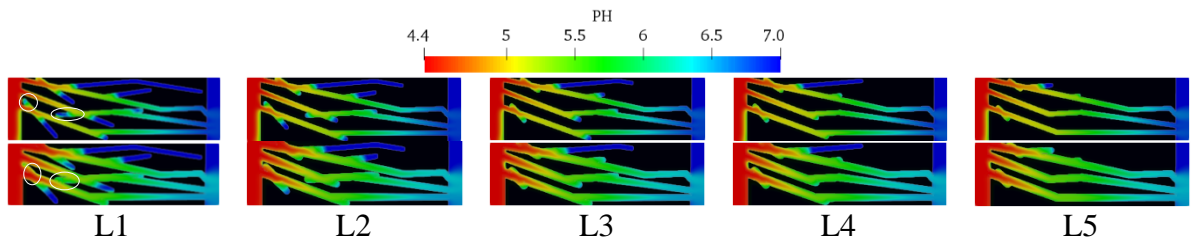


Fig. 6-10 Changing pH in fracture systems with different branch lengths at $t = 27.8$ h (first row) and $t = 83.3$ h (second row).

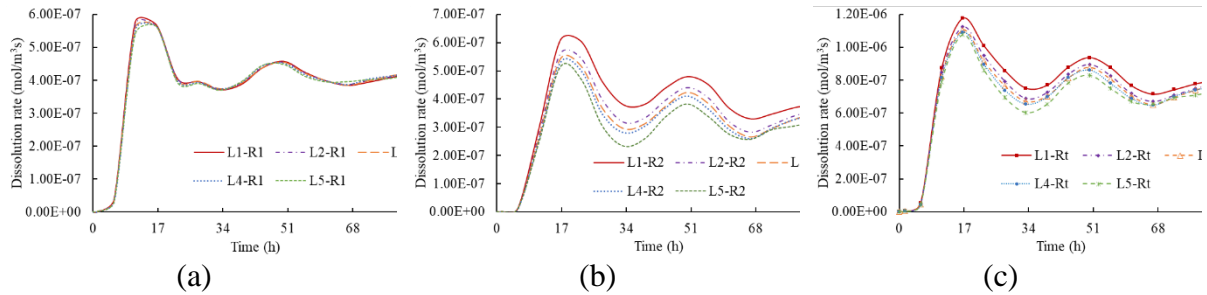


Fig. 6-11 Dissolution rate of different reaction paths. (a) indicates the dissolution rates contributed by the reaction of Eq. 5; (b) indicates the dissolution rates contributed by the reaction of Eq. 6; (c) indicates the total reaction rate for the calcite.

The normalized porosity–permeability relationship is shown in Fig. 6-12 (a). The fracture with longer branches had a faster growth of permeability as porosity increased. At the

initial stage, there was a slight difference in the porosity–permeability curve of each case. After the reaction, longer branches could penetrate the rock and enhanced the connection of the system, while significantly increasing the permeability in the system. The Ca ions accumulated faster in the longer lengths systems, since the longer length cases have larger reactive surface area and subsequently higher acid saturation. As the reaction occurred, the system with longer fracture branches became well connected, and a large amount of Ca ions flowed out of the system. Thus, the Ca ion concentration in L1 increased faster and then decreased. However, in L5 with shorter branches, the CO₂–acidified brine only enlarged the fracture around the inlet, and the connection condition for the system barely changed. The Ca ion concentration kept a mild increasing trend.

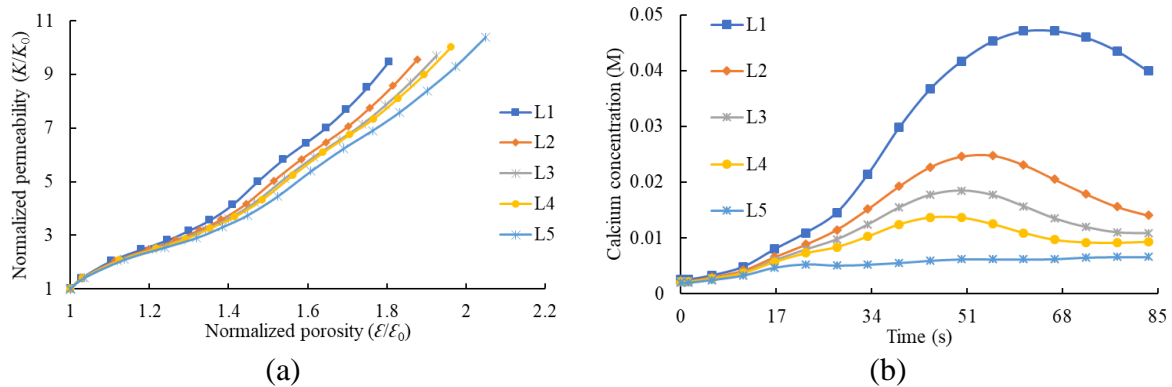


Fig. 6-12 (a) Relationship between normalized porosity and normalized permeability; (b) changing Ca ion concentration in the system.

6.4.4 Effects of fracture connectivity

We simulated four cases of fracture systems with different connection degrees. The geometry schematics are shown in Fig. 6-13. To investigate the effects of connectivity on the CO₂–enriched brine injection, we selected the following patterns. The primary fractures for

these four cases were similar, and branches in C1 were well connected to the primary fractures. C3 had three independent primary fractures with several branches attached. C2 and C4 had the differently intersected branches with the primary fractures.

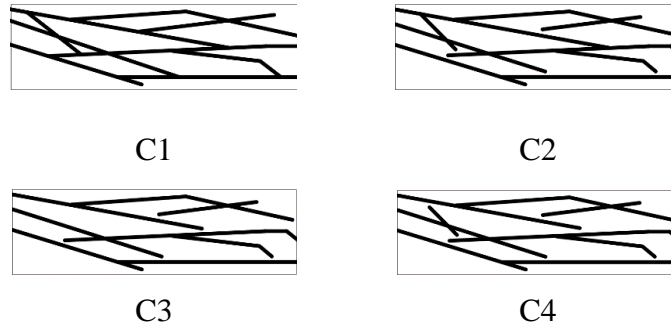


Fig. 6-13 Geometry schematics of fracture systems with different connections.

The pH distributions in the differently connected fracture systems are shown in Fig. 6-14. PH value was about seven at the end of branches in the poorly intersected branches. In C1, the highlighted branch in the first row was connected to the uppermost fracture, the middle fracture, and the bottom fracture. PH value was uniform inside this branch, and the rock was consumed up around this branch at $t = 83.3$ h (the third row). At $t = 83.3$ h, the highlighted fractures in C1 were enlarged, and at the same position C2, C3, and C4 only had slight evolutions. Ca ion concentration distribution over time is shown in Fig. 6-15 (a). The black color denotes the rock in the system, and cases C1, C2, C3, and C4 have the differently connected fracture. At $t = 27.8$ h, the end of branches accumulated the different amounts of Ca ions in the four cases. As the fracture evolution was induced by the mineral dissolution, the dead-end branches were intersected with other fractures, and Ca ions flowed out of the system. The distribution of Ca ions in C1, C2, C3, and C4 were almost similar at $t = 83.3$ h. This was

also shown in the curves of Fig. 6-15 (b). Ca ions were accumulated in the system with time, while the well-connected system had the lower Ca ions amount among four cases. After around $t = 37$ h, Ca ions amount decreased as Ca ions flowed out of the system. Ca ions amount of four cases gradually approached the same value at $t = 83.3$ h.

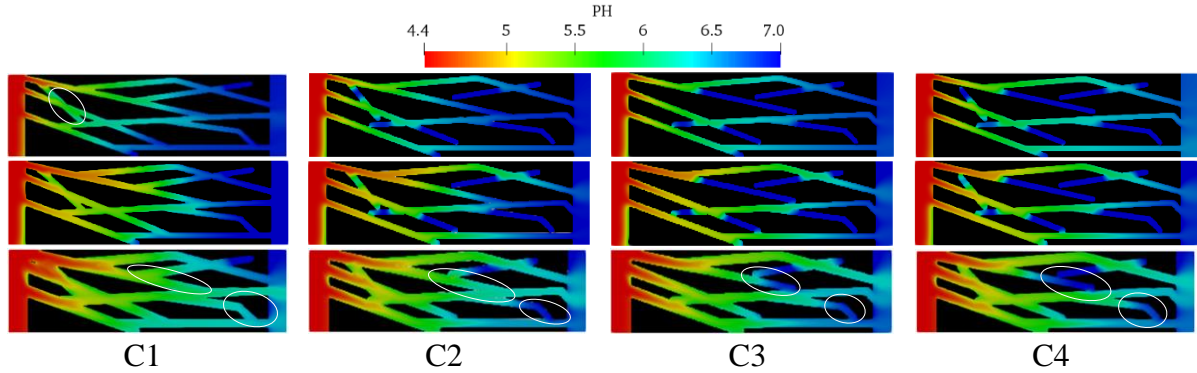


Fig. 6-14 Changing pH in fracture systems with different connectivity at $t = 15.3$ h (first row), 27.8 h (the second row) and 83.3 h (the third row).

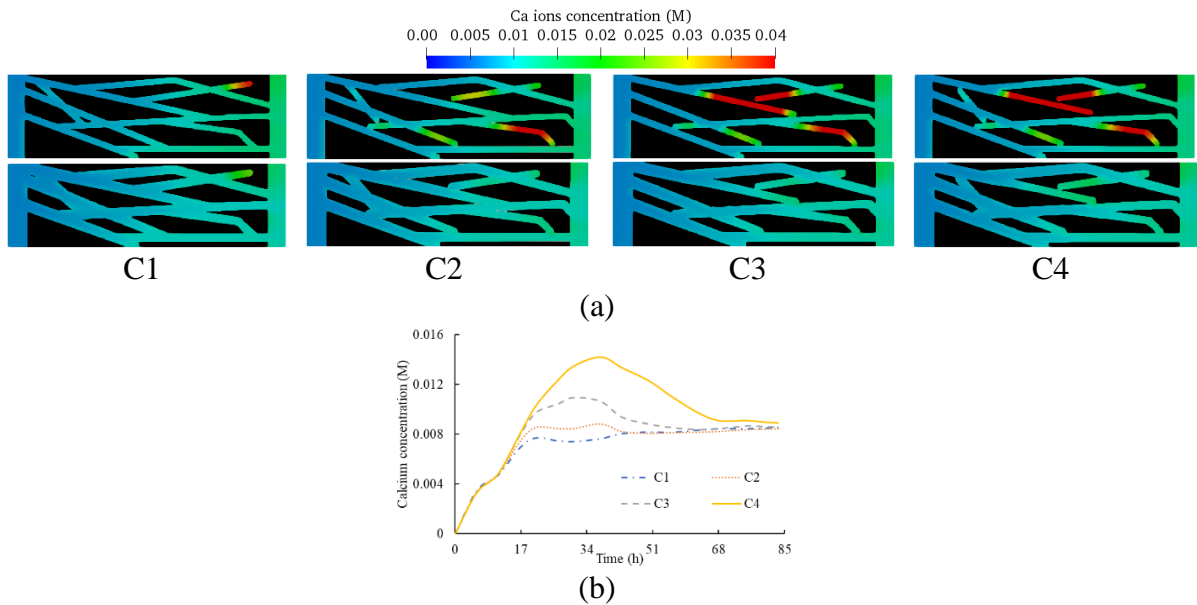


Fig. 6-15 (a) Ca ion concentration and fracture evolution during the CO_2 injection. The first row is at the beginning time of injection ($t = 1.38$ h). The second row is at $t = 83.3$ h; (b) changing Ca ion concentration over time.

The dissolution rates only had a slight difference in the four systems with different fracture connectivity. As shown in Fig. 6-16, the well-connected fracture cases had a relatively higher dissolution rate of minerals. The dissolution rate was contributed by the reaction of Eq. (6-4) and Eq. (6-5) and had a very similar value. However, the fracture connectivity led to the large difference of the porosity–permeability curves between the cases (Fig. 6-17 (a)). C3 and C4 had steeper porosity–permeability curves, because mineral dissolution greatly increased the fracture connectivity. Before the mineral dissolution, streamlines were only distributed in three main pathways in C3 and C4 at the initial time (Fig. 6-17 (b)). At $t = 83.3$ h, branches were connected to other fractures, and streamlines were distributed in almost every fracture and branch. C1 already had a well-connected fracture system, and only the aperture was enlarged caused by the dissolution, while the connectivity was not changed. Thus, the porosity–permeability had the slowest growth speed.

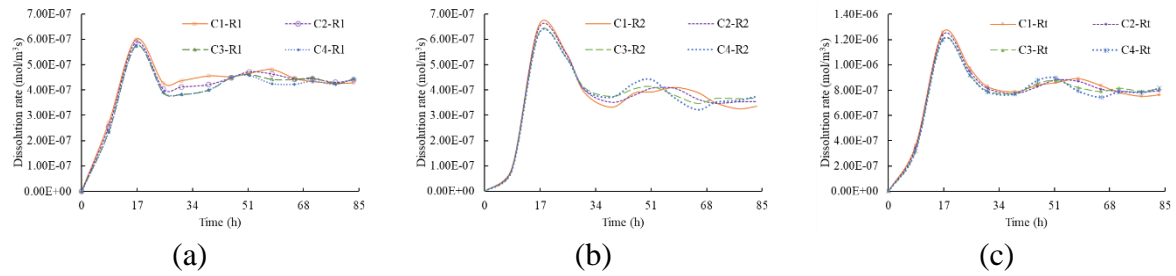


Fig. 6-16 Dissolution rate of different reaction paths. (a) shows the dissolution rate contributed by the reaction of Eq. 5; (b) shows the dissolution rate contributed by the reaction of Eq. 6; (c) shows the total reaction rate for the calcite.

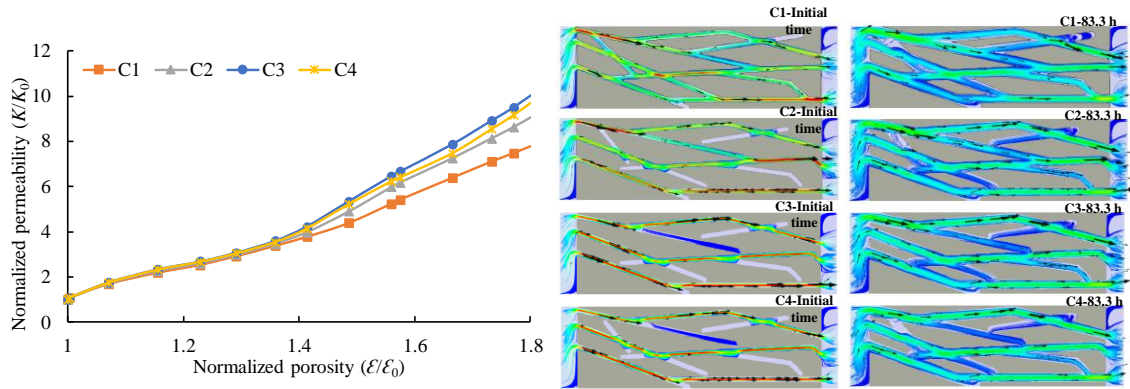


Fig. 6-17 (a) Normalized porosity and permeability relationship; (b) the velocity magnitude and streamlines.

6.5 CO₂-enriched brine in mineralogical compositions of the fracture-matrix

The rock structure, pore size, diameter of throat, and fracture aperture have dynamic changes during CO₂-enriched-brine injection, while some parts of solid zones are expanded, and some parts of solid zones are consumed. In this kind of condition, it's difficult to see the clear impact of multiple minerals on the fluid transport. Thus, a model describing the multiple mineral compositions can be used for clear quantification of the impact of presence of quartz and clay on the porosity-permeability relationship in calcite-dominant formations. The porosity and permeability curves are influenced by physical-and-chemical phenomena of calcite dissolution, clay swelling, and subsequent changes of rock morphology and compositions that are affecting fluid transport. So far, there are not much pore-scale studies that address the impact of multiple minerals on the porosity-permeability during the CO₂-enriched-brine injection, especially with the inclusion of clay swelling. One previous study has proved that the clay coating distributed around the calcite has significantly influenced the flow in the fracture (Noiriel et al. 2007). We expect that the porosity and permeability curves obtained from this study can quantitatively predict the impact of mineralogical compositions

on porosity–and–permeability evolution and subsequent fluid transport during the complex subsurface processes. In this regard, to elucidate the influence of the mineralogical compositions on the fracture–matrix system, we compared a pure calcite system (Fig. 6-18 (a)) with a quartz–calcite system (Fig. 6-18 (b)) and a clay–calcite system (Fig. 6-18 (c)). The geometry of the system was based on the micro X–ray image from Eagle Ford Shale (Peters, 2020). Quartz was regarded as a stable and unreactive mineral in the matrix, and was mainly distributed around the fracture, as shown in Fig. 6-18 (b). The fracture aperture was 1 mm; the length for the fracture was 5 mm; the height of the matrix for one side was 2.5 mm; the size of the geometrical model was referred from Er et al 2020 (Er, Babadagli, & Xu, 2010).

The Ca ion concentration and mineral evolution at $t = 1.4$ h and $t = 83.3$ h were shown in Fig. 6-19. Yellow color in Fig. 6-19 represents quartz; blue indicates, clay and black indicates calcite. As CO₂–enriched brine was injected, calcite around the fracture had obvious dissolution, and clay phase had a slight swelling at $t = 83.3$ h. Ca ion concentration was high at the initial time and gradually decreased, which shows the decrease of the dissolution rate. In pure calcite case, we can observe the enlargement of the fracture induced by the calcite dissolution (Fig. 6-20). By applying DBS method, we can obtain the velocity distribution and pressure gradient with time. The dynamic velocity distribution and pressure gradient was influenced by the clay swelling, acid dissolution and structure of unreacted minerals. The normalized porosity and permeability curves of three mineralogical contents were compared in Fig. 6-21. When the system contained clay, the permeability increased slowly as porosity increased. However, pure calcite case had the faster increase of permeability. Although the clay swelling decreased the porosity of the clay phase, the expanded volume of clay inhibited the fluid flow in the system. The obtained porosity and permeability curves have fully considered all the relevant physical–

and–chemical phenomena of calcite dissolution, clay swelling, and subsequent changes of rock morphology and compositions affecting fluid transport. The present model can be used as reference for the large–scale model and modify the Darcy scale model through average parameters over the control volume.

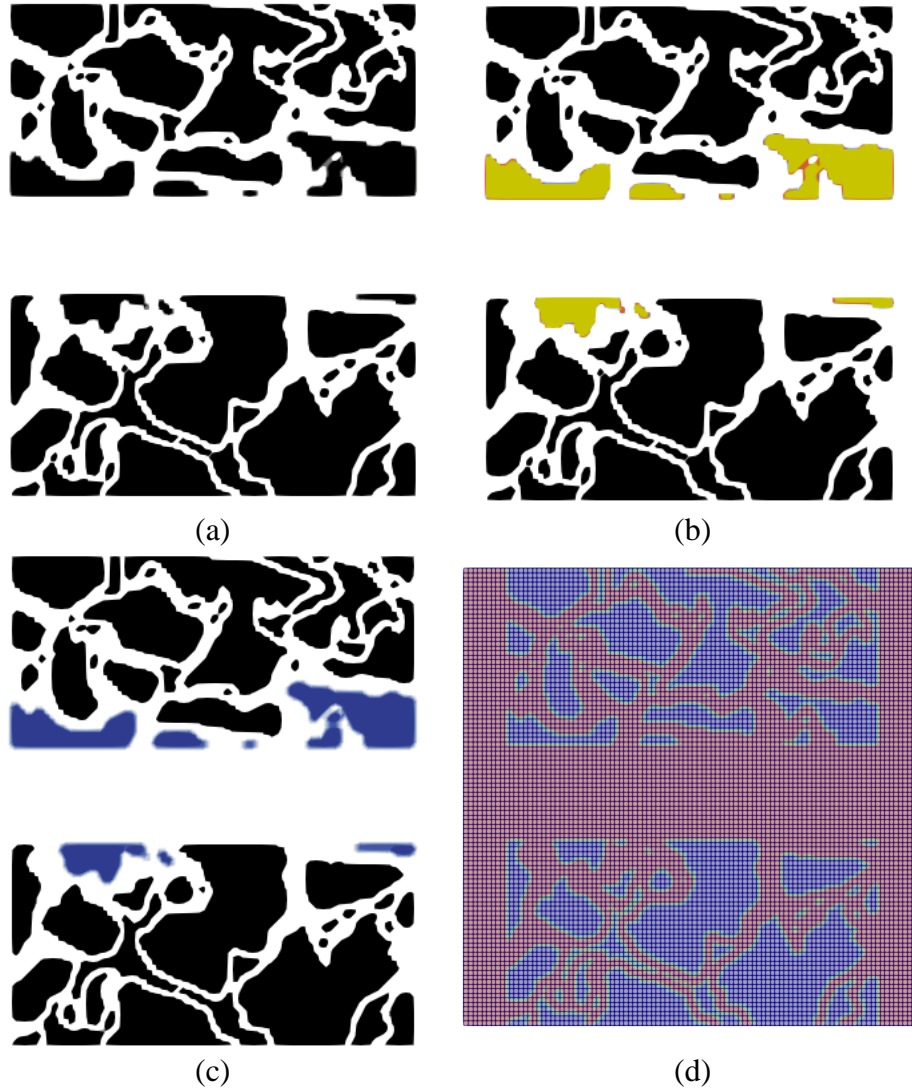


Fig. 6-18 Schematic of fracture–matrix systems (black indicates calcite; yellow indicates quartz; blue indicates clay); (d) The discretization of the computational domain with resolution of 150×150.

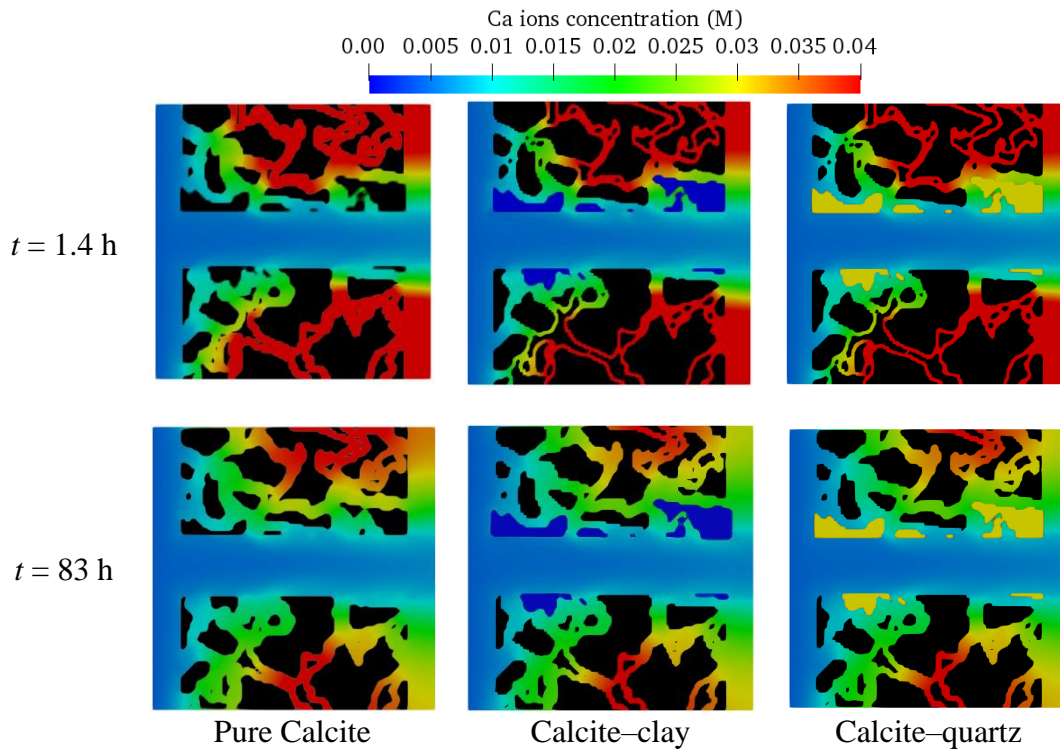


Fig. 6-19 Ca ion concentration of different mineralogical contents.

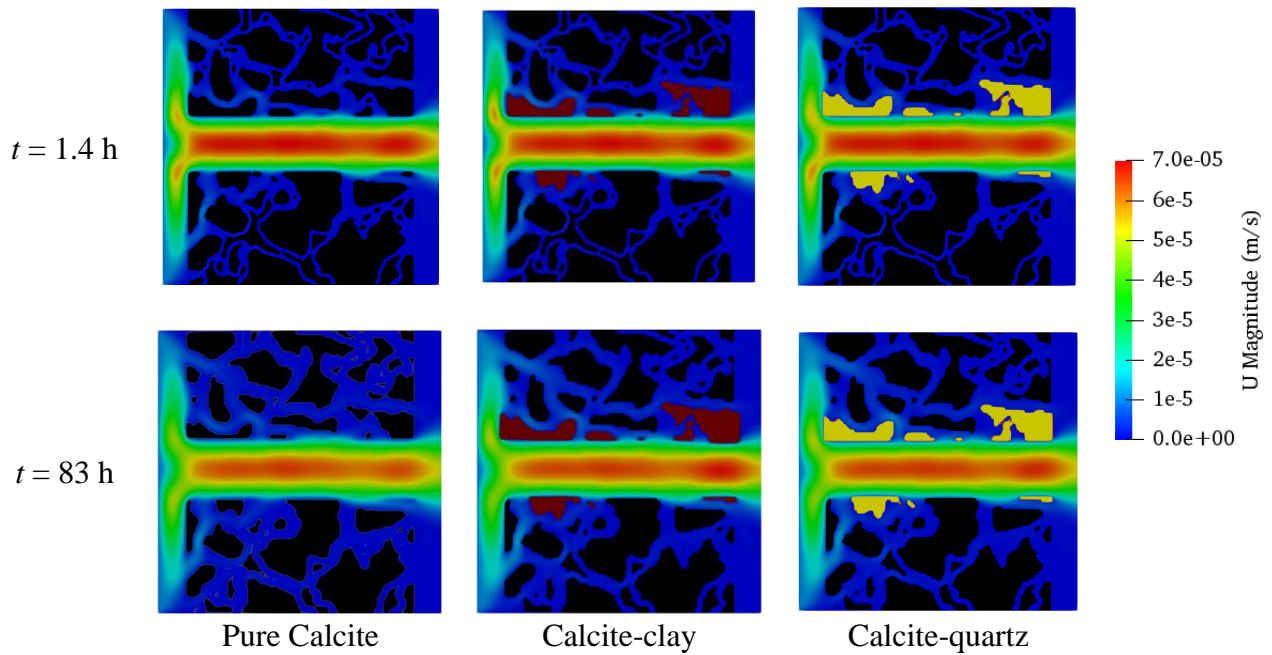


Fig. 6-20 Velocity distribution of different fracture-matrix systems.

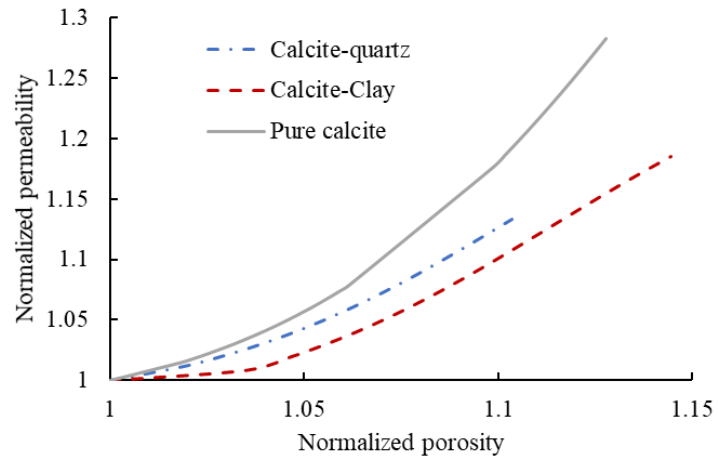


Fig. 6-21 Normalized porosity and permeability curves.

7 INVESTIGATION OF IRON PRECIPITATION BY HYDRAULIC FRACTURING FLUID INJECTION INTO SHALE

7.1 Level-set method coupled with reactive transport model

Level-set method uses the Eulerian computational techniques to capture the moving interface and shapes (Osher, Fedkiw, & Piechor, 2004). In Level-set method, the Level-set filed φ was used to represent the close curvature Γ . In our problem, Level-set filed φ was used to describe the movement of the pyrite surface Γ induced by the chemical reaction. The Level-set filed φ was generated using the equation

$$\varphi_0 = (2\varepsilon_s - 1)\gamma, \quad (7-1)$$

where $\gamma = 0.75\Delta x$, and Δx is the size of mesh cell; ε_s is the volume fraction of solid phase.

After applying the above equation, the Level-set filed has the relation

$$\varphi_0 \begin{cases} > 0 & \text{in solid phase,} \\ = 0 & \text{on the solid - fluid interface } \Gamma, \\ < 0 & \text{in fluid phase.} \end{cases} \quad (7-2)$$

The value of φ_0 in the pyrite area is larger than zero; φ_0 in the fluid area is smaller than zero; φ_0 on the solid-liquid interface is zero. To capture the evolution of the pyrite surface, the evolution of the Level-set filed is given by the time rate of φ

$$\frac{d\varphi}{dt} = \frac{\partial\varphi}{\partial t} + \vec{u} \cdot \nabla\varphi = 0, \quad (7-3)$$

where, \vec{u} is the surface velocity components. After projecting the surface velocity components

onto the local unit normal vector $u_n^\Gamma = \vec{u} \cdot \frac{\nabla\varphi}{|\nabla\varphi|} \Big|_{\varphi=0}$, the above equation can be written into

$$\frac{\partial\varphi}{\partial t} + u_n^\Gamma |\nabla\varphi| = 0, \quad (7-4)$$

where $u_n^\Gamma = \frac{K_c k_r C}{\rho_m}$. ρ_m is the molar density of the solid. Solving the above equation will lead to numerical oscillation due to the advection of φ with time. The Level-set field will not remain the sign function. Thus, we need to re-initialize the Level-set field to the sign-function

$$\frac{\partial \varphi}{\partial \tau} - \text{sign}(\varphi^{t+\Delta t})(1 - |\nabla \varphi|) = 0, \quad (7-5)$$

where τ is artificial time and is calculated by $0.1\Delta x$. The distribution of solid phase and fluid phase was determined by the Smoothed Heaviside function

$$H_\epsilon(\varphi) = \begin{cases} 0 & \text{if } \varphi < -\epsilon, \\ \frac{1}{2} \left[1 + \frac{\varphi}{\epsilon} - \frac{1}{\pi} \sin(\pi\varphi/\epsilon) \right] & \text{if } |\varphi| \leq \epsilon, \\ 1 & \text{if } \varphi > \epsilon, \end{cases} \quad (7-6)$$

where, $\epsilon = 1.5\Delta x$ (Osher et al., 2004). Then, we can obtain the value of volume fraction of solid for each time step. The Level-set was coupled with the reactive transport method introduced in the Chapter 2. The numerical solution sequence is shown in Fig. 7-1. The reactive transport is similar with the processes mentioned in the Chapter 2. For the Level-set method, we first used the Eq.(7-1) to assign the Level-set field from the volume fraction of solid. Next, calculate the Eq. (7-4) to obtain the change of closed surface induced by the chemical reaction. After re-initialize the Level-set field to the sign function, the volume fraction of solid can be updated by the smoothed Heaviside function.

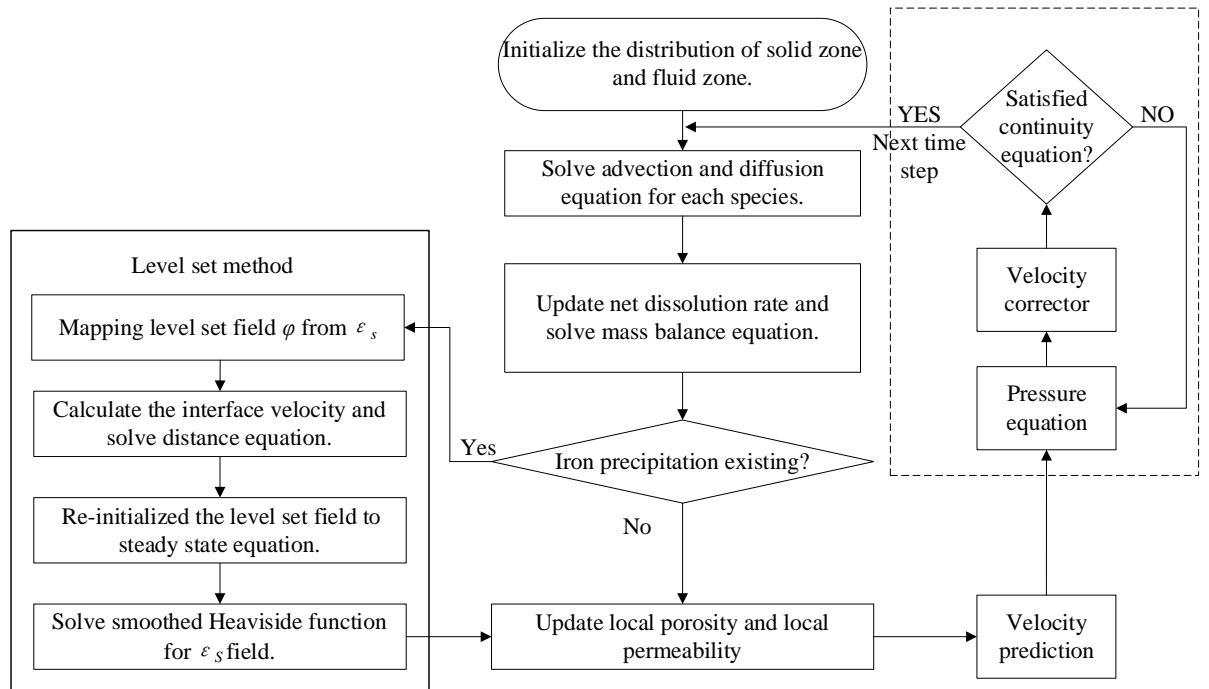
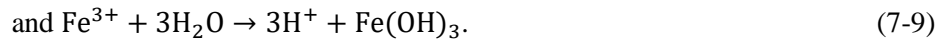
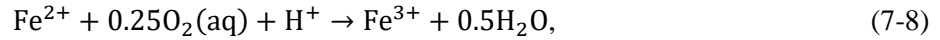
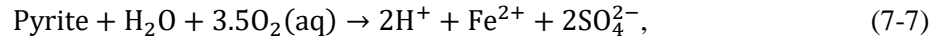


Fig. 7-1 The flow chart of the algorithm coupled Level-set method.

7.2 Chemical reaction paths for the iron precipitation

As the previous study indicated, Fe^{2+} is expected to be fast oxidized into Fe^{3+} , when hydraulic fracturing fluid is injected into shale (Jew et al., 2017). $\text{Fe}(\text{OH})_3$ and other iron oxide will be generated and precipitate on the pyrite surface under the neutral environment. The iron precipitation is influenced by many factors, including the pH value, and existence of organic matters (e.g. bitumen) and oxides in the hydraulic fracturing fluid, where the relevant reaction mechanisms including reaction kinetics have not been totally understood yet. We focused on the Fe^{3+} precipitation on the pyrite surface, because it will critically affect the rock morphologies (by making rough surfaces) and subsequent evolution of fluid flow pathways. Here, dissolved oxygen is playing a significant role in chemical reactions as can be seen below,

and we assumed dissolved oxygen as only component in the water to mimic the hydraulic fracturing fluid in a simplified manner. We mainly considered $\text{Fe}(\text{OH})_3$ as the precipitating mineral in this work, and the chemical reactions for iron precipitation on the pyrite surface are shown as



7.3 Experiments for the validation of numerical modeling

To validate the numerical modeling capability of pyrite surface oxidation and Fe(II) oxidation in solution, we conducted the experiment of the pure pyrite oxidation in the water saturated with oxygen. We first ground the large cubic pyrite into small pieces in the anaerobic environment to prevent the surface oxidation. We used the glove bag to grind the cubic pyrite, which filled with the nitrogen. The pyrite sample was put in the 10 mL vial glass bottle with the rubber stopper. We had two pyrite samples: Sample 1 was 0.0841 g; and Sample 2 was 0.321 g. We put Sample 1 in 10 mL deionized (DI) water. The Sample 2 was put in the 10 mL solution with pH value of 2 diluted with DI water and hydrochloride acid. We used HCl here, because HCl is one of the most common additive as the hydraulic fracturing fluid (Ashena, Aminzadeh, & Khoramchehr, 2022; Jew et al., 2017; N. Li, Chen, Yu, Han, & Kang, 2021). We measured the pyrite weight and oxygen concentration before the experiment. The glass bottle was put in the water bath under 80 °C. The SO_4^{2-} ion was measured using the Aquion Ion Chromatography during the reaction at 0 day, 4 days, 10 days, and 16 days of reaction. The Fe(II) concentration was measured by UV-vis at 4 days and 16 days.

In the ion chromatography analysis, the Dionex AS22–Fast–4 μm analytical column was used to separate the different ions in the solution and measure the conductivity of the ions. NaHCO_3 solution was used to elute the system, and the flow rate was set as 1.2 mL/min. We diluted the calibrated standards as the SO_4^{2-} concentration of 2 mg/L, 4 mg/L, 10 mg/L, 20 mg/L, 50 mg/L and 100 mg/L. After the injection of 0.25 μL solution into the ion chromatography, we could measure the area of the conductivity peak and obtain the calibrated plot of Fig. 7-2(b).

The Fe(II) concentration was measured by Nanodrop 2000 UV–vis Spectrophotometer. The DI water was the blank solution for the UV-vis background calibration. The micropipette was used to get the 1 μL solution for every measurement. We diluted the FeCl_2 standard solution with concentration of 0.006, 0.06, 0.6, and 12 mol/m³ to calibrate the Fe(II). In order to avoid oxidation of FeCl_2 , we dilute the solution in the anaerobic atmosphere. Before added DI water into FeCl_2 , we conducted the gas sparging with nitrogen gas to get rid of the dissolved oxygen in the DI water. We used the DI water without oxygen to dilute the standard solutions. From the UV–vis Spectrophotometer, the FeCl_2 was in the wavelength of 190 nm (Parinayok et al., 2011). The calibration of the FeCl_2 is shown in Fig. 7-2 (b). The x–axis represents the logarithmic value of the solution concentration, and y–axis represents the absorbance of the FeCl_2 . The logarithmic concentration has the linear relationship with the absorbance. We could calculate the Fe(II) concentrations in solution from the absorbance at 190 nm measured from the UV–vis.

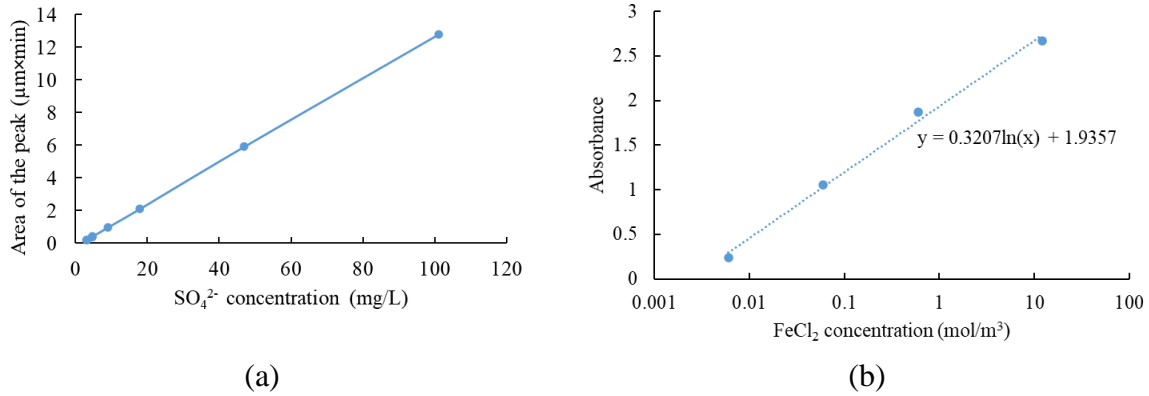


Fig. 7-2 (a) The calibration of sulfate concentration in IC. (b) The standards solution of FeCl₂ and absorbance in UV-vis.

To compare our numerical simulation with the experimental results, we set a 3-D geometric model to replicate the experimental condition. The 3-D model had 0.019 m-length, 0.019 m-width, and 0.027 m-height, as shown in Fig. 7-3 (a). To decrease the computational time spending, we generated the mesh with two sizes. From the bottom to 0.01m in height, we generated the very fine mesh to clearly describe the pyrite shape. As shown in Fig. 7-3 (b), the resolution of this area was 80 (length) × 60 (height) × 80 (width). From 0.01 m to the top of the model, the resolution was 40 (length) × 20 (height) × 40 (width). For the upper area, there was no surface reaction and only solution reaction. Thus, the grid size didn't influence the accuracy of the simulation. In this way, we can significantly decrease the grid number and increase the computational efficiency. The pyrite Sample 1 has the weight of 0.0841 g. The pyrite was initialized as a cubic shape with each side of 0.00256 m, by considering the pyrite density as 5 g/cm³. The Sample 2 was initialized as a cubic shape with each side of 0.004 m. During the experiment, we ground the pyrite sample, and the shape of the sample was irregular. Thus, it was challenging to numerically describe the surface morphology of the pyrite sample. We assumed that the pyrite has the regular cubic shape as shown in Fig. 7-3 (c). To investigate the

impact of surface roughness on the result, we added artificial surface roughness, as shown in Fig. 7-3 (d), which had the same volume as the cubic case. The pH value of solution was set as 7 for the first experiment case with Sample 1, and the O₂ concentration was set as 0.256 mol/m³ for the two experimental cases. The second experiment case was initialized as pH value of 2 at the beginning stage. The temperature was assumed to be 80 °C under the atmospheric pressure. The comparison between the numerical result and the experimental result on the sulfate concentration and Fe(II) concentration was shown in Fig. 7-2. We calibrated the reaction rate constant for chemical reactions of Eqs. (7-7) and (7-8) as 0.356 mol/m²s and 0.00000306 mol/m³s, respectively.

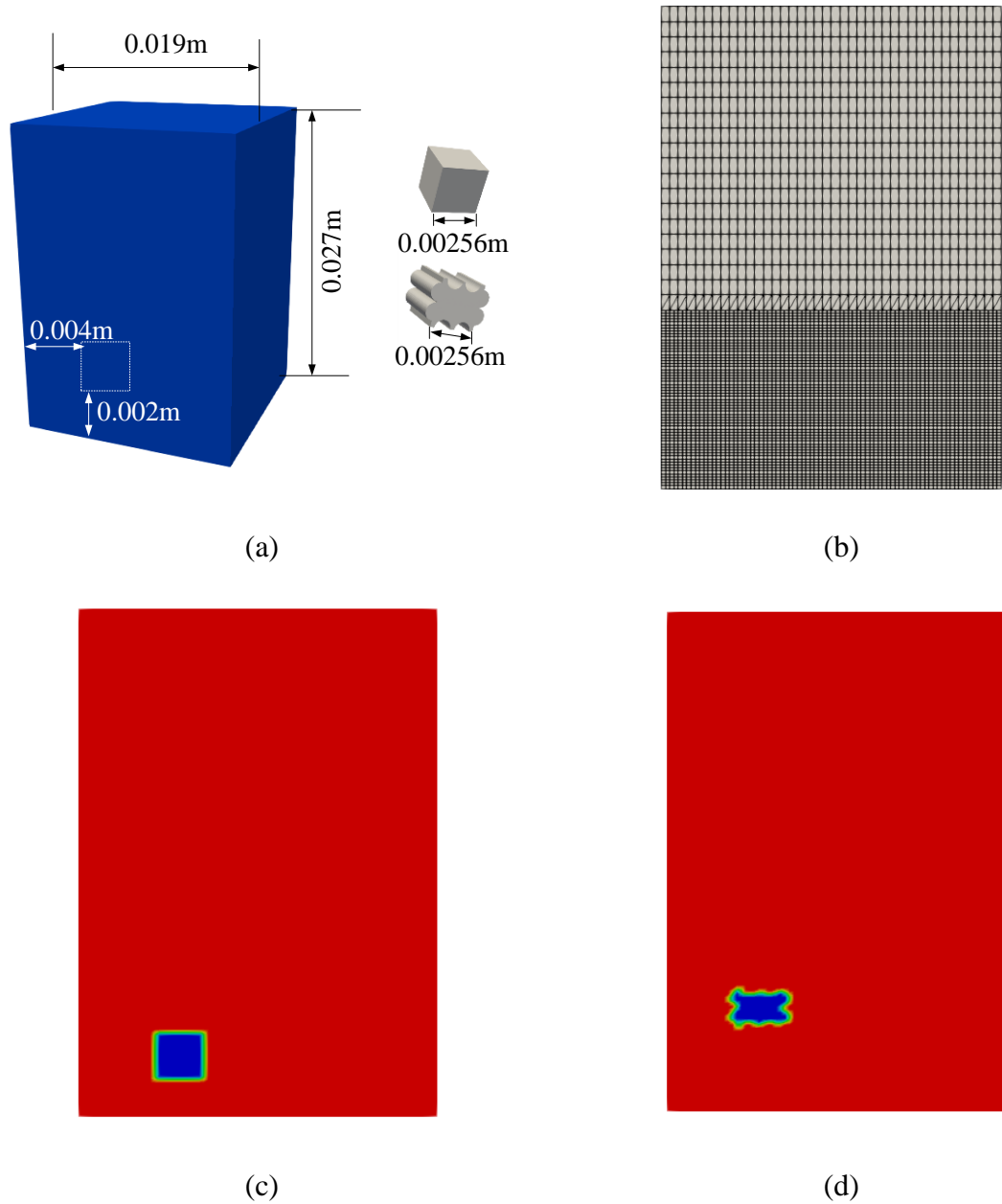


Fig. 7-3 (a) 3-D geometric model to mimic the experiment with Sample 1; (b) The cross section of the mesh; (c) The cross section of the initialization of the solid phase as a cube without surface roughness; (d) The cross section of the initialization of the solid phase with surface roughness.

The comparison between the numerical results and the experimental results are shown in Fig. 7-4. We mimicked the experiment setting for the two pyrite samples. For the Sample 1,

the simulation was under pH=7. Considering the surface roughness, the concentration of sulfate ion was larger than that without surface roughness. The numerical result and experimental result are in accordance with each other. The numerical result showed a minor difference with the experimental result due to following reasons. First, we assumed that the pyrite had the exact cubic shape with smooth surface and couldn't replicate the exact same surface roughness in the numerical model. Second, to measure the SO_4^{2-} ion concentration in the sample solution, we needed to get 0.25 μL solution sample from the vial bottle for the ion chromatography measurement, which might have increased the value of the sulfate ion concentration in the remaining solution.

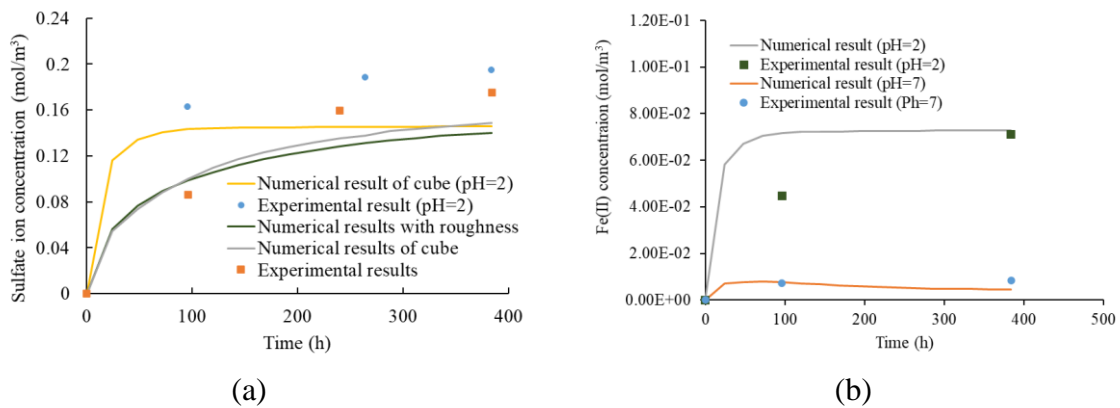


Fig. 7-4 The comparison between experimental results and numerical results of (a) Sulfate ion concentration; (b) Fe(II) concentration.

7.4 Simulation cases using digital rock image models

7.4.1 Problem background

Fig. 7-5 (a) is the Scanning Electron Microscopy (SEM) image of the calcite within the shale matrix from Barnett shale, and Fig. 7-5 (b) is the Energy-dispersive detector (EDS) about the elemental map (Vega, Ross, & Kovalick, 2015). In this EDS image, the red color is quartz

and clay, which were assumed to be non-reactive in this case. The aqua color indicates the calcite. We assumed that the calcite was consumed after the injection of acid. The yellow color is mainly composed with pyrite. The size of the SEM image is about $0.375\text{ mm} \times 0.424\text{ mm}$. According to the above assumptions, we have the geometric model shown in Fig. 7-5 (c), where the red color indicates quartz, and the yellow color indicates pyrite. The initialization of the pyrite and the generation of mesh is shown in Fig. 7-5 (d). The quartz was regarded as unreactive, and there was no dynamic change during the simulation of this case. Thus, we didn't generate the mesh over the quartz area to increase the computational efficiency. The resolution of the grid is 150×170 .

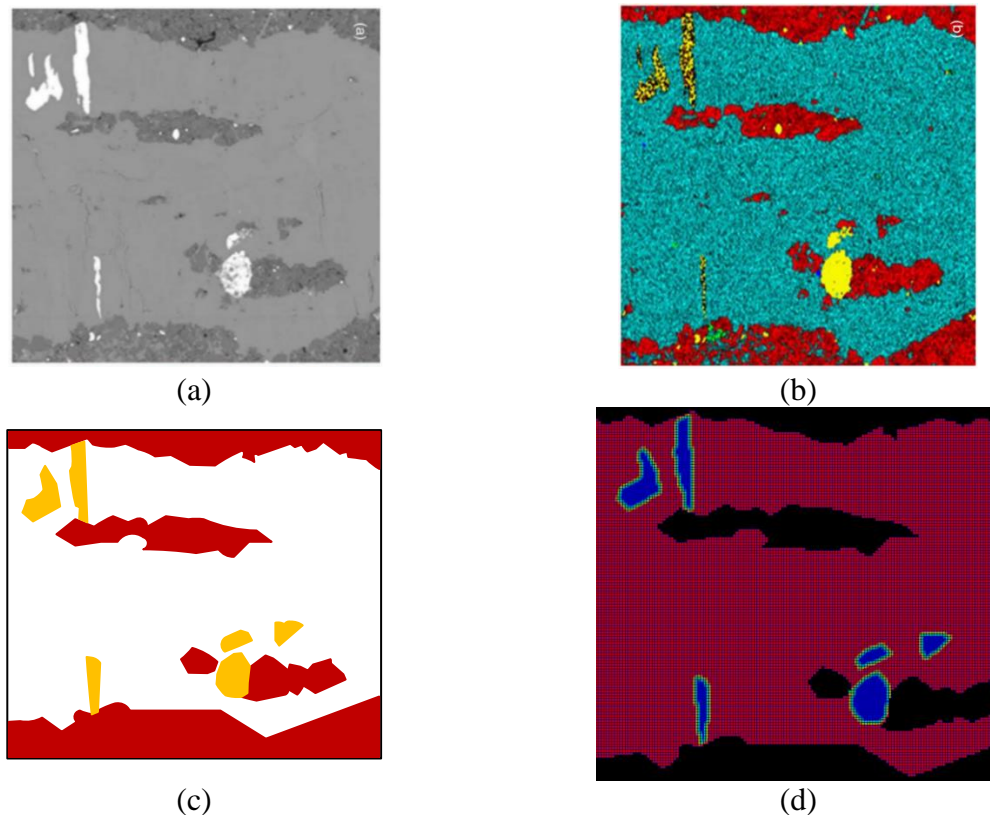


Fig. 7-5 (a) SEM image from Barnett shale (Vega et al., 2015); (b) EDS image of composite elemental map(Vega et al., 2015);(c) Geometric model of the numerical simulation. (d) The initialization of the pyrite in the computational domain with the mesh.

Table 7-1 lists the input parameters for the pyrite oxidation. At the beginning of the simulation, the fluid area was initialized with O₂ concentration of 0.256 mol/m³, and Fe(II), Fe(III), and Fe(III) were initialized as 0 mol/m³. The boundary condition for the species was set as zero gradient ($\frac{\partial c_i}{\partial n} |_{x=0} = 0$). The pH value was initialized as 7 for the fluid area and the concentration of H⁺ on the inlet boundary was 1×10^{-4} mol/m³.

Table 7-1 Input parameter for the pyrite oxidation simulation (Q. Li, Jew, Brown Jr, Bargar, & Maher, 2020).

Parameter	Symbol	Value
Fluid density	ρ_l	920 kg·m ⁻³
Pyrite density	ρ_s	5000 kg·m ⁻³
Fluid viscosity	μ_l	1×10^{-3} Pa·s
Injection velocity	v_{inj}	1.0×10^{-5} m·s ⁻¹
Reaction constant for Eq. (7-7)	k_{rp}	0.356 mol·m ⁻² ·s ⁻¹
Reaction constant for Eq. (7-8)	k_{r-iron}	3.06×10^{-6} mol·m ⁻² ·s ⁻¹
Molecular diffusive coefficient	D_i	5×10^{-9} m ² ·s ⁻¹
Inlet O ₂ concentration	C_{O_2}	0.256 mol·m ⁻³
Equilibrium constant for Eq. (7-7)	Log(Keq)	217
Equilibrium constant for Eq. (7-8)	Log(Keq)	0.938

7.4.2 Simulation of the pyrite surface oxidation and Fe(II) oxidation in solution

This simulation case 1 consists of pyrite surface oxidation and Fe oxidation in the solution. Fig. 7-6 shows the distributions of sulfate, dissolved oxygen, Fe(II), and Fe(III) in the geometric model based on the digital rock image at t = 1,000 s. Sulfate and Fe(II) were mainly generated around the pyrite surface. Fe(III) was from the oxidation of Fe(II). Fe(III) was mainly accumulated at the inlet area. As shown in Fig. 7-6 (d), the inlet area has high concentration of

dissolved oxygen, since we assumed that the oxygen with concentration of 0.256 mol/m^3 was flowed into the computation domain. Most Fe(II) was oxidized into Fe(III) in this area.

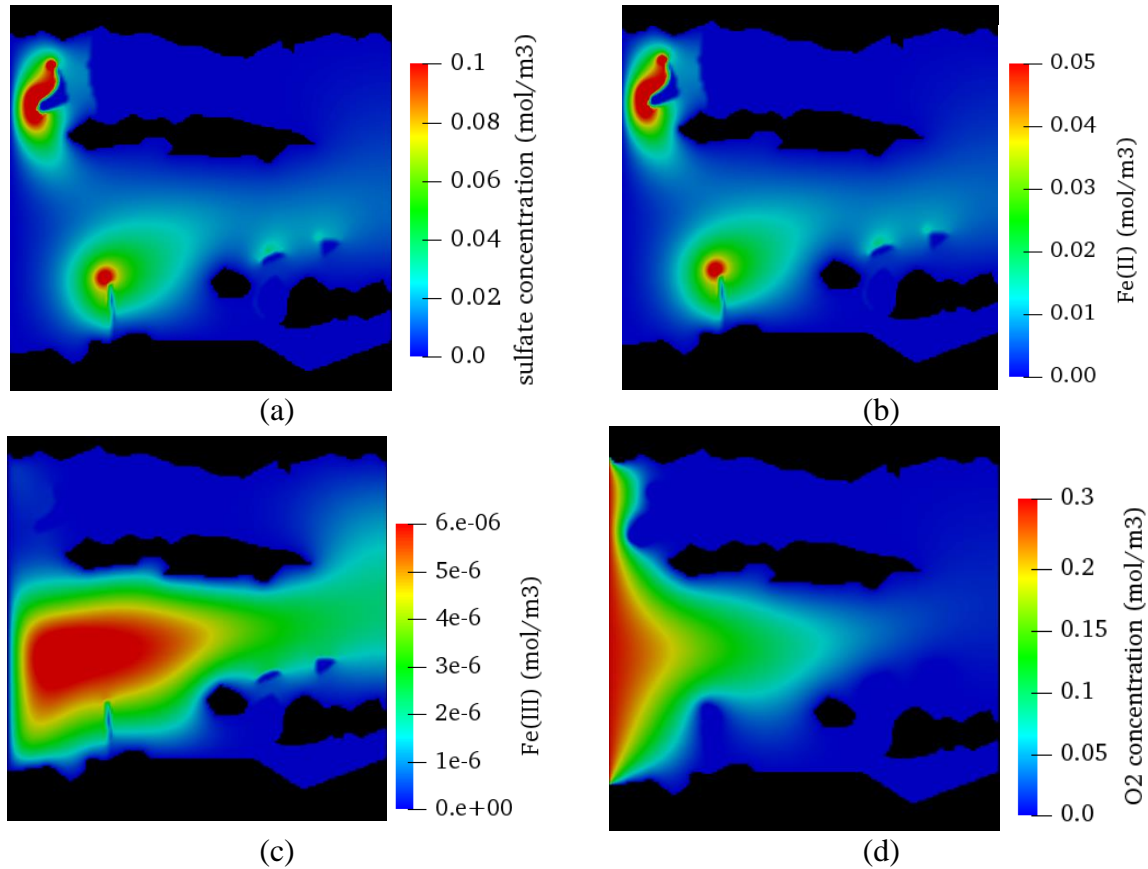


Fig. 7-6 The concentration of ions during the pyrite oxidation at $t = 1,000 \text{ s}$; (a) Sulfate concentration; (b) Fe(II) concentration; (c) Fe(III) concentration; (d) Dissolved oxygen.

The sulfate, Fe(II), Fe(III) and dissolved oxygen concentration were plotted in Fig. 7-7. For sulfate and Fe(II), the concentration first increased fast, and then reached the equilibrium gradually. On the contrary, oxygen concentration decreased at the beginning, and then kept the relatively constant value. Fe(III) increased fast at first, and then decreased gradually due to the iron precipitation.

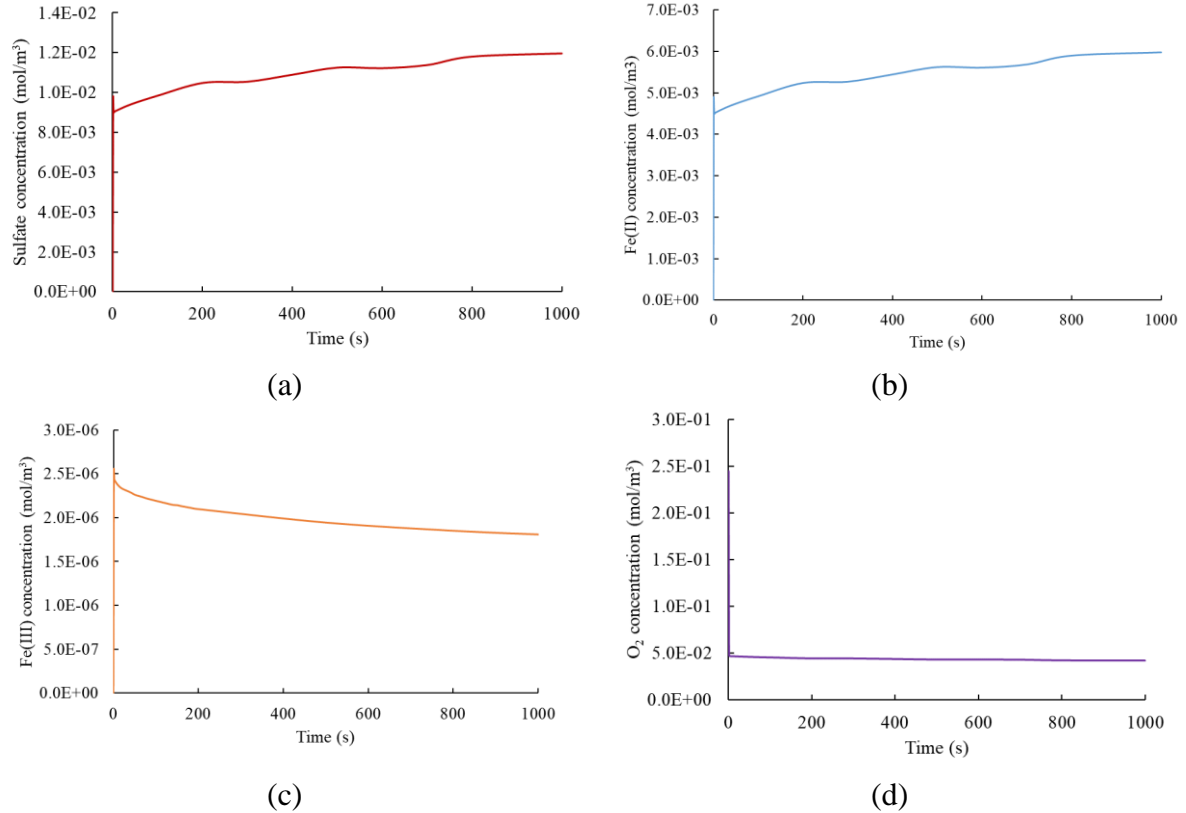


Fig. 7-7 The plot of ions concentration during the pyrite oxidation; (a) Sulfate concentration; (b) Fe(II) concentration; (c) Fe(III) concentration; (d) Dissolved oxygen.

7.4.3 Simulation of the iron precipitation

In the simulation case 2, to investigate the precipitation pattern of the iron, we considered the different values of the second Damköhler numbers (Da_{II}) on the conceptual simulation model on the digital rock image. In this case, we only considered the constant value of the Fe(III) concentration on the inlet boundary as 0.0005 mol/m³. Since there are several factors that can influence the iron precipitation, consideration of the constant inlet Fe(III) concentration can clearly elucidate the mechanism of the precipitation pattern. The volume average effective surface area for this pore structure was about 7000 1/m, and the molar volume

for pyrite was considered as $23.8 \text{ m}^3/\text{mol}$. The Damköhler numbers were set from 10^{-1} to 10^3 , and the parameters are listed in Table 7-2.

Table 7-2 Input parameters for the different cases.

Case	Da_{II}	$k_{precipitation}$	D_i
1	3×10^0	$1 \times 10^{-6} \text{ mol} \cdot \text{m}^{-2} \cdot \text{s}^{-1}$	$1 \times 10^{-9} \text{ m}^2 \cdot \text{s}^{-1}$
2	3.7×10^1	$1 \times 10^{-6} \text{ mol} \cdot \text{m}^{-2} \cdot \text{s}^{-1}$	$7.5 \times 10^{-11} \text{ m}^2 \cdot \text{s}^{-1}$
3	3.5×10^0	$1 \times 10^{-6} \text{ mol} \cdot \text{m}^{-2} \cdot \text{s}^{-1}$	$7.5 \times 10^{-10} \text{ m}^2 \cdot \text{s}^{-1}$
4	3.5×10^{-1}	$1 \times 10^{-8} \text{ mol} \cdot \text{m}^{-2} \cdot \text{s}^{-1}$	$7.5 \times 10^{-11} \text{ m}^2 \cdot \text{s}^{-1}$
5	3.5×10^3	$1 \times 10^{-4} \text{ mol} \cdot \text{m}^{-2} \cdot \text{s}^{-1}$	$7.5 \times 10^{-11} \text{ m}^2 \cdot \text{s}^{-1}$

Fig. 7-8 shows the volume fraction of pore with respect to time during the iron precipitation. From the cases 1 to 4, we selected the simulation times of 1,000 s, 2,000 s, and 3,000 s. For case 5, we selected the times of 200 s, 400 s, and 650 s, due to the fast precipitation rate. We could observe the different precipitation patterns under different Damköhler numbers. Under the small Da_{II} (3.5×10^{-1}), there was barely precipitation on the pyrite surface. When Da_{II} reached 10^3 , the precipitation was more like a dendritic shape, and the precipitation shape was highly random. The cases 1-3 had the same reaction rate constant, but different diffusive coefficients. The growth rate of the precipitation was very similar in these three cases, but the precipitation showed slight differences. By comparing the cases 1 and 2, under the larger Da_{II} with smaller diffusive coefficient, the precipitation had longer dendritic shape. This was mainly influenced by the concentration of Fe(III) in the field, as shown in Fig. 7-9.

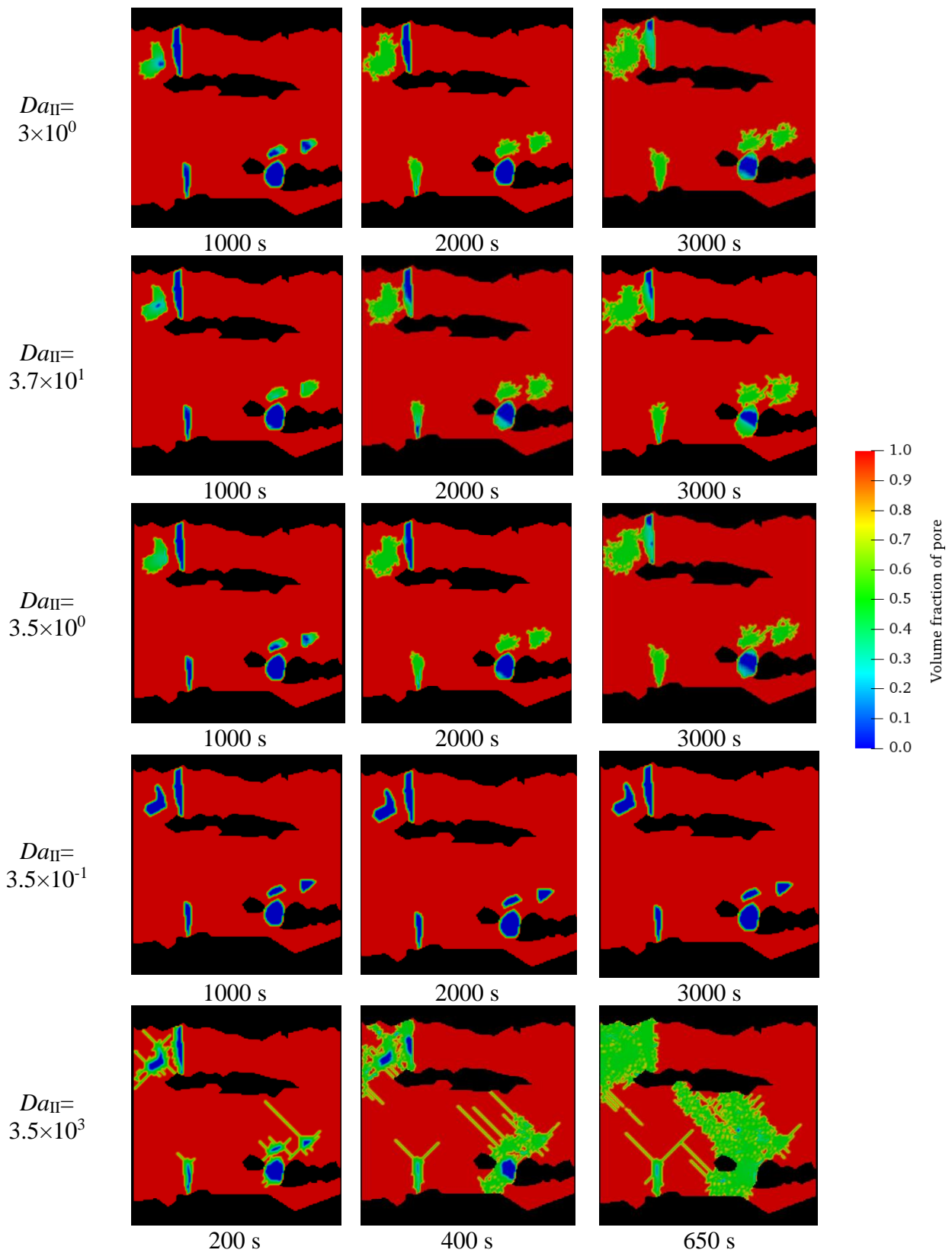


Fig. 7-8 The volume fraction of pore during the iron precipitation.

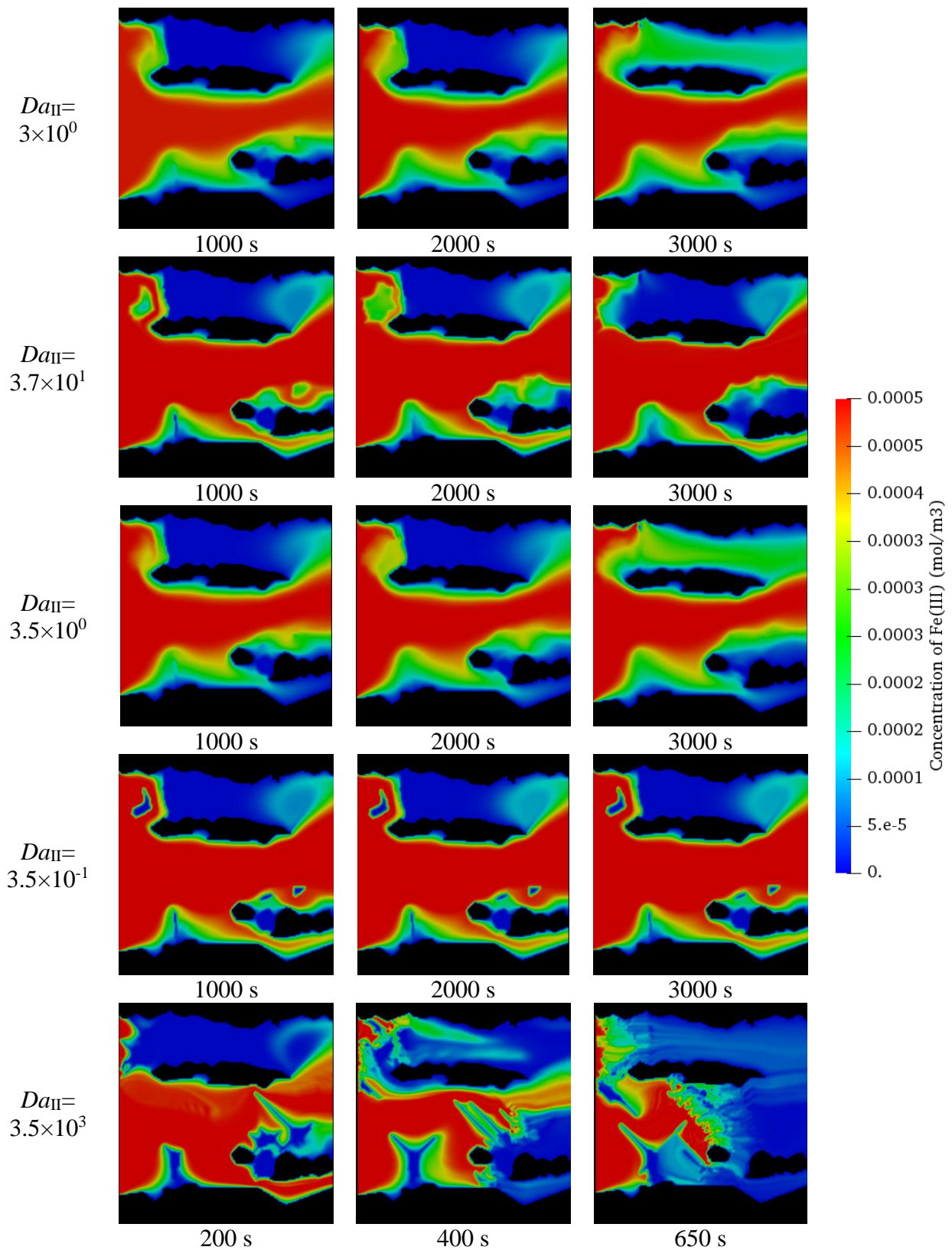


Fig. 7-9 The concentration of Fe(III) during the iron precipitation.

8 SUMMARY

8.1 Conclusions

The subsurface formations as natural shales have rich compositions with carbonate, clay, and sulfide. In such systems, mineral–fluid interactions have critical impact on the fluid transport, as subsequently resulting in the porosity–permeability alteration, pore geometry alteration, and flow pathways evolution. In this regard, the present dissertation established the pore–scale reactive transport models to investigate the impact of mineral–fluid interactions on fluid transport. The present dissertation mainly focuses on three mineral–fluid interactions through the following specific application problems: (1) calcite dissolution by hydrochloric acid (to investigate the carbonate dissolution); (2) CO₂–enriched brine injection (to investigate the carbonate dissolution and clay swelling); (3) hydraulic fracturing fluid injection into shale (to investigate the iron precipitation). We developed the pore–scale reactive transport model to describe the multi–species transport and solid evolution as the result of the chemical reactions.

First, the investigations of carbonate dissolution by hydrochloric acid reveal that:

(1) In the simulation of a digital rock image from Niobrara formation, when $Da_{II} < 1$ and $Pe < 1$, acid deeply penetrated inside the tiny corner and crevice. When $Da_{II} > 1$ and $Pe < 1$, concentration gradient was large. We found that when the Da_{II} and Pe were very close and Da_{II}/Pe ratio was smaller than 1, the pore only showed a slight change. Thus, Da_{II}/Pe ratio needed to be larger than 1 to guarantee the effective acidizing.

(2) To investigate the impact of fracture surface roughness on fluid transport, we first studied the dissolution and transport pattern in the parallel. From the investigation, we categorized the solid dissolution of fractures into three dissolution patterns regarding the second Damköhler number and the Péclet number—face dissolution, front dissolution, and edge

dissolution. We also found that the roughness factor was related to the porosity–permeability curve’s growth rate. As the roughness decreased, the porosity–permeability curve was approximated to the cubic law relationship.

Second, we coupled the momentum conservation equation for a plastic solid to simulate the clay swelling during the injection of CO₂–enriched brine. We also studied the fracture system with various density, length, and connectivity, and the fracture–matrix system during the injection of CO₂–enriched brine. The investigation revealed several interesting findings:

(1) When the system contained clay, the permeability increased slowly as porosity increased due to calcite dissolution, because the expanded clay volume inhibited the fluid flow in the system.

(2) Low fracture density cases have good CO₂ storage capacity, because more calcium was trapped in the dead–end branches and limited the reaction rate at this area.

Third, we conducted the experiment of pyrite oxidation to calibrate the reaction rate constant. This reaction rate constant is utilized to establish the numerical method to track the pyrite surface oxidation and Fe oxidation in solution. With the calibrated reaction rate constant, we conducted the numerical simulation on the digital rock image from Barnett shale and have the following results:

(1) We calibrated the reaction rate constants of pyrite surface oxidation and Fe(II) in solution, and compared the numerical results with the experimental results to validate the numerical method. The sulfate ion and Fe(II) ion from experimental result and experimental result are in the same trend.

(2) From the conceptual model coupling the reactive transport mode and the Level–Set method, we could observe the different precipitation patterns under different Da_{II} .

(3) In the simulation case 1, the concentration of sulfate and Fe(II) ions first increased quickly and then reached the equilibrium gradually. On the contrary, oxygen concentration decreased at the beginning and then kept at the relatively constant value. Fe(III) increased quickly at first, and then decreased gradually due to the iron precipitation.

(4) In the simulation case 2, under the small Da_{II} , there was barely precipitation on the pyrite surface. Under the larger Da_{II} with smaller diffusive coefficient, the precipitation had longer dendritic shape.

8.2 Recommendations for future work

The current work focused on the pore-scale investigation of reactive transport of subsurface water-rock interactions. The envisioned work will include the large-scale (i.e. reservoir, basin) investigation, in order to predict the long-term behavior of the systems. In this regard, first envisioned work will be:

(1) To establish the upscaling method for the porosity-permeability relationship and integrate it into the reservoir-scale study. The obtained upscaling parameters can be used to couple with the large-scale model to track the fate and transport of components for the long term.

Given that the present dissertation only considered the iron hydroxide precipitation on the pyrite surface and that the precipitation mechanisms can vary under different acidic environment, the second and third envisioned works will be:

(2) To establish the experimental method to investigate the various other iron precipitation mechanisms.

(3) To establish the numerical method to predict the iron precipitation as the suspension in the solution.

REFERENCES

- Administration, E. I. (2021). How much shale (tight) oil is produced in the United States?
- Agrawal, P., Raoof, A., Iliev, O., & Wolthers, M. (2020). Evolution of pore-shape and its impact on pore conductivity during CO₂ injection in calcite: Single pore simulations and microfluidic experiments. *Advances in Water Resources*, *136*, 103480. Retrieved from <https://www.sciencedirect.com/science/article/pii/S030917081930644X>. doi:<https://doi.org/10.1016/j.advwatres.2019.103480>
- Akanni, O. O., Nasr-El-Din, H. A., & Gusain, D. (2017). A Computational Navier-Stokes Fluid-Dynamics-Simulation Study of Wormhole Propagation in Carbonate-Matrix Acidizing and Analysis of Factors Influencing the Dissolution Process. *SPE Journal*, *22*(06), 2049-2066. Retrieved from <https://doi.org/10.2118/187962-PA>. doi:10.2118/187962-PA
- Ashena, R., Aminzadeh, F., & Khoramchehr, A. (2022). Production Improvement via Optimization of Hydraulic Acid Fracturing Design Parameters in a Tight Carbonate Reservoir. *Energies*, *15*(5). doi:10.3390/en15051947
- Bazin, B. (2001). From matrix acidizing to acid fracturing: a laboratory evaluation of acid/rock interactions. *SPE Production & Facilities*, *16*(01), 22-29.
- Bear, J., & Buchlin, J.-M. (1991). *Modelling and applications of transport phenomena in porous media* (Vol. 5): Springer.
- Berre, I., Doster, F., & Keilegavlen, E. (2019). Flow in fractured porous media: a review of conceptual models and discretization approaches. *Transport in Porous Media*, *130*(1), 215-236.

- Birkholzer, J. T., Zhou, Q., & Tsang, C.-F. (2009). Large-scale impact of CO₂ storage in deep saline aquifers: A sensitivity study on pressure response in stratified systems. *International Journal of Greenhouse Gas Control*, 3(2), 181-194. Retrieved from <https://www.sciencedirect.com/science/article/pii/S1750583608000753>.
doi:<https://doi.org/10.1016/j.ijggc.2008.08.002>
- Blender Foundation, c. (1994). Blender.
- Blunt, M. J., Bijeljic, B., Dong, H., Gharbi, O., Iglauer, S., Mostaghimi, P., . . . Pentland, C. (2013). Pore-scale imaging and modelling. *Advances in Water Resources*, 51, 197-216.
- Bousquet-Melou, P., Goyeau, B., Quintard, M., Fichot, F., & Gobin, D. (2002). Average momentum equation for interdendritic flow in a solidifying columnar mushy zone. *International Journal of Heat and Mass Transfer*, 45(17), 3651-3665. Retrieved from <https://www.sciencedirect.com/science/article/pii/S0017931002000777>.
doi:[https://doi.org/10.1016/S0017-9310\(02\)00077-7](https://doi.org/10.1016/S0017-9310(02)00077-7)
- Brackbill, J. U., Kothe, D. B., & Zemach, C. (1992). A continuum method for modeling surface tension. *Journal of Computational Physics*, 100(2), 335-354. Retrieved from <https://www.sciencedirect.com/science/article/pii/002199919290240Y>.
doi:[https://doi.org/10.1016/0021-9991\(92\)90240-Y](https://doi.org/10.1016/0021-9991(92)90240-Y)
- Carrillo, F. J., & Bourg, I. C. (2019). A Darcy-Brinkman-Biot Approach to Modeling the Hydrology and Mechanics of Porous Media Containing Macropores and Deformable Microporous Regions. *Water Resources Research*, 55(10), 8096-8121. Retrieved from <https://agupubs.onlinelibrary.wiley.com/doi/abs/10.1029/2019WR024712>.
doi:<https://doi.org/10.1029/2019WR024712>

- Chen, L., Kang, Q., Tang, Q., Robinson, B. A., He, Y.-L., & Tao, W.-Q. (2015). Pore-scale simulation of multicomponent multiphase reactive transport with dissolution and precipitation. *International Journal of Heat and Mass Transfer*, 85, 935-949. doi:10.1016/j.ijheatmasstransfer.2015.02.035
- Chen, L., Kang, Q., Viswanathan, H. S., & Tao, W.-Q. (2014). Pore-scale study of dissolution-induced changes in hydrologic properties of rocks with binary minerals. *Water Resources Research*, 50(12), 9343-9365. Retrieved from <https://agupubs.onlinelibrary.wiley.com/doi/abs/10.1002/2014WR015646>. doi:10.1002/2014wr015646
- Chen, S., Han, Y., Fu, C., Zhang, h., Zhu, Y., & Zuo, Z. (2016). Micro and nano-size pores of clay minerals in shale reservoirs: Implication for the accumulation of shale gas. *Sedimentary Geology*, 342, 180-190. Retrieved from <https://www.sciencedirect.com/science/article/pii/S0037073816301798>. doi:<https://doi.org/10.1016/j.sedgeo.2016.06.022>
- Concil, I. T. R. (2017). Characterization and Remediation of Fractured Rock. *FracRx-1*, Washington, D.C. doi:<https://fracturedrx-1.itrcweb.org/3-hydrology-fluid-flow/>
- Dashtian, H., Bakhshian, S., Hajirezaie, S., Nicot, J.-P., & Hosseini, S. A. (2019). Convection-diffusion-reaction of CO₂-enriched brine in porous media: A pore-scale study. *Computers & Geosciences*, 125, 19-29. Retrieved from <http://www.sciencedirect.com/science/article/pii/S0098300418309348>. doi:<https://doi.org/10.1016/j.cageo.2019.01.009>

- Deng, H., Fitts, J. P., Crandall, D., McIntyre, D., & Peters, C. A. (2015). Alterations of fractures in carbonate rocks by CO₂-acidified brines. *Environmental Science & Technology*, 49(16), 10226-10234.
- Deng, H., Molins, S., Trebotich, D., Steefel, C., & DePaolo, D. (2018). Pore-scale numerical investigation of the impacts of surface roughness: Upscaling of reaction rates in rough fractures. *Geochimica et Cosmochimica Acta*, 239, 374-389.
- Detwiler, R. L., Glass, R. J., & Bourcier, W. L. (2003). Experimental observations of fracture dissolution: The role of Peclet number on evolving aperture variability. *Geophysical research letters*, 30(12). Retrieved from <https://agupubs.onlinelibrary.wiley.com/doi/abs/10.1029/2003GL017396>. doi:10.1029/2003gl017396
- Dijk, P. E., Berkowitz, B., & Yechieli, Y. (2002). Measurement and analysis of dissolution patterns in rock fractures. *Water Resources Research*, 38(2), 5-1-5-12.
- Duarte, F., Gormaz, R., & Natesan, S. (2004). Arbitrary Lagrangian–Eulerian method for Navier–Stokes equations with moving boundaries. *Computer Methods in Applied Mechanics and Engineering*, 193(45-47), 4819-4836.
- Er, V., Babadagli, T., & Xu, Z. (2010). Pore-scale investigation of the matrix– fracture interaction during CO₂ injection in naturally fractured oil reservoirs. *Energy & Fuels*, 24(2), 1421-1430.
- Fazeli, H., Patel, R., & Hellevang, H. (2018). Effect of Pore-Scale Mineral Spatial Heterogeneity on Chemically Induced Alterations of Fractured Rock: A Lattice Boltzmann Study. *Geofluids*, 2018, 6046182. Retrieved from <https://doi.org/10.1155/2018/6046182>. doi:10.1155/2018/6046182

- Feng, W., He, B., Song, A., Wang, Y., Zhang, M., & Zhang, W. (2010, 2010//). *Compressible Lattice Boltzmann Method and Applications*. Paper presented at the High Performance Computing and Applications, Berlin, Heidelberg.
- Ferrari, A., & Lunati, I. (2013). Direct numerical simulations of interface dynamics to link capillary pressure and total surface energy. *Advances in Water Resources*, *57*, 19-31.
- Fogler, H. S., Lund, K., & McCune, C. C. (1976). Predicting the Flow and Reaction of HCl/HF Acid Mixtures in Porous Sandstone Cores. *Society of Petroleum Engineers Journal*, *16*(05), 248-260. Retrieved from <https://doi.org/10.2118/5646-PA>.
doi:10.2118/5646-PA
- Fredd, C. N., & Fogler, H. S. (1998). Influence of transport and reaction on wormhole formation in porous media. *AIChE Journal*, *44*(9), 1933-1949.
- Golfier, F., Zarcone, C., Bazin, B., Lenormand, R., Lasseux, D., & Quintard, M. (2002). On the ability of a Darcy-scale model to capture wormhole formation during the dissolution of a porous medium. *Journal of Fluid Mechanics*, *457*, 213-254.
doi:10.1017/s0022112002007735
- Gray, W. G. (1975). A derivation of the equations for multi-phase transport. *Chemical Engineering Science*, *30*(2), 229-233. Retrieved from <https://www.sciencedirect.com/science/article/pii/0009250975800108>.
doi:[https://doi.org/10.1016/0009-2509\(75\)80010-8](https://doi.org/10.1016/0009-2509(75)80010-8)
- Guo, J., Laouafa, F., & Quintard, M. (2016). A theoretical and numerical framework for modeling gypsum cavity dissolution. *International Journal for Numerical and Analytical Methods in Geomechanics*, *40*(12), 1662-1689. doi:10.1002/nag.2504

- Hoefner, M., & Fogler, H. S. (1988). Pore evolution and channel formation during flow and reaction in porous media. *AIChE Journal*, 34(1), 45-54.
- Huang, H., Meakin, P., & Liu, M. (2005). Computer simulation of two - phase immiscible fluid motion in unsaturated complex fractures using a volume of fluid method. *Water Resources Research*, 41(12).
- Huang, T., Hill, A. D., & Schechter, R. S. (1997). *Reaction Rate and Fluid Loss: The Keys to Wormhole Initiation and Propagation in Carbonate Acidizing*. Paper presented at the International Symposium on Oilfield Chemistry, Houston, Texas.
<https://doi.org/10.2118/37312-MS>
- Hung, K. M., Hill, A. D., & Sepehrnoori, K. (1989). A Mechanistic Model of Wormhole Growth in Carbonate Matrix Acidizing and Acid Fracturing. *Journal of Petroleum Technology*, 41(01), 59-66. Retrieved from <https://doi.org/10.2118/16886-PA>.
doi:10.2118/16886-PA
- Jasak, H. (1996). Error Analysis and Estimation for Finite Volume Method with Applications to Fluid Flow. *PhD thesis*.
- Jew, A. D., Dustin, M. K., Harrison, A. L., Joe-Wong, C. M., Thomas, D. L., Maher, K., . . . Bargar, J. R. (2017). Impact of organics and carbonates on the oxidation and precipitation of iron during hydraulic fracturing of shale. *Energy & Fuels*, 31(4), 3643-3658.
- Kang, Q., Chen, L., Valocchi, A. J., & Viswanathan, H. S. (2014). Pore-scale study of dissolution-induced changes in permeability and porosity of porous media. *Journal of Hydrology*, 517, 1049-1055. doi:10.1016/j.jhydrol.2014.06.045

- Kang, Q., Zhang, D., & Chen, S. (2003). Simulation of dissolution and precipitation in porous media. *Journal of Geophysical Research: Solid Earth*, 108(B10).
doi:10.1029/2003jb002504
- Kang, Q., Zhang, D., Chen, S., & He, X. (2002). Lattice Boltzmann simulation of chemical dissolution in porous media. *Physical Review E*, 65(3), 036318. Retrieved from <https://link.aps.org/doi/10.1103/PhysRevE.65.036318>.
doi:10.1103/PhysRevE.65.036318
- Kim, T., Hwang, S., & Jang, S. (2016). Petrophysical approach for estimating porosity, clay volume, and water saturation in gas-bearing shale: A case study from the Horn River Basin, Canada. *Austrian Journal of Earth Sciences*, 109. doi:10.17738/ajes.2016.0022
- Leaist, D. G. (1984). Diffusion in aqueous solutions of sulfuric acid. *Canadian journal of chemistry*, 62(9), 1692-1697.
- Leal, L. G. (1992). *Laminar flow and convective transport processes* (Vol. 251): Elsevier.
- Li, N., Chen, F., Yu, J., Han, P., & Kang, J. (2021). Pre-acid system for improving the hydraulic fracturing effect in low-permeability tight gas reservoir. *Journal of Petroleum Exploration and Production*, 11(4), 1761-1780. Retrieved from <https://doi.org/10.1007/s13202-021-01129-x>. doi:10.1007/s13202-021-01129-x
- Li, Q., Jew, A. D., Brown Jr, G. E., Bargar, J. R., & Maher, K. (2020). Reactive transport modeling of shale–fluid interactions after imbibition of fracturing fluids. *Energy & Fuels*, 34(5), 5511-5523.
- Li, Q., Jew, A. D., Cercone, D., Bargar, J. R., Brown Jr, G. E., & Maher, K. (2019). *Geochemical Modeling of Iron (Hydr) oxide Scale Formation During Hydraulic*

Fracturing Operations. Paper presented at the Unconventional Resources Technology Conference, Denver, Colorado, 22-24 July 2019.

- Li, Q., Jew, A. D., Kohli, A., Maher, K., Brown Jr, G. E., & Bargar, J. R. (2019). Thicknesses of chemically altered zones in shale matrices resulting from interactions with hydraulic fracturing fluid. *Energy & Fuels*, 33(8), 6878-6889.
- Li, X., Huang, H., & Meakin, P. (2008). Level set simulation of coupled advection-diffusion and pore structure evolution due to mineral precipitation in porous media. *Water Resources Research*, 44(12). doi:10.1029/2007wr006742
- Liu, H., Valocchi, A. J., Werth, C., Kang, Q., & Oostrom, M. (2014). Pore-scale simulation of liquid CO₂ displacement of water using a two-phase lattice Boltzmann model. *Advances in Water Resources*, 73, 144-158.
- Liu, L. (2013). Prediction of swelling pressures of different types of bentonite in dilute solutions. *Colloids and Surfaces A: Physicochemical and Engineering Aspects*, 434, 303-318. Retrieved from <https://www.sciencedirect.com/science/article/pii/S0927775713004585>.
doi:<https://doi.org/10.1016/j.colsurfa.2013.05.068>
- Liu, M., & Mostaghimi, P. (2017a). Characterisation of reactive transport in pore-scale correlated porous media. *Chemical Engineering Science*, 173, 121-130.
doi:10.1016/j.ces.2017.06.044
- Liu, M., & Mostaghimi, P. (2017b). High-resolution pore-scale simulation of dissolution in porous media. *Chemical Engineering Science*, 161, 360-369.
doi:10.1016/j.ces.2016.12.064

- Lund, K., Fogler, H. S., & McCune, C. C. (1973). Acidization—I. The dissolution of dolomite in hydrochloric acid. *Chemical Engineering Science*, 28(3), 691-IN691. Retrieved from <http://www.sciencedirect.com/science/article/pii/0009250977800031>. doi:[https://doi.org/10.1016/0009-2509\(77\)80003-1](https://doi.org/10.1016/0009-2509(77)80003-1)
- Lund, K., Fogler, H. S., McCune, C. C., & Ault, J. W. (1975). Acidization—II. The dissolution of calcite in hydrochloric acid. *Chemical Engineering Science*, 30(8), 825-835. Retrieved from <http://www.sciencedirect.com/science/article/pii/0009250975800479>. doi:[https://doi.org/10.1016/0009-2509\(75\)80047-9](https://doi.org/10.1016/0009-2509(75)80047-9)
- Luo, H., Quintard, M., Debenest, G., & Laouafa, F. (2012). Properties of a diffuse interface model based on a porous medium theory for solid–liquid dissolution problems. *Computational Geosciences*, 16(4), 913-932. doi:10.1007/s10596-012-9295-1
- Michael, H. A., & Khan, M. R. (2016). Impacts of physical and chemical aquifer heterogeneity on basin-scale solute transport: Vulnerability of deep groundwater to arsenic contamination in Bangladesh. *Advances in Water Resources*, 98, 147-158.
- Mittal, R., & Iaccarino, G. (2005). Immersed boundary methods. *Annu. Rev. Fluid Mech.*, 37, 239-261.
- Molins, S., Soulaire, C., Prasianakis, N. I., Abbasi, A., Poncet, P., Ladd, A. J. C., . . . Steefel, C. I. (2020). Simulation of mineral dissolution at the pore scale with evolving fluid–solid interfaces: review of approaches and benchmark problem set. *Computational Geosciences*. Retrieved from <https://doi.org/10.1007/s10596-019-09903-x>. doi:10.1007/s10596-019-09903-x

- Molins, S., Trebotich, D., Miller, G. H., & Steefel, C. I. (2017). Mineralogical and transport controls on the evolution of porous media texture using direct numerical simulation. *Water Resources Research*, 53(5), 3645-3661. Retrieved from <https://agupubs.onlinelibrary.wiley.com/doi/abs/10.1002/2016WR020323>.
doi:10.1002/2016wr020323
- Molins, S., Trebotich, D., Steefel, C. I., & Shen, C. (2012). An investigation of the effect of pore scale flow on average geochemical reaction rates using direct numerical simulation. *Water Resources Research*, 48(3).
- Ni, X., Chen, W., Li, Z., & Gao, X. (2017). Reconstruction of different scales of pore-fractures network of coal reservoir and its permeability prediction with Monte Carlo method. *International Journal of Mining Science and Technology*, 27(4), 693-699. Retrieved from <https://www.sciencedirect.com/science/article/pii/S2095268617303592>.
doi:<https://doi.org/10.1016/j.ijmst.2017.05.021>
- Ning, Y., Zhang, K., He, S., Chen, T., Wang, H., & Qin, G. (2019). Numerical modeling of gas transport in shales to estimate rock and fluid properties based on multiscale digital rocks. *Energy Procedia*, 158, 6093-6098.
- Osher, S., Fedkiw, R., & Piechor, K. (2004). Level set methods and dynamic implicit surfaces. *Appl. Mech. Rev.*, 57(3), B15-B15.
- Parinayok, P., Yamashita, M., Yonezu, K., Ohashi, H., Watanabe, K., Okaue, Y., & Yokoyama, T. (2011). Interaction of Au (III) and Pt (IV) complex ions with Fe (II) ions as a scavenging and a reducing agent: A basic study on the recovery of Au and Pt by a chemical method. *Journal of colloid and interface science*, 364(1), 272-275.

- Pereira Nunes, J., Blunt, M., & Bijeljic, B. (2016). Pore - scale simulation of carbonate dissolution in micro - CT images. *Journal of Geophysical Research: Solid Earth*, 121(2), 558-576.
- Peters, C. a. K., Julie. (2020). *Eagle Ford Shale: Synchrotron-Based Element and Mineral Maps*.
- Pokrovsky, O. S., Golubev, S. V., & Schott, J. (2005). Dissolution kinetics of calcite, dolomite and magnesite at 25 °C and 0 to 50 atm pCO₂. *Chemical Geology*, 217(3), 239-255. Retrieved from <https://www.sciencedirect.com/science/article/pii/S000925410500015X>.
doi:<https://doi.org/10.1016/j.chemgeo.2004.12.012>
- Pokrovsky, O. S., Golubev, S. V., Schott, J., & Castillo, A. (2009). Calcite, dolomite and magnesite dissolution kinetics in aqueous solutions at acid to circumneutral pH, 25 to 150 °C and 1 to 55 atm pCO₂: New constraints on CO₂ sequestration in sedimentary basins. *Chemical Geology*, 265(1), 20-32. Retrieved from <https://www.sciencedirect.com/science/article/pii/S0009254109000308>.
doi:<https://doi.org/10.1016/j.chemgeo.2009.01.013>
- Prodanovic, M. a. L., Christopher and Tokan-Lawal, Adenike and Eichhubl, Peter. (2016). Niobrara formation fracture.
- Quintard, M. (2015). Introduction to heat and mass transport in porous media. *Porous Media Interaction with High Temperature and High Speed Flows, Von Karman Institute for Fluid Dynamics, Rhode Saint Genese, Belgium*.
- Quintard, M., & Whitaker, S. (1993). Transport in ordered and disordered porous media: volume-averaged equations, closure problems, and comparison with experiment.

Chemical Engineering Science, 48(14), 2537-2564. Retrieved from
<https://www.sciencedirect.com/science/article/pii/000925099380266S>.

doi:[https://doi.org/10.1016/0009-2509\(93\)80266-S](https://doi.org/10.1016/0009-2509(93)80266-S)

Quintard, M., & Whitaker, S. (1994). Transport in ordered and disordered porous media III: Closure and comparison between theory and experiment. *Transport in Porous Media*, 15, 31-49. doi:10.1007/BF01046157

Raeini, A. Q., Bijeljic, B., & Blunt, M. J. (2014). Numerical modelling of sub-pore scale events in two-phase flow through porous media. *Transport in Porous Media*, 101(2), 191-213.

Sadeghnejad, S., Enzmann, F., & Kersten, M. (2021). Digital rock physics, chemistry, and biology: challenges and prospects of pore-scale modelling approach. *Applied Geochemistry*, 131, 105028. Retrieved from
<https://www.sciencedirect.com/science/article/pii/S0883292721001608>.
doi:<https://doi.org/10.1016/j.apgeochem.2021.105028>

Schechter, R. S., & Gidley, J. L. (1969). The change in pore size distribution from surface reactions in porous media. *AIChE Journal*, 15(3), 339-350. Retrieved from
<https://doi.org/10.1002/aic.690150309>. doi:<https://doi.org/10.1002/aic.690150309>

Shovkun, I., & Espinoza, D. N. (2019). Fracture propagation in heterogeneous porous media: pore-scale implications of mineral dissolution. *Rock Mechanics and Rock Engineering*, 52(9), 3197-3211.

Singh, H., & Cai, J. (2019). A feature-based stochastic permeability of shale: part 1— validation and two-phase permeability in a Utica shale sample. *Transport in Porous Media*, 126(3), 527-560.

- Soulaine, C., Roman, S., Kavscek, A., & Tchelepi, H. A. (2017). Mineral dissolution and wormholing from a pore-scale perspective. *Journal of Fluid Mechanics*, 827, 457-483. Retrieved from <https://www.cambridge.org/core/article/mineral-dissolution-and-wormholing-from-a-porescale-perspective/82CE22EF080CA51DF1C2BEECA4C582DD>. doi:10.1017/jfm.2017.499
- Soulaine, C., Roman, S., Kavscek, A., & Tchelepi, H. A. (2018). Pore-scale modelling of multiphase reactive flow: application to mineral dissolution with production of CO_2 . *Journal of Fluid Mechanics*, 855, 616-645. Retrieved from <https://www.cambridge.org/core/article/porescale-modelling-of-multiphase-reactive-flow-application-to-mineral-dissolution-with-production-of-textco2/A4CBC57A04C43066D273BB0E44E3A305>. doi:10.1017/jfm.2018.655
- Soulaine, C., & Tchelepi, H. A. (2016). Micro-continuum Approach for Pore-Scale Simulation of Subsurface Processes. *Transport in Porous Media*, 113(3), 431-456. doi:10.1007/s11242-016-0701-3
- Spearman, J. (2017). An examination of the rheology of flocculated clay suspensions. *Ocean Dynamics*, 67(3-4), 485-497.
- Spencer, M., Garlapalli, R., & Trembly, J. P. (2020). Geochemical phenomena between Utica-Point Pleasant shale and hydraulic fracturing fluid. *AIChE Journal*, 66(4), e16887. Retrieved from <https://doi.org/10.1002/aic.16887>. doi:<https://doi.org/10.1002/aic.16887>
- Starchenko, V., & Ladd, A. J. C. (2018). The Development of Wormholes in Laboratory-Scale Fractures: Perspectives From Three-Dimensional Simulations. *Water Resources*

- Research*, 54(10), 7946-7959. Retrieved from <https://doi.org/10.1029/2018WR022948>. doi:<https://doi.org/10.1029/2018WR022948>
- Tartakovsky, A. M., Meakin, P., Scheibe, T. D., & West, R. M. E. (2007). Simulations of reactive transport and precipitation with smoothed particle hydrodynamics. *Journal of Computational Physics*, 222(2), 654-672.
- Tian, Z., Xing, H., Tan, Y., Gu, S., & Golding, S. D. (2016). Reactive transport LBM model for CO₂ injection in fractured reservoirs. *Computers & Geosciences*, 86, 15-22.
- Tokan-Lawal, A., Prodanović, M., Landry, C. J., & Eichhubl, P. (2017). Influence of Numerical Cementation on Multiphase Displacement in Rough Fractures. *Transport in Porous Media*, 116(1), 275-293. Retrieved from <https://doi.org/10.1007/s11242-016-0773-0>. doi:10.1007/s11242-016-0773-0
- Vallejo, L. E., & Mawby, R. (2000). Porosity influence on the shear strength of granular material–clay mixtures. *Engineering Geology*, 58(2), 125-136. Retrieved from <https://www.sciencedirect.com/science/article/pii/S001379520000051X>. doi:[https://doi.org/10.1016/S0013-7952\(00\)00051-X](https://doi.org/10.1016/S0013-7952(00)00051-X)
- Vega, B., Ross, C. M., & Kovscek, A. R. (2015). Imaging-Based Characterization of Calcite-Filled Fractures and Porosity in Shales. *SPE Journal*, 20(04), 810-823. Retrieved from <https://doi.org/10.2118/2014-1922521-PA>. doi:10.2118/2014-1922521-pa
- Verhaeghe, F., Arnout, S., Blanpain, B., & Wollants, P. (2006). Lattice-Boltzmann modeling of dissolution phenomena. *Physical Review E*, 73(3), 036316.
- Weller, H. G., Tabor, G., Jasak, H., & Fureby, C. (1998). A tensorial approach to computational continuum mechanics using object-oriented techniques. *Computers in physics*, 12(6), 620-631.

- Xu, T., Apps, J. A., & Pruess, K. (2003). Reactive geochemical transport simulation to study mineral trapping for CO₂ disposal in deep arenaceous formations. *Journal of Geophysical Research: Solid Earth*, 108(B2).
- Xu, Z., Meakin, P., & Tartakovsky, A. M. (2009). Diffuse-interface model for smoothed particle hydrodynamics. *Physical Review E*, 79(3), 036702.
- You, J., & Lee, K. J. (2021a). Analyzing the Dynamics of Mineral Dissolution during Acid Fracturing by Pore-Scale Modeling of Acid-Rock Interaction. *SPE Journal*, 1-14. Retrieved from <https://doi.org/10.2118/200406-PA>. doi:10.2118/200406-pa
- You, J., & Lee, K. J. (2021b). Pore-Scale Study to Analyze the Impacts of Porous Media Heterogeneity on Mineral Dissolution and Acid Transport Using Darcy–Brinkmann–Stokes Method. *Transport in Porous Media*. Retrieved from <https://doi.org/10.1007/s11242-021-01577-3>. doi:10.1007/s11242-021-01577-3
- You, J., & Lee, K. J. (2021c). A pore–scale investigation of surface roughness on the evolution of natural fractures during acid dissolution using DBS method. *Journal of Petroleum Science and Engineering*, 108728. Retrieved from <https://www.sciencedirect.com/science/article/pii/S0920410521003880>. doi:<https://doi.org/10.1016/j.petrol.2021.108728>
- You, J., & Lee, K. J. (2022). Pore-Scale Numerical Investigations of the Impact of Mineral Dissolution and Transport on the Heterogeneity of Fracture Systems During CO₂-Enriched Brine Injection. *SPE Journal*, 1-17. Retrieved from <https://doi.org/10.2118/204313-PA>. doi:10.2118/204313-pa

APPENDIX

A1. Notation of the volume-averaged technique

When use the following phase indicator to represent the phase volume fractions

$$\gamma_f = \begin{cases} 1 & \text{in } f \text{ - phase,} \\ 0 & \text{in } s \text{ - phase,} \end{cases} \quad (\text{A. 1})$$

which gives the following equation to simplify the phase volume fraction:

$$\varepsilon_f = \langle \gamma_f \rangle = \frac{1}{V} \int_{V_f} dV = \frac{V_f}{V}. \quad (\text{A. 2})$$

By applying the general transport theorems and mathematical development, we gave the following equations regarding the average of phase property (Quintard & Whitaker, 1993)

$$\langle \nabla \psi_f \rangle = \nabla \langle \psi_f \rangle + \frac{1}{V} \int_{A_{fs}} \mathbf{n}_{fs} \psi_f dA, \quad (\text{A. 3})$$

$$\langle \nabla \cdot \mathbf{A}_f \rangle = \nabla \cdot \langle \mathbf{A}_f \rangle + \frac{1}{V} \int_{A_{fs}} \mathbf{n}_{fs} \cdot \mathbf{A}_f dA, \quad (\text{A. 4})$$

$$\text{and } \left\langle \frac{\partial \psi_f}{\partial t} \right\rangle = \frac{\partial \langle \psi_f \rangle}{\partial t} - \frac{1}{V} \int_{A_{fs}} \mathbf{n}_{fs} \cdot \mathbf{w}_{fs} dA, \quad (\text{A. 5})$$

where, \mathbf{n}_{fs} is the normal vector directed from f -phase toward the s -phase; \mathbf{w}_{fs} is the velocity of f - s interface. Quintard and Whitaker has proved that (Quintard & Whitaker, 1993)

$$\nabla \cdot \langle v_f \rangle = 0, \quad (\text{A. 6})$$

$$\text{and } \nabla \cdot (\varepsilon_f \langle v_f^f \rangle) = 0. \quad (\text{A. 7})$$

The Gray decomposition has the following equations (Gray, 1975)

$$v_f = \langle v_f \rangle^f + \tilde{v}_f, \quad (\text{A. 8})$$

$$\text{and } \langle v_f v_f \rangle^f = \langle v_f \rangle^f \langle v_f \rangle^f + \langle \tilde{v}_f \tilde{v}_f \rangle^f. \quad (\text{A. 9})$$

A2. Averaged continuity equation

We assume the densities of ρ_f and ρ_s are uniform in the control volume and the liquid density only varies on the macroscopic scale. Thus, we have

$$\rho_k = \gamma_f \langle \rho_k \rangle^k, k = f, s, \quad (\text{A. 10})$$

where, $\langle \rho_k \rangle^k$ is the intrinsic volume average density. Apply the Gray decomposition in the mass conservation equation of f -phase Eq. (2-6)

$$\frac{\partial \rho_f}{\partial t} + \nabla \cdot (\rho_f (\langle v_f \rangle^f + \tilde{v}_\beta)) = 0. \quad (\text{A. 11})$$

Multiply by ε_f and use derivative identities to expand the above equation

$$\varepsilon_f \frac{\partial \rho_f}{\partial t} + \varepsilon_f \rho_f \nabla \cdot \langle v_f \rangle^f + \varepsilon_f \langle v_f \rangle^f \cdot \nabla \rho_f + \varepsilon_f \rho_f \nabla \cdot \tilde{v}_\beta + \varepsilon_f \tilde{v}_\beta \cdot \nabla \rho_f = 0. \quad (\text{A. 12})$$

Taking the averaging theorems on the mass conservation equation, the averaged macroscopic mass conservation equation for the fluid phase can be written as

$$\frac{\partial}{\partial t} (\varepsilon_f \rho_f) + \nabla \cdot (\varepsilon_f \rho_f \langle v_f \rangle^f) = \frac{\partial}{\partial t} (\varepsilon_f \rho_f) + \nabla \cdot (\rho_f \langle v_f \rangle) = \dot{m}_f. \quad (\text{A. 13})$$

The above equation can be written as

$$\varepsilon_f \frac{\partial \rho_f}{\partial t} + \rho_f \frac{\partial \varepsilon_f}{\partial t} + \varepsilon_f \rho_f \nabla \cdot \langle v_f \rangle^f + \varepsilon_f \langle v_f \rangle^f \cdot \nabla \rho_f + \langle v_f \rangle^f \rho_f \cdot \nabla \varepsilon_f = \dot{m}_f. \quad (\text{A. 14})$$

Using Eq.(A. 12) to subtract Eq.(A. 14) leads to the local continuity equation

$$\varepsilon_f \rho_f \nabla \cdot \tilde{v}_f + \varepsilon_f \tilde{v}_f \cdot \nabla \rho_f = \rho_f \frac{\partial \varepsilon_f}{\partial t} + \langle v_f \rangle^f \rho_f \cdot \nabla \varepsilon_f + \dot{m}_f, \quad (\text{A. 15})$$

with the boundary condition of

$$\rho_f \mathbf{n}_{fs} \cdot (v_f - \mathbf{w}_{fs}) = \rho_s \mathbf{n}_{fs} \cdot (v_s - \mathbf{w}_{fs}) \text{ at } A_{fs}, \quad ((\text{A. 16}))$$

where, v_s is very small in the solid zone and can be ignored. Then the above equation can be

turned into the following format with $\delta = 1 - \frac{\rho_s}{\rho_f}$

$$\mathbf{n}_{fs} \cdot v_f = \delta (\mathbf{n}_{fs} \cdot \mathbf{w}_{fs}) \text{ at } A_{fs}. \quad (\text{A. 17})$$

Apply Gray decomposition in the above boundary condition

$$\mathbf{n}_{fs} \cdot \langle v_f \rangle^f + \mathbf{n}_{fs} \cdot \tilde{v}_f = \delta(\mathbf{n}_{fs} \cdot \mathbf{w}_{fs}) \text{ at } A_{fs}. \quad (\text{A. 18})$$

In the problem of acidizing and other surface reaction problem, the velocity of the solid-fluid interface \mathbf{w}_{fs} is much smaller than the fluid velocity $\langle v_f \rangle^f$. Therefore, the above boundary condition can be reduced to

$$\mathbf{n}_{fs} \cdot \langle v_f \rangle^f = -\mathbf{n}_{fs} \cdot \tilde{v}_f \text{ at } A_{fs}. \quad (\text{A. 19})$$

This equation provides $\langle v_f \rangle^f = -\tilde{v}_f$. Thus, from non-slip boundary condition, we can estimate that the velocity deviation of \tilde{v}_f has the order of magnitude (Quintard & Whitaker, 1994)

$$\tilde{v}_f = O(\langle v_f \rangle^f). \quad (\text{A. 20})$$

The order of magnitude estimates associated with local continuity equation is given as:

$$\begin{array}{cccccc} \varepsilon_f \rho_f \nabla \cdot \tilde{v}_f + \varepsilon_f \tilde{v}_f \cdot \nabla \rho_f = \rho_f \frac{\partial \varepsilon_f}{\partial t} + \langle v_f \rangle^f \rho_f \cdot \nabla \varepsilon_f + \dot{m}_f, & & & & & (\text{A. 21}) \\ \downarrow & & \downarrow & & \downarrow & & \downarrow & & \downarrow \\ O(\varepsilon_f \rho_f \frac{\langle v_f \rangle^f}{l_f}) & O(\varepsilon_f \langle v_f \rangle^f \frac{\rho_f}{L}) & O(\rho_f \varepsilon_f \frac{\bar{w}_n}{l_f}) & O(\rho_f \langle v_f \rangle^f \frac{\varepsilon_f}{L_\varepsilon}) & O(\varepsilon_f \rho_s \frac{\bar{w}_n}{l_f}). \end{array}$$

In our problem, \dot{m}_f is the source term, which accounts for the surface reaction and usually represents the rate of dissolution and precipitation. \dot{m}_f can be defined as $\dot{m}_f = -\frac{1}{V} \int_{A_{fs}} \rho_f \mathbf{n}_{fs} \cdot (v_f - \mathbf{w}_{fs}) dA$. According to the mass balance equation, $\dot{m}_f = -\dot{m}_s \sim \rho_s A_v \bar{w}_n$, in which A_v is the specific surface area and calculated by $A_v = A_{fs}/V$, and \bar{w}_n is the averaged interfacial growth velocity and calculated by $\bar{w}_n = \frac{1}{A} \int_{A_{fs}} \rho_f \mathbf{n}_{fs} \cdot \mathbf{w}_{fs} dA$. $\frac{\partial \varepsilon_f}{\partial t} = \frac{1}{A} \int_{A_{fs}} \rho_f \mathbf{n}_{fs} \cdot \mathbf{w}_{fs} dA$ is valid for the surface reaction problem. Thus, \dot{m}_f can be estimated to have the order of magnitude of $O(\varepsilon_f \rho_s \frac{\bar{w}_n}{l_f})$.

After applying the constrain of characteristics length of $l_s, l_f \ll r_o \ll L, l_s, l_f \ll r_o \ll L_\varepsilon$ with the natural convection condition $\bar{w}_n \ll \|\langle v_f \rangle^f\|$, we finally have

$$\nabla \cdot \tilde{v}_f = 0. \quad (\text{A. 22})$$

A3. Averaged momentum equation

Take the surficial average of the momentum equation, we have the following equation

$$\left\langle \frac{\partial}{\partial t} (\rho_f v_f) \right\rangle + \langle \nabla \cdot (\rho_f v_f v_f) \rangle = -\langle \nabla P_f \rangle + \langle \mu_f \nabla^2 v_f \rangle. \quad (\text{A. 23})$$

Apply the derivative of average theorem Equations on the above equation, the first item of the left side can be written as

$$\begin{aligned} \left\langle \frac{\partial}{\partial t} (\rho_f v_f) \right\rangle &= \frac{\partial}{\partial t} \langle \rho_f v_f \rangle - \frac{1}{V} \int_{A_{fs}} (\mathbf{n}_{fs} \cdot \mathbf{w}_{fs}) \rho_f v_f dA = \frac{\partial}{\partial t} (\rho_f \varepsilon_f \langle v_f \rangle^f) - \\ &\frac{1}{V} \int_{A_{fs}} (\mathbf{n}_{fs} \cdot \mathbf{w}_{fs}) \rho_f v_f dA. \end{aligned} \quad (\text{A. 24})$$

The second item of the left side can be written as

$$\begin{aligned} \langle \nabla \cdot (\rho_f v_f v_f) \rangle &= \nabla \cdot \langle \rho_f v_f v_f \rangle + \frac{1}{V} \int_{A_{fs}} \mathbf{n}_{fs} \cdot \mathbf{A}_f dA = \nabla \cdot \rho_f \varepsilon_f \langle v_f v_f \rangle^f + \frac{1}{V} \int_{A_{fs}} (\mathbf{n}_{fs} \cdot \\ &\mathbf{v}_f) \rho_f v_f dA. \end{aligned} \quad (\text{A. 25})$$

Apply Gray's decomposition of $\langle v_f v_f \rangle^f = \langle v_f \rangle^f \langle v_f \rangle^f + \langle \tilde{v}_f \tilde{v}_f \rangle^f$ on the above equation

$$\langle \nabla \cdot (\rho_f v_f v_f) \rangle = \nabla \cdot (\varepsilon_f \rho_f \langle v_f \rangle^f \langle v_f \rangle^f) + \nabla \cdot (\varepsilon_f \rho_f \langle \tilde{v}_f \tilde{v}_f \rangle^f) + \frac{1}{V} \int_{A_{fs}} (\mathbf{n}_{fs} \cdot \mathbf{v}_f) \rho_f v_f dA. \quad (\text{A. 26})$$

The left side of Eq. (A. 23) can become

$$\begin{aligned} \left\langle \frac{\partial}{\partial t} (\rho_f v_f) \right\rangle + \langle \nabla \cdot (\rho_f v_f v_f) \rangle &= \frac{\partial}{\partial t} (\rho_f \varepsilon_f \langle v_f \rangle^f) + \nabla \cdot (\varepsilon_f \rho_f \langle v_f \rangle^f \langle v_f \rangle^f) + \nabla \cdot \\ &(\varepsilon_f \rho_f \langle \tilde{v}_f \tilde{v}_f \rangle^f) + \frac{1}{V} \int_{A_{fs}} \mathbf{n}_{fs} \cdot (\mathbf{v}_f - \mathbf{w}_{fs}) \rho_f v_f dA. \end{aligned} \quad (\text{A. 27})$$

The first term of right side can be written as

$$-\langle \nabla P_f \rangle = -\nabla (\varepsilon_f \langle P_f \rangle^f) - \frac{1}{V} \int_{A_{fs}} P_f \mathbf{n}_{fs} dA. \quad (\text{A. 28})$$

Apply the Gray's decomposition on the last term of the above equation:

$$-\langle \nabla P_f \rangle = -\nabla(\varepsilon_f \langle P_f \rangle^f) - \frac{1}{V} \int_{A_{fs}} \langle P_f \rangle^f \mathbf{n}_{fs} dA - \frac{1}{V} \int_{A_{fs}} \tilde{P}_f \mathbf{n}_{fs} dA. \quad (\text{A. 29})$$

We need to notice that the average quantity $\langle P_f \rangle^f$ is estimated at \mathbf{r} instead of centroid \mathbf{x} . The detail is shown in Fig. 2-3. \mathbf{x} is the centroid of the averaging volume, which is the geometric center of the averaging volume. It depends on the shape of the averaging volume and doesn't change with the property. It's obtained from the mean position of all points in the body. Thus, we can use Tylor series expansion about the centroid \mathbf{x} of the averaging volume on $\langle P_f \rangle^f$

$$\langle P_f \rangle^f \Big|_{\mathbf{r}} = \langle P_f \rangle^f \Big|_{\mathbf{x}} + (\mathbf{r} - \mathbf{x}) \cdot \nabla \langle P_f \rangle^f \Big|_{\mathbf{x}} + \frac{1}{2} (\mathbf{r} - \mathbf{x})^2 : \nabla \nabla \langle P_f \rangle^f \Big|_{\mathbf{x}} + \dots \quad (\text{A. 30})$$

Let $\mathbf{y} = \mathbf{r} - \mathbf{x}$ and substitute Eq. (A. 29) into Eq.(A. 30)

$$\begin{aligned} -\langle \nabla P_f \rangle &= -\nabla(\varepsilon_f \langle P_f \rangle^f) - \frac{1}{V} \int_{A_{fs}} \mathbf{n}_{fs} dV \langle P_f \rangle^f \Big|_{\mathbf{x}} - \frac{1}{V} \int_{A_{fs}} \mathbf{y} \mathbf{n}_{fs} dV \nabla \langle P_f \rangle^f \Big|_{\mathbf{x}} - \\ &\frac{1}{2} \frac{1}{V} \int_{A_{fs}} \mathbf{y} \mathbf{y} \mathbf{n}_{fs} dV \nabla \nabla \langle P_f \rangle^f \Big|_{\mathbf{x}} - \frac{1}{V} \int_{A_{fs}} \tilde{P}_f \mathbf{n}_{fs} dV. \end{aligned} \quad (\text{A. 31})$$

From the schematic of the averaging volume, $\int_{A_{fs}} \mathbf{y} \mathbf{y} \mathbf{n}_{fs} dV$ and $\int_{A_{fs}} \mathbf{y} \mathbf{n}_{fs} dV$ is very small and can be neglected. Substitute equation $\psi_f = \gamma_f$ in Eq. (A. 3), we can obtain $\frac{1}{V} \int_{A_{fs}} \mathbf{n}_{fs} dV = -\nabla \varepsilon_f$. Thus Eq. (A. 31) can be written as

$$-\langle \nabla P_f \rangle = -\nabla(\varepsilon_f \langle P_f \rangle^f) + \langle P_f \rangle^f \nabla \varepsilon_f - \frac{1}{V} \int_{A_{fs}} \tilde{P}_f \mathbf{n}_{fs} dV. \quad (\text{A. 32})$$

The above equation can be finally turn into

$$-\langle \nabla P_f \rangle = -\varepsilon_f \nabla \langle P_f \rangle^f - \frac{1}{V} \int_{A_{fs}} \tilde{P}_f \mathbf{n}_{fs} dV. \quad (\text{A. 33})$$

Using the same method as above, we can finally obtain the viscosity term as

$$\langle \mu_f \nabla^2 v_f \rangle = \varepsilon_f \mu_f \nabla^2 \langle v_f \rangle^f + \frac{\mu_f}{V} \int_{A_{fs}} \mathbf{n}_{fs} \cdot \nabla \tilde{v}_f dA + \mu_f \nabla \cdot \left(\frac{1}{V} \int_{A_{fs}} \mathbf{n}_{fs} \tilde{v}_f dA \right). \quad (\text{A. 34})$$

The averaged momentum equation can be written as

$$\begin{aligned} & \frac{\partial}{\partial t} (\rho_f \varepsilon_f \langle v_f \rangle^f) + \nabla \cdot (\varepsilon_f \rho_f \langle v_f \rangle^f \langle v_f \rangle^f) + \nabla \cdot (\varepsilon_f \rho_f \langle \tilde{v}_f \tilde{v}_f \rangle^f) + \frac{1}{V} \int_{A_{fs}} \mathbf{n}_{fs} \cdot (\mathbf{v}_f - \\ & \mathbf{w}_{fs}) \rho_f v_f dA = -\varepsilon_f \nabla \langle P_f \rangle^f + \varepsilon_f \mu_f \nabla^2 \langle v_f \rangle^f + \frac{1}{V} \int_{A_{fs}} \mathbf{n}_{fs} \cdot (-\tilde{P}_f \mathbf{I} + \mu_f \nabla \tilde{v}_f) dA + \mu_f \nabla \cdot \\ & \left(\frac{1}{V} \int_{A_{fs}} \mathbf{n}_{fs} \tilde{v}_f dA \right) \end{aligned} \quad (\text{A. 35})$$

$$\begin{aligned} \text{and } & \langle v_f \rangle^f \frac{\partial}{\partial t} (\rho_f \varepsilon_f) + \rho_f \varepsilon_f \frac{\partial \langle v_f \rangle^f}{\partial t} + \varepsilon_f \rho_f \langle v_f \rangle^f \nabla \cdot \langle v_f \rangle^f + \langle v_f \rangle^f \nabla \cdot (\varepsilon_f \rho_f \langle v_f \rangle^f) + \nabla \cdot \\ & (\varepsilon_f \rho_f \langle \tilde{v}_f \tilde{v}_f \rangle^f) + \frac{1}{V} \int_{A_{fs}} \mathbf{n}_{fs} \cdot (\mathbf{v}_f - \mathbf{w}_{fs}) \rho_f v_f dA = -\varepsilon_f \nabla \langle P_f \rangle^f + \varepsilon_f \mu_f \nabla^2 \langle v_f \rangle^f + \frac{1}{V} \int_{A_{fs}} \mathbf{n}_{fs} \cdot \\ & (-\tilde{P}_f \mathbf{I} + \mu_f \nabla \tilde{v}_f) dA + \mu_f \nabla \cdot \left(\frac{1}{V} \int_{A_{fs}} \mathbf{n}_{fs} \tilde{v}_f dA \right). \end{aligned} \quad (\text{A. 36})$$

Substitute the continuity equation Eq. (A. 13)

$$\begin{aligned} & \rho_f \varepsilon_f \frac{\partial \langle v_f \rangle^f}{\partial t} + \varepsilon_f \rho_f \langle v_f \rangle^f \nabla \cdot \langle v_f \rangle^f + \nabla \cdot (\varepsilon_f \rho_f \langle \tilde{v}_f \tilde{v}_f \rangle^f) + \frac{1}{V} \int_{A_{fs}} \mathbf{n}_{fs} \cdot (\mathbf{v}_f - \\ & \mathbf{w}_{fs}) \rho_f v_f dA + \dot{m}_f \langle v_f \rangle^f = -\varepsilon_f \nabla \langle P_f \rangle^f + \varepsilon_f \mu_f \nabla^2 \langle v_f \rangle^f + \frac{1}{V} \int_{A_{fs}} \mathbf{n}_{fs} \cdot (-\tilde{P}_f \mathbf{I} + \mu_f \nabla \tilde{v}_f) dA + \\ & \mu_f \nabla \cdot \left(\frac{1}{V} \int_{A_{fs}} \mathbf{n}_{fs} \tilde{v}_f dA \right). \end{aligned} \quad (\text{A. 37})$$

According to the estimation of order of the magnitude

$$\begin{aligned} & \rho_f \varepsilon_f \frac{\partial \langle v_f \rangle^f}{\partial t} + \varepsilon_f \rho_f \langle v_f \rangle^f \nabla \cdot \langle v_f \rangle^f = -\varepsilon_f \nabla \langle P_f \rangle^f + \varepsilon_f \mu_f \nabla^2 \langle v_f \rangle^f + \frac{1}{V} \int_{A_{fs}} \mathbf{n}_{fs} \cdot (-\tilde{P}_f \mathbf{I} + \\ & \mu_f \nabla \tilde{v}_f) dA. \end{aligned} \quad (\text{A. 38})$$

We have the following manipulation

$$\begin{aligned} & \frac{\partial \varepsilon_f \rho_f \langle v_f \rangle^f}{\partial t} + \nabla \cdot \varepsilon_f \rho_f \langle v_f \rangle^f \langle v_f \rangle^f = \langle v_f \rangle^f \frac{\partial \varepsilon_f \rho_f}{\partial t} + \varepsilon_f \rho_f \frac{\partial \langle v_f \rangle^f}{\partial t} + \varepsilon_f \rho_f \langle v_f \rangle^f \cdot \nabla \langle v_f \rangle^f + \\ & \langle v_f \rangle^f \nabla \cdot \varepsilon_f \rho_f \langle v_f \rangle^f = \langle v_f \rangle^f \left(\frac{\partial \varepsilon_f \rho_f}{\partial t} + \nabla \cdot \varepsilon_f \rho_f \langle v_f \rangle^f \right) + \varepsilon_f \rho_f \frac{\partial \langle v_f \rangle^f}{\partial t} + \varepsilon_f \rho_f \langle v_f \rangle^f \cdot \nabla \langle v_f \rangle^f. \end{aligned} \quad (\text{A. 39})$$

Since we didn't consider the interfacial momentum transfer in this problem, the first term is zero. We have the following relationship

$$\varepsilon_f \rho_f \frac{\partial \langle v_f \rangle^f}{\partial t} + \varepsilon_f \rho_f \langle v_f \rangle^f \cdot \nabla \langle v_f \rangle^f = \frac{\partial \varepsilon_f \rho_f \langle v_f \rangle^f}{\partial t} + \nabla \cdot \varepsilon_f \rho_f \langle v_f \rangle^f \langle v_f \rangle^f. \quad (\text{A. 40})$$

Eq. (A. 38) can be written into

$$\frac{\partial \varepsilon_f \rho_f \langle v_f \rangle^f}{\partial t} + \nabla \cdot \varepsilon_f \rho_f \langle v_f \rangle^f \langle v_f \rangle^f = -\varepsilon_f \nabla \langle P_f \rangle^f + \varepsilon_f \mu_f \nabla^2 \langle v_f \rangle^f + \frac{1}{V} \int_{A_{fs}} \mathbf{n}_{fs} \cdot (-\tilde{P}_f \mathbf{I} + \mu_f \nabla \tilde{v}_f) dA. \quad (\text{A. 41})$$

A4. Closure problem

The above equation is non-closed equation. We need to find the closure problem to express \tilde{v}_f and \tilde{P}_f by their intrinsic averaged velocity $\langle v_f \rangle^f$ and pressure $\langle P_f \rangle^f$. Thus substitute the Gray's decomposition into the momentum equation Eq. (2-7) and subtract Eq.(A. 38)

$$\begin{aligned} & \rho_f \varepsilon_f \frac{\partial \tilde{v}_f}{\partial t} + \rho_f \varepsilon_f v_f \cdot \nabla \tilde{v}_f + \rho_f \varepsilon_f \tilde{v}_f \cdot \nabla \langle v_f \rangle^f - \nabla \cdot ((\varepsilon_f \rho_f \langle \tilde{v}_f \tilde{v}_f \rangle^f) - \frac{1}{V} \int_{A_{fs}} \mathbf{n}_{fs} \cdot (\mathbf{v}_f - \\ & \mathbf{w}_{fs}) \rho_f \mathbf{v}_f dA = -\varepsilon_f \nabla \tilde{P}_f + \varepsilon_f \mu_f \nabla^2 \tilde{v}_f - \frac{1}{V} \int_{A_{fs}} \mathbf{n}_{fs} \cdot (-\tilde{P}_f \mathbf{I} + \mu_f \nabla \tilde{v}_f) dA - \mu_f \nabla \cdot \\ & \left(\frac{1}{V} \int_{A_{fs}} \mathbf{n}_{fs} \tilde{v}_f dA \right). \end{aligned} \quad (\text{A. 42})$$

Repeat the procedure of the previous estimating the order of magnitude of each term, the first four terms of left side have the following order of magnitude

$$\begin{array}{cccc} \rho_f \varepsilon_f \frac{\partial \tilde{v}_f}{\partial t} + \rho_f \varepsilon_f v_f \cdot \nabla \tilde{v}_f + \rho_f \varepsilon_f \tilde{v}_f \cdot \nabla \langle v_f \rangle^f - \nabla \cdot ((\varepsilon_f \rho_f \langle \tilde{v}_f \tilde{v}_f \rangle^f), & & & \\ \downarrow & \downarrow & \downarrow & \downarrow \\ O(\varepsilon_f \rho_f \frac{\tilde{v}_f}{\tilde{t}}) & O(\varepsilon_f \rho_f \frac{(\langle v_f \rangle^f)^2}{l_f}) & O(\varepsilon_f \rho_f \langle v_f \rangle^f \frac{(\langle v_f \rangle^f)^2}{L}) & O(\varepsilon_f \rho_f \frac{(\langle v_f \rangle^f)^2}{L}), \end{array} \quad (\text{A. 43})$$

where, \tilde{t} is the characteristic time of \tilde{v}_f , which is far smaller than the characteristic time of $\langle v_f \rangle^f$. The first term can be neglected. Considering the characteristic length constraint of $l_f \ll r_o \ll L$, the other term has

$$\nabla \cdot ((\varepsilon_f \rho_f \langle \tilde{v}_f \tilde{v}_f \rangle^f) \sim \rho_f \varepsilon_f \tilde{v}_f \cdot \nabla \langle v_f \rangle^f \ll \rho_f \varepsilon_f v_f \cdot \nabla \tilde{v}_f. \quad (\text{A. 44})$$

Since we have non-slip boundary condition ($\mathbf{v}_f = 0$) at the solid-fluid interface, the fourth term on the left side can be ignored.

For the right side according to previous study (Bousquet-Melou et al., 2002):

$$\begin{aligned} \varepsilon_f \mu_f \nabla^2 \tilde{v}_f - \frac{1}{V} \int_{A_{fS}} \mathbf{n}_{fS} \cdot (-\tilde{P}_f \mathbf{I} + \mu_f \nabla \tilde{v}_f) dA - \mu_f \nabla \cdot \left(\frac{1}{V} \int_{A_{fS}} \mathbf{n}_{fS} \tilde{v}_f dA \right), \quad (\text{A. 45}) \\ \downarrow \qquad \qquad \qquad \downarrow \qquad \qquad \qquad \downarrow \\ \mathcal{O}(\varepsilon_f \mu_f \frac{\langle v_f \rangle^f}{l_f^2}) \quad \mathcal{O}(\varepsilon_f \mu_f \frac{\langle v_f \rangle^f}{l_f^2}) \quad \mathcal{O}(\varepsilon_f \mu_f \frac{\langle v_f \rangle^f}{L_\varepsilon^2}). \end{aligned}$$

We have the constraint of $l_f \ll r_o \ll L_\varepsilon$, thus, $\varepsilon_f \mu_f \nabla^2 \tilde{v}_f \sim \frac{1}{V} \int_{A_{fS}} \mathbf{n}_{fS} \cdot (-\tilde{P}_f \mathbf{I} + \mu_f \nabla \tilde{v}_f) dA \gg \mu_f \nabla \cdot \left(\frac{1}{V} \int_{A_{fS}} \mathbf{n}_{fS} \tilde{v}_f dA \right)$. Finally, the local closure momentum equation with the closed continuity equation can be written as

$$\rho_f \mathbf{v}_f \cdot \nabla \tilde{v}_f = -\nabla \tilde{P}_f + \mu_f \nabla^2 \tilde{v}_f - \frac{1}{V} \int_{A_{fS}} \mathbf{n}_{fS} \cdot (-\tilde{P}_f \mathbf{I} + \mu_f \nabla \tilde{v}_f) dA, \quad (\text{A. 46})$$

$$\text{and } \nabla \cdot \tilde{v}_f = 0. \quad (\text{A. 47})$$

A5. Discretization theory

Applying the Gauss's theorem, we can obtain these identities

$$\int_V \nabla \cdot \mathbf{a} dV = \int_A \mathbf{a} \cdot \vec{\mathbf{n}} dA, \quad (\text{A. 48})$$

$$\int_V \nabla \varphi dV = \int_A \varphi \vec{\mathbf{n}} dA \quad (\text{A. 49})$$

$$\text{and } \nabla \varphi = \frac{1}{V} \sum_F \varphi_f \vec{\mathbf{n}} A_f. \quad (\text{A. 50})$$

where, \mathbf{a} is the vector and φ is the scalar property. V is the volume of the control volume; A is the surface bounding the volume V . In FVM, the variables were regarded as the linear distribution along through the cell, thus, we can have

$$\varphi(\mathbf{x}) = \varphi_P + (\mathbf{x} - \mathbf{x}_P) \cdot (\nabla \varphi)_P. \quad (\text{A. 51})$$

P denotes the centroid of the owner cell. \mathbf{x}_p and \mathbf{x} represents the location vector. The definition centroid position has

$$\int_V \mathbf{x} dV = V_P \mathbf{x}_p, \quad (\text{A. 52})$$

move the term in the left side to the right side and get

$$0 = \int_V \mathbf{x} dV - \mathbf{x}_p \int_V dV. \quad (\text{A. 53})$$

Then, we can have

$$0 = \int_V (\mathbf{x} - \mathbf{x}_p) dV. \quad (\text{A. 54})$$

Taking the integral form of the above equation over the control volume P

$$\int_{VP} \varphi(\mathbf{x}) dV = \int_{VP} [\varphi_P + (\mathbf{x} - \mathbf{x}_p) \cdot (\nabla\varphi)_P] dV = \varphi_P \int (\mathbf{x} - \mathbf{x}_p) dV \cdot (\nabla\varphi)_P = \varphi_P V_P. \quad (\text{A. 55})$$

We can use the following equation to represents the interpolation scheme when calculate the value φ on the cell face

$$\varphi_f = f_x \varphi_P + (1 - f_x) \varphi_N. \quad (\text{A. 56})$$

For the Central Difference (linear) scheme

$$f_x = \frac{\overline{fN}}{\overline{PN}}, \quad (\text{A. 57})$$

where, \overline{fN} is the distance from cell surface to the center of neighbor cell; \overline{PN} is the distance from the center of owner cell to the neighbor cell. The Central Difference scheme has second-order accuracy. It is often used to interpolate the center value to the face value on the diffusion term instead of the convention.

For the Upwind Differencing scheme, the face value is determined according to the flow direction

$$f_x = \begin{cases} 1 & \text{for } F > 0, \\ 0 & \text{for } F < 0, \end{cases} \quad (\text{A. 58})$$

where, F is the mass flux through the cell face. This scheme is often particular used on the convection term because we want to take more information about the flow when determine the interpolation scheme, and it is very stable. However, the upwind Differencing scheme only has the first-order accuracy. There are some other advanced interpolation schemes like Linear Upwind Differencing scheme and Blended Differencing scheme. The Upwind Differencing scheme has

$$\varphi_f = \begin{cases} \varphi_P + \Phi(\nabla\varphi)_P \cdot \mathbf{r} & \text{for } F > 0, \\ \varphi_P + \Phi(\nabla\varphi)_N \cdot \mathbf{r} & \text{for } F < 0, \end{cases} \quad (\text{A. 59})$$

where, \mathbf{r} is the vector between the centroid P and the cell face. Φ is the gradient limiter, which is in the range of 0 to 1 and it is used to guarantee the stability when the $\nabla\varphi$ is too steep. The Blended Differencing scheme has the following equation

$$\varphi_f = \Psi\varphi_{UD} + (1 - \Psi)\varphi_{CD}. \quad (\text{A. 60})$$

Blended Differencing scheme considered the Central Differencing φ_{UD} for accuracy and Upwind Differencing φ_{CD} for the stability. Ψ is the blending function.

A6. Validation of the solid deformation

To validate the deformation of plastic solid (clay), we compared the numerical results with the analytical solution of the fluid-driven deformation of a clay filter cake. The analytical model is based on Biot theory and is able to predict the 1-D solid deformation of the plug as a function of its initial porosity, the deformation modulus of the solid, and the fluid pressure gradient across the plug (Hewitt et al. 2016). The published analytical models gave a good agreement with the experimental measurements from several experiments under different

pressure heads. In the analytical model, the clay was regarded as porous media and was initially unstrained. The clay was initially saturated with fluid, and the height of water (H) was above the clay cake. In our numerical simulation, we simulated a 1-D container with a size of 12 cm \times 15 cm, which was partially filled with clay. The initial clay depth was set as 9 cm. The schematic of the geometric model was shown in Fig. A-1 (a). We simulated two different porosity of 0.5 and 0.6. We considered 0.5 and 0.6 here, because the typical porosity of clay is found to be 0.5 to 0.6 (S. Chen et al., 2016; Kim, Hwang, & Jang, 2016; Vallejo & Mawby, 2000). Since we described the clay with double structures, which contain macropores and micropores, the porosity here represents the void space fraction of the clay cake. To describe the clay swelling, the porosity of clay cake increases as the pore space of interlayer, inter-grain, and interparticle of bentonite increased. The change of the volume of clay was shown in Fig. A-1 (c). The numerical results meet well with the analytical results. The change of volume was obtained until the clay deformation reached the steady state. Fig. A-1 (b) shows the clay cake after reaching the equilibrium states, where the clay cake had different deformations under different dimensionless pressures. Here, the dimensionless pressure is calculated by the ratio of the applied fluid pressure difference to the elastic modulus of the clay, as shown in the following equation:

$$P_d = \frac{\rho g H}{\sigma^*}, \quad (\text{A. 61})$$

where, ρ is the fluid density; H is the total height of container; σ^* is the elastic modulus of the clay, which was taken as 1,900 Pa in our simulation. As the dimensionless pressure increased, the clay deformation became slight.

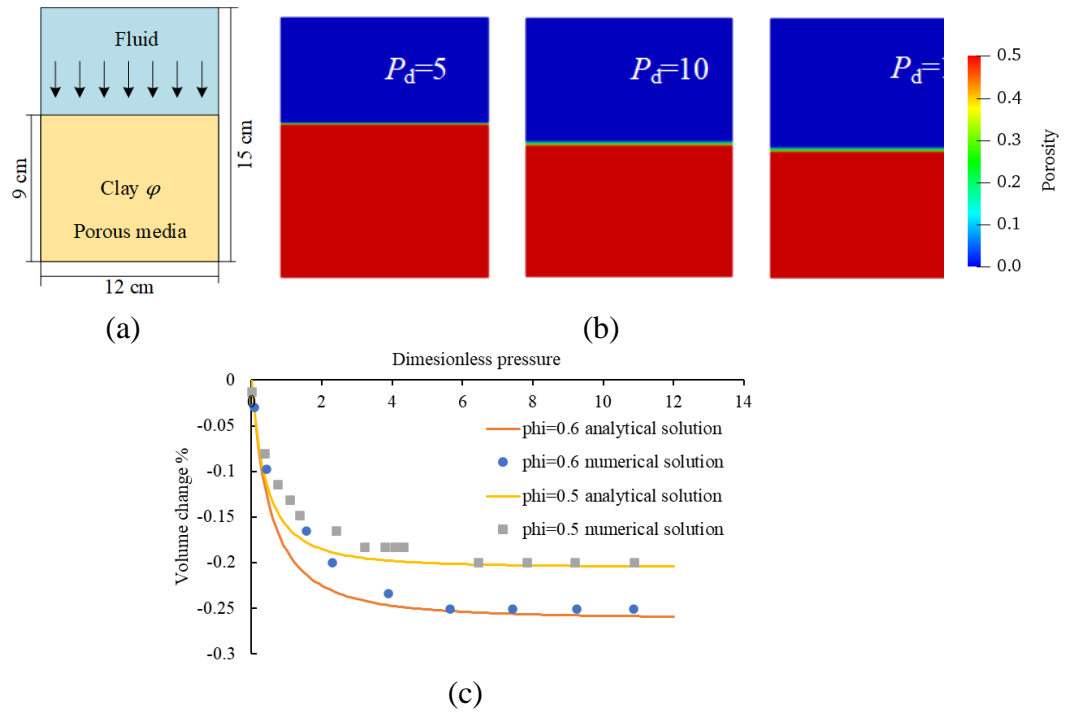


Fig. A-1 (a) Schematic of the geometric model; (b) Clay porosity when fluid-driven deformation reaches the steady state under different dimensionless pressures with initial porosity of 0.5; (c) the comparison of volume change between numerical results and analytical results.